In-medium properties of the ω-meson studied in photonuclear reactions near the production threshold

Inaugural-Dissertation zur Erlangung
des Doktorgrades der Naturwissenschaften
der Justus-Liebig-Universität Gießen
Fachbereich 07
(Mathematik und Informatik, Physik, Geographie)

vorgelegt von

Michaela Thiel
aus Butzbach

II. Physikalisches Institut der
Justus-Liebig-Universität Gießen

10. November 2010

Abstract

Hadrons can be described with their fundamental properties like their mass or lifetime. Nowadays, these values seem to be well known in vacuum. But what happens, if hadrons are embedded in a strongly interacting environment? To answer this question, theoretical physicists are working on model calculations which (up to now) can not give a consistent conclusion: the results vary from predictions assuming a lowering of the vector meson mass in a strongly interacting environment up to predictions assuming a higher mass at high densities. Other models predict structures in the hadron spectral function due to a coupling of the hadron to nucleon resonances. Hence, experiments are needed to check the theoretical predictions.

Light vector mesons seem to be the ideal probe to study in-medium modifications. Their lifetimes are short enough, so that their decay length is comparable to nuclear dimensions. Therefore the probability is high, that the vector mesons decay inside the nuclear medium. The measured decay products than carry the in-medium informations of the vector meson. In this thesis, possible modifications of the ω meson were studied in photonuclear reactions. Most of the former experiments on this topic studied the leptonic decay into e^+e^-. This is a clean and ideal method to study in-medium modifications since leptons do not underly the strong force. Nevertheless, for this thesis the hadronic decay $\omega \to \pi^0\gamma$ was chosen. This decay mode allows to measure the undistorted ω invariant mass spectrum since contributions from the ρ meson are suppressed by two orders of magnitude. Having the pion as a strongly interacting particle in the final state is a disadvantage of this decay channel: due to final state interactions the reconstructed four-momenta can be distorted. Applying a cut on the kinetic energy of the pion $T_{\pi^0} > 150$ MeV reduces the amount of distorted events.

The experiments for this thesis were performed at the Mainzer Mikrotron MAMI during three beamtimes in 2008. After an upgrade in the year 2006, a continuous electron beam with energies up to 1600 MeV is available. Real photons are produced due to the Bremsstrahlung process when the electron beam impinges on a radiator. The energy of the photons is determined using the Mainz-Glasgow tagging system. For this thesis the reaction

$$\gamma A \to (A-1)\omega p \to (A-1)\pi^0\gamma p \to (A-1)\gamma\gamma\gamma p \qquad (0.1)$$

was investigated for the two different target materials carbon and niobium. To detect the decay products, the detector systems Crystal Ball and TAPS were used. Together they cover roughly the full solid angle of 4π.

Within this thesis, the lineshape of the $\pi^0\gamma$ invariant mass was studied for different nuclear targets. As a reference the signal is compared to a signal obtained from a liquid hydrogen target. The ω meson was reconstructed using two different analysis branches. In an exclusive analysis three photons and one proton were requested, in a semi-exclusive analysis only three photons were requested. A sideband subtraction technique was used to remove chance coincidences and background contributions from $\pi^0\eta$ decays from the invariant mass spectrum.

The exact determination of the background was necessary, since it has a direct impact on the lineshape of the ω signal. Therefore the background contribution was identified using two different method. In the first method the background was determined by a fit, while in the second the background was directly obtained from the data, selecting four photon events and omitting one of them randomly.

Both methods were compared and the result showed the systematic uncertainties in the determination of the ω lineshape. A comparison of the invariant mass distributions for the three different target materials (liquid hydrogen, carbon, niobium) showed good agreement for C and Nb and a slight broadening compared to the ω signal from the hydrogen target after correcting for the 5 cm target length.

In addition niobium data was compared to GiBUU calculations. A deviation from the scenario assuming a mass shift of 16% was observed. Therefore, this scenario could be excluded. This was supported by the results obtained from the analysis of the ω meson momentum distributions, which was also part of this thesis. Here, a deviation of the experimental data from the theoretical scenarios including a mass shift could clearly be seen. The scenarios without mass shift were in good agreement with the experimental data.

Zusammenfassung

Hadronen können durch ihre fundamentalen Eigenschaften wie ihre Masse oder Lebensdauer beschrieben werden. In der heutigen Zeit gehen wir davon aus, diese Größen für den Vakuumszustand zu kennen. Aber was passiert wenn Hadronen in einem stark wechselwirkenden Medium agieren, insbesondere, wenn die Dichte oder die Temperatur dieses Mediums sehr hoch ist? Eine Vielzahl von theoretischen Physikern beschäftigen sich mit dieser Fragestellung. Die bisher erzielten Vorhersagen lassen leider noch keinen einheitlichen Tenor erkennen. Die Ergebnisse reichen von einer Absenkung der Vektormeson Masse in einem stark wechselwirkenden Medium bis hin zu einer Erhöhung der Masse bei steigender Dichte. Da von den theoretischen Vorhersagen kein Szenario wirklich ausgeschlossen werden kann, braucht man Experimente zur Überprüfung der Modellrechnungen.

Leichte Vektormesonen scheinen ideale Sonden zur Untersuchung von in-Medium Modifikationen zu sein, da ihre Lebensdauer kurz genug ist, um innerhalb des nuklearen Mediums zu zerfallen. Dadurch tragen die Zerfallsprodukte die in-Medium Informationen des Vektormesons. In dieser Arbeit wurden mögliche Modifikationen des ω Mesons in photonuklearen Reaktionen untersucht. Obwohl viele frühere Experimente den Zerfall in e^+e^- und somit Leptonen in Ausgangskanal untersuchten, die nicht durch die starke Wechselwirkung beeinflusst werden, wurde für diese Arbeit der hadronische Zerfallskanal $\omega \to \pi^0\gamma$ ausgewählt. Dieser Kanal hat den Vorteil, dass Beiträge des ρ Mesons aufgrund des Verzweigungsverhältnis um zwei Größenordnungen unterdrückt sind. Ein Nachteil ist, dass das Pion ein stark wechselwirkendes Teilchen ist und durch Streuungen im Kern zu einer Verfälschung des Meßergebnises führen kann. Studien zeigten jedoch, dass dieser Anteil signifikant unterdrückt werden kann, wenn zudem ein Schnitt auf die kinetische Energie des Pions $T_{\pi^0} > 150$ MeV verlangt wird.

Die für diese Arbeit zugrunde liegenden Experimente wurden am Mainzer Mikrotron MAMI in drei Strahlzeiten im Jahr 2008 durchgeführt. Der dort zum Einsatz kommende Elektronenbeschleuniger erzeugt nach einem Upgrade im Jahre 2006 einen kontinuierlichen Elektronenstrahl mit Energien bis 1600 MeV. In einem Radiator werden unter Ausnutzung des Bremsstrahlungs-Prozesses reelle Photonen erzeugt, denen mit Hilfe des Mainz-Glasgow Tagging Systems jeweils eine eindeutige Energie zugeordnet

werden kann. Untersucht wurde im Rahmen dieser Arbeit die Reaktion

$$\gamma A \rightarrow (A-1)\omega p \rightarrow (A-1)\pi^0 \gamma p \rightarrow (A-1)\gamma\gamma\gamma p \tag{0.2}$$

sowie die semi-exklusive ω Produktion für die beiden Targetmaterialien Kohlenstoff und Niob. Die Zerfallsprodukte können mit den Detektoren Crystal Ball und TAPS nachgewiesen werden, die nahezu den kompletten Raumwinkel abdecken. Ziel der Experimente war es, die Statistik im Vergleich zu entsprechenden früheren Messungen am ELSA-Beschleuniger in Bonn deutlich zu verbessern.

Im Rahmen dieser Arbeit wurde die Linienform der $\pi^0 \gamma$ invarianten Masse bestimmt und für die Targetmaterialien Kohlenstoff und Niob verglichen. Als Referenzsignal wurde flüssiger Wasserstoff verwendet. Die Fragestellung ist, ob sich die Linienform aufgrund von in-Medium Modifikationen des ω Mesons ändert.
Für die Rekonstruktion der ω Mesonen wurden zwei unterschiedliche Analysen verwendet. In einer exklusiven Analyse wurden explizit drei Photonen und ein Proton verlangt, während in einer semi-exklusiven Analyse nur drei Photonen verlangt wurden. Seitenband-Abzugsmethoden ermöglichten den Abzug von zufällige Koinzidenzen und Untergrundbeiträgen aus $\pi^0 \eta$ Zerfällen im invarianten Massenspektrum.
Die eigentliche Schwierigkeit der Analyse bestand in der Bestimmung des Untergrundbeitrages, dessen Form direkte Auswirkung auf die Linienform des $\pi^0 \gamma$ invarianten Massenspektrums hat. Daher wurde der Untergrund für die Niob Daten zum einen mit einem Fit bestimmt und zum anderen direkt aus den Daten. Hierfür wurden Ereignisse mit vier Photonen selektiert und ein Photon davon zufällig verworfen.
Beide Methoden wurden miteinander verglichen und zeigen die systematische Unsicherheit in der Bestimmung der ω Meson Linienform. Ein Vergleich der verschiedenen Targetmaterialien zeigt eine gute Übereinstimmung für die ω Signale am C und Nb und eine geringfügige Verbreiterung gegenüber dem ω Signal am LH_2 nach Korrektur der Auflösungsverschlechterung durch die 5 cm Targetlänge.
Vergleiche zu GiBUU Rechnungen ergeben eine größere Abweichung der Daten zu dem gerechneten Szenario wo eine Massenverschiebung von 16% angenommen wurde, welches deshalb ausgeschlossen werden kann. Unterstützt wird diese Aussage von einer Analyse der Impulsverteilung, die im Rahmen dieser Arbeit ebenfalls durchgeführt wurde. Eine Abweichung zu Rechnungen, in denen lediglich eine Massenverschiebung angenommen wurde, ist deutlich zu erkennen. Die theoretischen Szenarien, in denen keine Massenverschiebung involviert ist, sind verträglich mit den experimentellen Daten.

Units and Conventions

In this thesis the electron volt (eV) is used as energy unit. One eV is the kinetic energy an electron gains when passing through a potential of 1 Volt. It is equivalent to $1.602 \cdot 10^{-19}$ J.

The constants c and $\hbar$ are set to 1 using the natural unit system. According to the equations

$$E = m \cdot c^2 \tag{0.3}$$

and

$$E = p \cdot c \tag{0.4}$$

the dimension of mass and momenta are also given in eV.

For the angles describing the experimental setup the following convention is used (illustrated in figure 0.1):

- **Polar angle**: $0° \leq \theta \leq 180°$

- **Azimuthal angle**: $-180° \leq \phi \leq +180°$
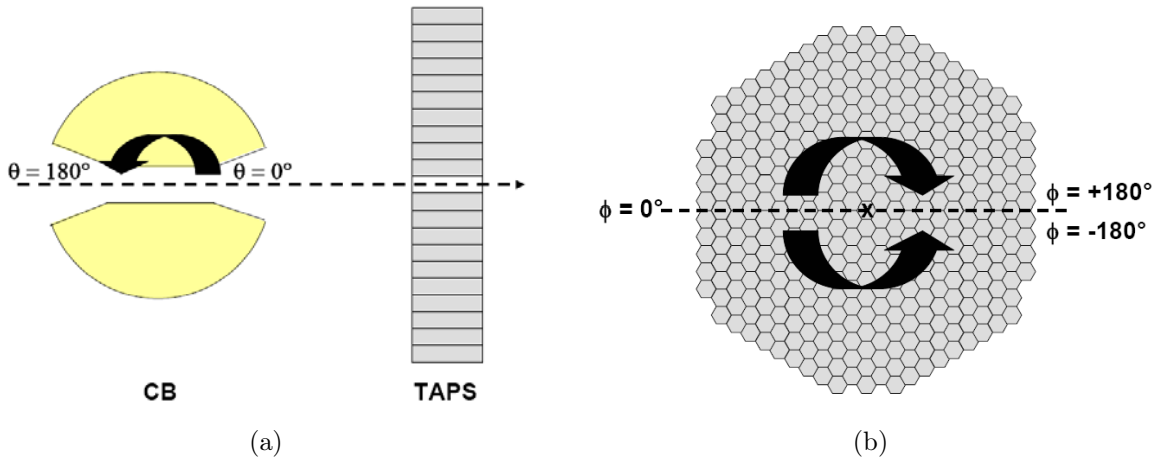
Figure 0.1: (a) Polar angle $0° \leq \theta \leq 180°$. (b) Azimuthal angle $-180° \leq \phi \leq +180°$. View in beam direction.

Contents

Contents

2

Chapter 1.

Theoretical Fundamentals

The topic of this thesis leads to the question whether the special properties of hadrons in a strongly interacting environment are modified and whether these changes are measurable. In the following a short introduction to theoretical hadron physics fundamentals is given, while the next chapter focuses on in-medium characteristics.

1.1. The Standard Model

Although nowadays a lot of particles are known, there is only a small number of elementary particles which build up all matter we know so far. The standard model describes these fundamental particles together with their interactions. 61 particles belong in total to the standard model, assuming the existence of the Higgs boson:

- 6 leptons and anti-leptons

- 6 quarks (in three different colours) and anti-quarks

- 12 exchange bosons (8 gluons, the photon, the W^+, the W^-, the Z^0)

- the Higgs boson

The particles are grouped into three families, as shown in figure 1.1. The constituents of ordinary matter belong to the first family (electron, electron-neutrino, up quark and down quark). The particles of the second and third family are heavier and unstable, they decay into the particles of the first family.
Looking at their properties, the fundamental particles can be grouped into:
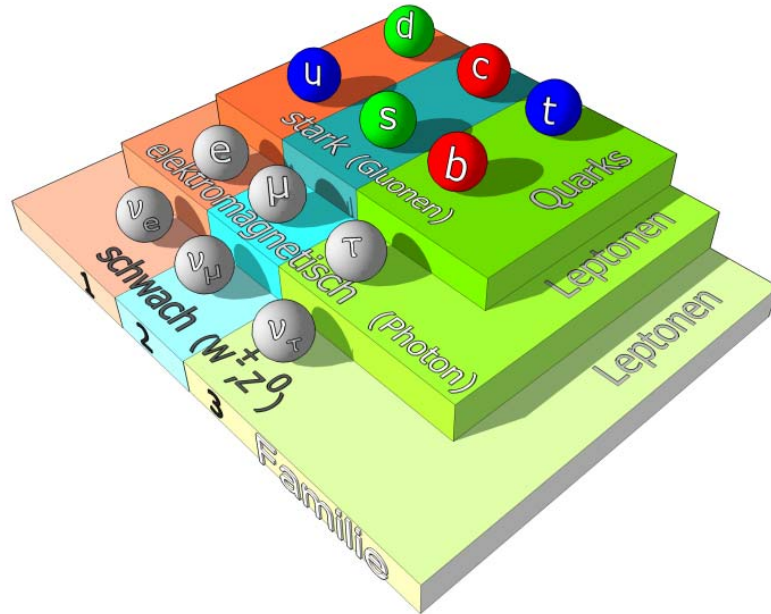
- leptons

- quarks

- gauge bosons

Figure 1.1: Elementary particles in the standard model.

1.1.1. Leptons

The name lepton comes from the greek word *leptòs* which has the meaning of „fine" or „light". As we know so far leptons are elementary particles which belong with their half-integral spin to the group of fermions. Hence, they obey the Fermi-Dirac-statistics.

Leptons can have either an electric charge of -1 or 0, an overview is listed in table 1.1.

Family	Particle	Mass	$Q/|e|$
1	e^-	511 keV	-1
1	ν_e	$<$ 2 eV	0
2	μ^-	105.66 MeV	-1
2	ν_μ	$<$ 0.19 eV	0
3	τ	1776.84 MeV	-1
3	ν_τ	$<$ 18.2 MeV	0

Table 1.1: Lepton properties. Data were taken from [PDG08].

Leptons do not carry a colour charge, hence they do not interact strongly. All leptons

carry a weak charge which allows them to interact via the weak force like e.g. in the β^- - decay. Only the electrically charged leptons can interact electromagnetically. That makes the detection of the neutral leptons difficult. Interacting just via the weak force the neutrinos can only be detected indirectly by energy and momentum balances. Today it seems to be established that neutrinos are not massless, but only upper limits can be given. This fact is supported by the observation, that neutrinos can oscillate into other flavour eigenstates.

1.1.2. Quarks

Quarks are the elementary particles building the hadrons. Like the leptons quarks are fermions with half-integral spin. 1964 their existence was first postulated by Murray Gell-Mann and George Zweig.

There are supposed to be six different quark types, the so-called flavours, all observed in accelerator experiments. The last experimentally detected quark was the top quark at Fermilab in 1995 [Abe95]. Due to their masses they can be grouped into light quarks (up, down and strange) and heavy quarks (charm, top and bottom). Table 1.2 shows an overview of the quarks with their quantum numbers and their properties.

Family	Particle	Mass [MeV]	Q/$|e|$	I_3	S	C	B	T
1	up (u)	1.5 to 3.3	+2/3	+1/2	0	0	0	0
1	down (d)	3.5 to 6.0	-1/3	-1/2	0	0	0	0
2	charm (c)	1270	+2/3	0	0	+1	0	0
2	strange (s)	104	-1/3	0	-1	0	0	0
3	top (t)	171200	+2/3	0	0	0	0	+1
3	bottom (b)	4200	-1/3	0	0	0	-1	0

Table 1.2: Quark properties. Data were taken from [PDG08].

The masses listed in table 1.2 are the current quark masses, refering to the bare masses in contrast to the constituent quark masses. These effective quark masses also take the mass of the gluon particle field surrounding the quark into account.

In addition to their flavour, quarks have a colour[1] charge (red r, green g and blue b), anti-quarks the corresponding anti-colours (anti-red $\bar{r}$, anti-green $\bar{g}$ and anti-blue $\bar{b}$). Due to their colour charge, quarks interact strongly. The resulting attraction leads to the formation of hadrons. Adding up all three colours (baryons) or the colour with the corresponding anti-colour (mesons) the composed object is colour neutral. The theory of the strong interaction claims that only colour neutral particles can exist freely and

---

[1]It is not a real colour, just an extra degree of freedom.

so far single free quarks were not observed. This effect is called confinement.

The observed states in nature always have integral electric charges. Accordingly, quarks carry -1/3 or +2/3 times the elementary charge. Scattering experiments face the fractional charges of quarks in hadrons.

Unlike the leptons, quarks underlie all four fundamental forces. Due to the weak interaction, a quark of one flavour can change into a quark of another flavour. Despite of the fact that the flavour transformation process is the same for all quarks, each quark has a preference to transform within its own family. Mathematically this can be described using the *Cabibbo-Kobayashi-Maskawa* matrix (CKM matrix):

$$\begin{pmatrix} |d'\rangle \\ |s'\rangle \\ |b'\rangle \end{pmatrix} = \begin{pmatrix} V_{ud} & V_{us} & V_{ub} \\ V_{cd} & V_{cs} & V_{cb} \\ V_{td} & V_{ts} & V_{tb} \end{pmatrix} \cdot \begin{pmatrix} |d\rangle \\ |s\rangle \\ |b\rangle \end{pmatrix} \tag{1.1}$$

The transition probability of a quark with flavour i changing to flavour j is proportional to $\left| V_{q_i q_j} \right|^2$. The strength of the weak interaction between the six quarks is illustrated in figure 1.2.
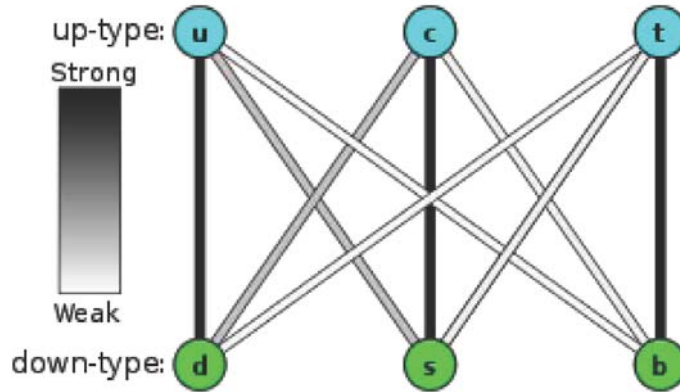

Figure 1.2: The strength of the weak interaction between the six quark flavours, determined by the matrix elements of the CKM matrix.

1.1.3. Gauge Bosons

Gauge bosons are integral spin particles, acting as the carriers of the fundamental forces. In table 1.3 they are listed together with the corresponding forces and properties.

Gauge Boson	Couples to	Interaction	J^P	Mass [GeV/c^2]
8 gluons	colour charge	strong	1^-	0
photons	el. charge	EM	1^-	0
W$^\pm$, Z^0 boson	weak charge	weak	1^-, 1^+	80 - 90
graviton	mass	gravitation	2^+	0

Table 1.3: Main properties of the gauge bosons. J denotes the total angular momentum, P the parity of the bosons.

Gluons

The gauge bosons of the strong force are the gluons. They are neutral particles and expected to be massless. Gluons couple to the colour charge of the quarks. Since the quarks change their colour due to a gluon-exchange, the gluons carry a colour and an anti-colour. Thus, $3^2 = 9$ different combinations are expected. But one of these combinations is a colour singlet state which carries no net colour charge and has to be excluded. So there are 8 gluons which can be written as an octett of states:

$$|r\bar{g}\rangle,\ |r\bar{b}\rangle,\ |g\bar{r}\rangle,\ |g\bar{b}\rangle,\ |b\bar{r}\rangle,\ |b\bar{g}\rangle,\ \frac{1}{\sqrt{2}}\left(|r\bar{r}\rangle - |g\bar{g}\rangle\right),\ \frac{1}{\sqrt{6}}\left(|r\bar{r}\rangle - |g\bar{g}\rangle - |b\bar{b}\rangle\right) \quad (1.2)$$

Due to their colour charge the gluons can also interact strongly with each other and form exotic states, e.g. glueballs or hybrids.

Photon

Photons are the exchange bosons of the electromagnetic force. They couple to the electric charge although being uncharged themselves. Photons are massless which leads to the infinite range of the electromagnetic force.

W$^\pm$ and Z^0 Boson

The gauge bosons of the weak interaction are two charged bosons, the W$^+$ and W$^-$, and the neutral Z^0 boson. Unlike the other exchange bosons, they are very massive particles which leads to the short range of the weak force. They are weakly charged and can interact with each other or couple to other weakly charged particles. A W$^\pm$ exchange modifies the electric charge and the weak isospin.

Graviton

The graviton is predicted to be the force carrying particle of gravitation but it is has not been observed yet. The graviton should be a massless spin-2 particle which has no electric charge.
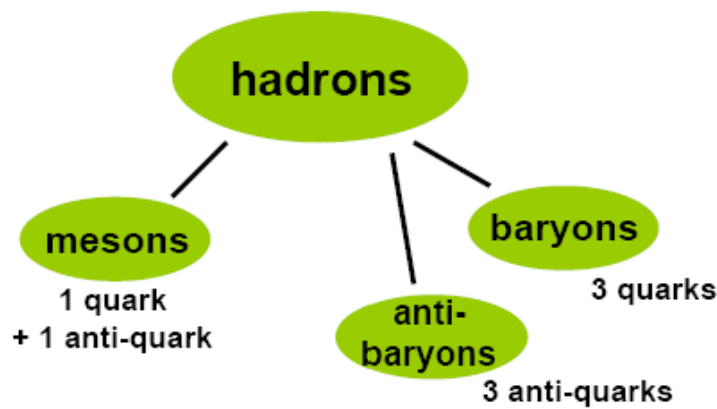
1.2. Hadrons

Figure 1.3: Classification of hadrons into baryons (qqq), anti-baryons ($\bar{q}\bar{q}\bar{q}$) and mesons ($q\bar{q}$).

The matter of our world is composed of quarks. They are building the so-called hadrons with the proton and the neutron as the most common ones. The proton is the only long living hadron, all other particles decay relatively fast into other hadrons, leptons or photons. To build hadrons from the quarks some main conditions have to be fulfilled:

- The charge of the composed object has to be an integer multiple of the elementary charge.

- The composed object has to be colour neutral.

As it is sketched in figure 1.3 hadrons can be fermions with half-integral spin, the so-called baryons, consisting of 3 quarks or bosons with integral spin, so-called mesons, composed of a quark and an anti-quark.
There may be other states with quantum numbers forbidden for the fermions and

bosons, but allowed for some exotic states like for example glueballs (e.g. ggg) or hybrids (e.g. $q\bar{q}gg$). For these states among other things the $\overline{P}$ANDA[2] detector [Col09b] will look.

1.2.1. Mesons

Mesons are composite systems containing a quark and an anti-quark. All existing mesons underlie the strong interaction, therefore they are instable particles. Due to the six quark flavours, one would expect 36 different mesons. But in addition the spin of the quarks has to be taken into account, which leads to more possible meson combinations.

Quarks are half-integral spin particles. The spin of a $q\bar{q}$ pair can couple to $S_{q\bar{q}} = |S_q + S_{\bar{q}}|$ and $S_{q\bar{q}} = |S_q - S_{\bar{q}}|$. Hence, a meson can have the total spin S of either 0 or 1.

(a) Pseudoscalar mesons   (b) Vector mesons
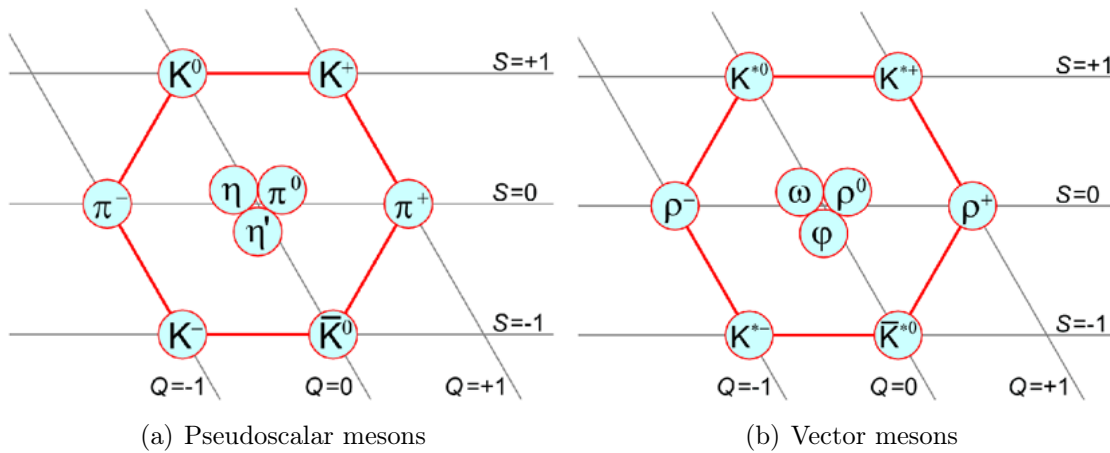
Figure 1.4: Nonets of mesons with spin 0 (a) and spin 1 (b) classified by the third component of the isospin and strangeness content. In the figures, S refers to the strangeness.

Concentrating on the three lightest quarks, the mesons can be grouped in a first step in nonets with same parity and total angular momentum J^P, but different spin. Figure 1.4(a) shows the mesons with spin 0 (pseudoscalar mesons), in figure 1.4(b) the mesons with spin 1 (vector mesons) are shown.

Due to the similar masses of the up, down and strange quarks, the quark/anti-quark states will mix. Table 1.4 shows the quark content together with the fundamental properties for the π^0 and the ω meson, the particles of main interest for this thesis.

---

[2]Anti**P**roton **AN**nihilations at **DA**rmstadt

Meson	J^{PC}	Quark Content	Mass [MeV]
π^0	0^{-+}	$\frac{1}{\sqrt{2}}\left(\left|u^{\uparrow}\bar{u}^{\downarrow}\right\rangle + \left|d^{\uparrow}\bar{d}^{\downarrow}\right\rangle\right)$	134.9766
ω	1^{--}	$\frac{1}{\sqrt{2}}\left(\left|u^{\uparrow}\bar{u}^{\uparrow}\right\rangle + \left|d^{\uparrow}\bar{d}^{\uparrow}\right\rangle\right)$	782.65

Table 1.4: Fundamental properties of the π^0 and the ω meson. J denotes the total angular momentum, P the parity and C the charge conjugation of the particles.

1.2.2. Baryons

Baryons are composed of three quarks, accordingly the anti-baryons of three anti-quarks. The three quarks can couple to a total spin of $1/2$ or $3/2$. The three lightest quarks form an octet of states with spin $1/2$ and a decuplet of states with spin $3/2$ shown in figure 1.5.

(a) Baryons with spin $1/2$.   (b) Baryons with spin $3/2$.
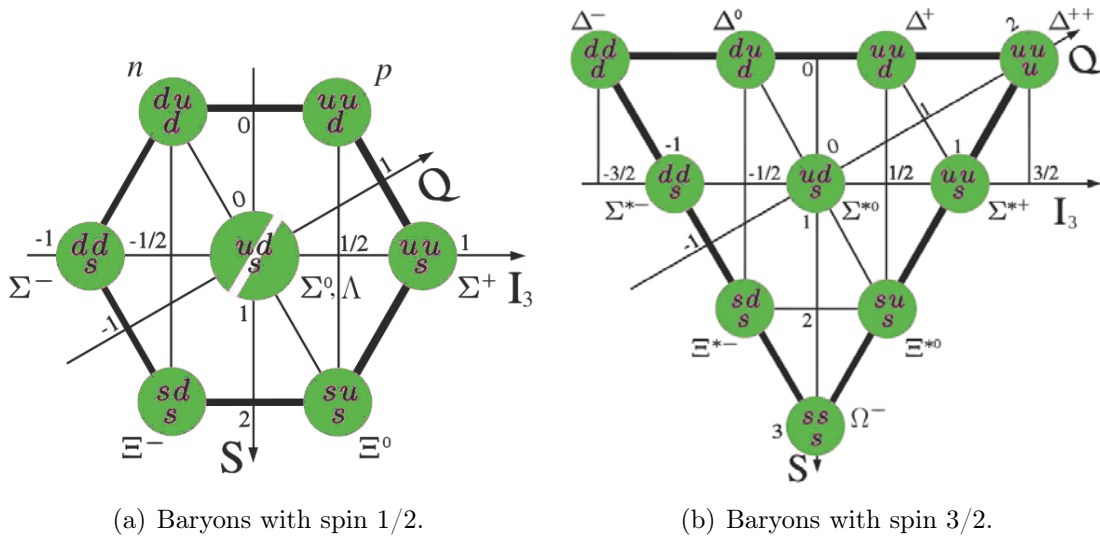
Figure 1.5: The lightest baryon octet and decuplet.

The classification into the spin $3/2$ decuplett predicted a new particle, the Ω^-, which was discovered 1964 [Bar64] and supports the quark model.

Replacing the strange quark with a charm, bottom or top quark leaves the name of the particle unchanged, only it gets an additional index, refering to the flavour of the quark.

1.3. The Fundamental Forces

Only four fundamental forces are necessary to describe what keeps the world at heart together. To explain how objects interact which each other we know gravitation and the electromagnetic force in the long range distances and the strong and weak forces in the short range distances.

The main characteristics of the four forces are summarized in the tables 1.5 and 1.3. In the following sections the fundamental interactions will be described more detailed.

Interaction	Current Theory	Rel. Strength	r Behaviour	Range [m]
Strong	QCD[2]	10^{38}	1	10^{-15}
EM	QED[3]	10^{36}	$\frac{1}{r^2}$	∞
Weak	Electroweak	10^{25}	$\frac{d}{dr}\left(\frac{\exp(-r \cdot m_{W,Z})}{r}\right)$	10^{-18}
Gravitation	GR[4]	1	$\frac{1}{r^2}$	∞

Table 1.5: Properties of the fundamental forces.

1.3.1. Gravitation

Gravitation is well known for everybody as the force which lets things fall down to the ground. It is an attractive force between two massive objects which can be described by Newtons law:

$$F(r) = G\frac{m_1 m_2}{r^2} \tag{1.3}$$

where G is the gravitational constant. The force is well known from e.g. measurements of the orbits of the planets (Kepler) or free fall experiments (Galilei). Gravitation is a quite weak force in energy scales below 10^{19} GeV and can be neglected in this case compared to the other three fundamental forces.

In the general theory of relativity Albert Einstein invented the entity of space, time and matter, which leads to a four-dimensional spacetime. Here, matter can change the structure of the spacetime and the gravitation is just a consequence of the space-time

---

[2]**Q**uantum **C**hromo **D**ynamics
[3]**Q**uantum **E**lectro **D**ynamics
[4]**G**eneral **R**elativity

geometry.

Unfortunately, the general theory of relativity, describing the macroscopic cosmos and the quantum theory, describing the microscopic cosmos, are mathematically not compatible. That is why gravitation is the only interaction which is not connected to the standard model up to now.

1.3.2. The Electromagnetic Force

The electric force acts between objects which carry electrical charges and can be described by the Coulomb law. For unlike charges the force is attractive, for like charges repulsive. Going from static charges to moving charges it was observed that an electric current creates a magnetic field and a moving magnetic field induces an electric current. That leads to the conclusion that the electric and the magnetic force are just two aspects of one unified force, the electromagnetic force.

Quantum Electro Dynamics (QED) is the field theory describing electromagnetic processes. Its the most precise theory in science so far. The strength of the interaction between charged particles and photons - as mediators of the electromagnetic force - is specified via the coupling constant, the so-called fine structure constant.

$$\alpha = \frac{e^2}{4\pi\hbar c} \approx \frac{1}{137} \tag{1.4}$$

The electromagnetic force has an infinite range due to its massless gauge boson.

1.3.3. The Weak Force

The weak force acts on all fermions. Accordingly, all elementary particles have a weak charge. Weak interactions are difficult to measure, because their interaction strength is, like the name implies, weak compared to the electromagnetic and the strong interactions. The weakness comes from the mass of their gauge bosons, 80 GeV ($W^{\pm}$) and 91 GeV (Z^0). In contrast, the photon and the gluons as the mediators of the electromagnetic and strong force are massless.

The cross section of an interaction is proportional to $|M_{fi}|^2$. The matrix element can be calculated to:

$$M_{fi} \propto \frac{g^2}{q^2 - m_B^2} \tag{1.5}$$

with the weak coupling g, the momentum transfer q and the mass of the gauge boson m_B.

Only if the energy is in the same order like the masses of the gauge bosons $E \cong m_{W,Z}$,

the electromagnetic and the weak force become comparable in strength (figure 1.6). In this energy regime weak interaction can be measured e.g. in processes where:

- Neutrinos are involved.

- The flavour of the quark changes.

- Parity is violated maximally.
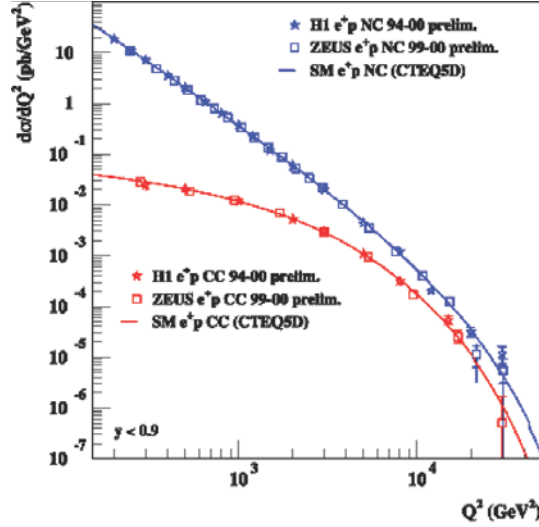
Figure 1.6: Electroweak unification. Going to high Q^2 the electromagnetic and weak force become comparable in strength.

The most prominent example for a weak interaction is the β-decay. Here a down quark converts into an up quark, so the neutron changes to a proton. The process is illustrated in figure 1.7.

The weak and the electromagnetic force can be seen as two aspects of one unified interaction, the so-called electroweak force. S. Glashow, A. Salam and S. Weinberg introduced in 1967 a formalism, where the weak isospin was introduced as a new quantum number. The third component of the weak isospin triplet ($T_3(W^+) = +1$, $T_3(W^-) = -1$ and $T_3(W^0) = 0$) should be conserved in reactions with charged currents. With the weak isospin singlet $B^0(T = 0, T_3 = 0)$ the two neutral vector bosons can be described as orthogonal linear combinations of the W^0 and the B^0:

$$|\gamma\rangle = \cos\theta_W \left|B^0\right\rangle + \sin\theta_W \left|W^0\right\rangle \tag{1.6}$$

$$\left|Z^0\right\rangle = -\sin\theta_W \left|B^0\right\rangle + \cos\theta_W \left|W^0\right\rangle \tag{1.7}$$

with the Weinberg angle $\cos\theta_W = \frac{M_W}{M_Z}$ in analogy to the Cabibbo angles θ_C in the CKM matrix.

In 1979 S. Glashow, A. Salam and S. Weinberg were honored for their work with the Nobel prize.
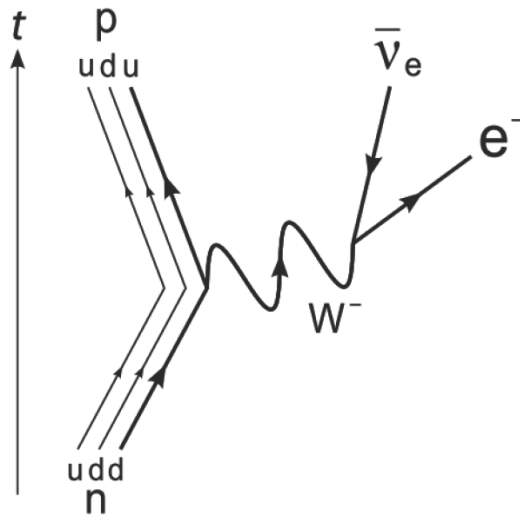
Figure 1.7: Feynman diagram of the β^- decay.

1.3.4. The Strong Force

Described by the Coulomb law, there is an attractive force between opposite sign charges and a repulsive force between same sign charges. As a consequence the protons in the nucleus should repel each other. But they are bound in the nucleus due to the strong force which is much stronger than the electromagnetic force for light nuclei.
Strongly interacting particles are described within the field theory Quantum Chromo Dynamics. These are the quarks and gluons, carrying a colour charge. Even though the exchange bosons of the strong interaction, the gluons, are massless the range of the strong force is limited. Because of the colour charge the gluons carry, they can couple to each other. Chapter *Hadrons in a medium* will focus on the topic strong force and its consequences.

1.4. Mass

The standard model in its original form has only massless particles included. To solve the problem, in 1964 Peter Higgs postulated the so-called Higgs mechanism. The vacuum is not empty, so that the massless particles are decelerated in that field which gives them a mass. The mediator of the Higgs field is the Higgs boson. It is predicted to be heavier than 114 GeV. The Large Hadron Collider (LHC) at CERN tries to find the Higgs boson which would confirm the theory of the standard model. But the Higgs mechanism does not give an answer to the question why some particles are more

massive than others.

In the world we live in, it seems to be natural that the sum of the individual parts of a compound system have the same mass than the composed system itself. The mass of ordinary matter comes from the masses of protons and neutrons which consist of up and down quarks. I.e. the proton has a mass of $m_p = 938$ MeV, the mass of the three quarks is only in the order of 15 MeV. This big mass difference cannot be explained by binding energy effects.

Corresponding to Einsteins famous equation of special relativity $E = mc^2$ mass is equivalent to energy. Turning the statement around implies mass can be explained in terms of energy. Energy is stored in the motion of the quarks and in the colour gluon fields that connect them. This makes the proton so massive.

To see if the mass of a hadron really is related to the strong interaction, one can put the hadrons into a strongly interacting enviroment, e.g. a nucleus. That is one way looking for possible in-medium modifications.

In the next chapter the underlying theory (QCD) with its symmetries and the theoretical predictions for in-medium modifications will be described.

Chapter 2.

Hadrons in the Nuclear Medium

Hadrons are composite systems made out of quarks and gluons, underlying the strong force which is decribed within the Quantum Chromodynamics (QCD).

In vacuum the specific properties of a hadron like its mass and life time are well known. The question arises, if these properties stay unchanged if the hadron is embedded in a strongly interacting enviroment like a nucleus and if these possible modifications are measurable.

This chapter discusses the relevant symmetries of QCD and will give an overview over the theoretical predictions and the experimental access to in-medium modifications of a hadron.

2.1. Quantum Chromo Dynamics

Nowadays QCD is established as the fundamental theory of strong interactions. At high energies one can observe quarks and gluons as active degrees of freedom e.g. in deep inelastic scattering. Quarks can be considered to be quasi free, weakly interacting particles. This phenomenom is known as asymptotic freedom. Nonetheless, it is not possible to isolate single free quarks and gluons. This is due to the strong force which stays constant with increasing distance between quarks. The constancy of the strong force originates from the linear part of the potential which is described as:

$$V(r) = -\frac{4}{3}\alpha_s\frac{1}{r} + \sigma r \qquad (2.1)$$

with the strong coupling constant α_s and the string tension σ.

At high energies (equivalent to small distances) the strong coupling constant decreases $\alpha_s(Q^2 \to \infty) \ \to 0$ (see figure 2.1) and QCD is a perturbative theory.

At low energies (equivalent to large distances) one observes hadrons, which are composite systems of quarks and gluons. They are confined within hadrons. In this energy regime the strong coupling constant strongly increases so that QCD can no longer be treated as a perturbative theory.
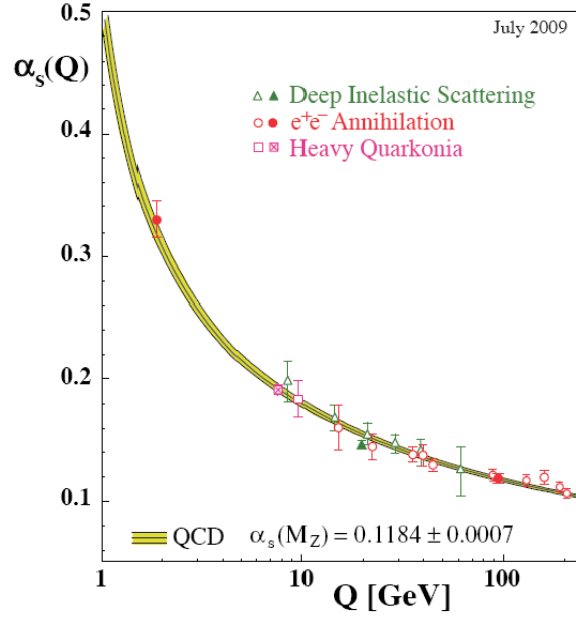
Figure 2.1: Q^2 dependence of the strong coupling constant α_s ([PDG08]).

2.1.1. Symmetries of QCD

Looking at the theory of strong interactions, QCD can be expressed in terms of their Lagrangian and their symmetries underlying all strong interactions. The Lagrangian is given by:

$$\mathcal{L}_{QCD} = \bar{q}\left(i\gamma^\mu D_\mu - M\right)q - \frac{1}{4}G_{\mu\nu}G^{\mu\nu} \tag{2.2}$$

with the quark field q, the Dirac matrices γ^μ and the covariant derivative D_μ. M leads to the quark mass matrix and $G_{\mu\nu}$ is the gluon tensor.

One big advantage of the Lagrangian formalism is that symmetries lead to conserved quantities, e.g. the number of baryons. There are two further approximate symmetries:

1. **Center symmetry**: is an exact symmetry for infinitely heavy quarks $m_q \to \infty$ and therefore related to confinement. In the limit of vanishing quarks the center symmetry is spontaneously broken, with the Polyakov loop acting as the order parameter.

2. **Chiral symmetry**: is an exact global symmetry of QCD in the limit of massless quarks $m_q \to 0$. Chiral symmetry is broken on the hadronic level.

2.1.2. Chiral Symmetry

Chirality describes the spin orientation of a massless particle relative to its direction of motion:

$$h = \frac{\vec{s} \cdot \vec{p}}{|\vec{s}| \, |\vec{p}|} \tag{2.3}$$

If the spin is pointing in the same direction the Eigenvalue is $+1$ (right handedness), if the spin points in the opposite direction the Eigenvalue is -1 (left handedness). Thus, massless particles can either be right or left handed, but they cannot transform into each other like illustrated in figure 2.2. This leads to chirality as a conserved quantity.
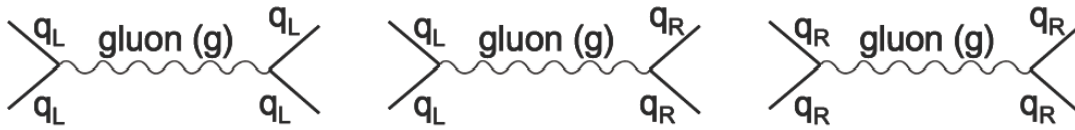
Figure 2.2: Quark handedness is conserved in strong interactions.

But we do not have massless particles. Nonetheless, comparing the masses of the three lightest quarks with the energy scale of QCD ($\Lambda_{QCD} \cong 200$ MeV), the masses of the up and down quark can be neglected:

$$\frac{m_u}{\Lambda_{QCD}} \approx 1,5 \cdot 10^{-2}, \qquad \frac{m_d}{\Lambda_{QCD}} \approx 2,5 \cdot 10^{-2}, \qquad \frac{m_s}{\Lambda_{QCD}} \approx 5 \cdot 10^{-1} \tag{2.4}$$

In this so-called chiral limit the two lightest quark masses are assumed to be $m_{u,d} \approx 0$. Here the QCD Lagrangian acquires an exact global symmetry (chiral symmetry) under independent SU(2) rotations of the left handed and right handed quarks:

$$q_L \rightarrow U_L q_L, \qquad q_R \rightarrow U_R q_R \tag{2.5}$$

with U_L, U_R being the global SU(2) matrices.

According to Noether's theorem, this symmetry leads to two conserved quantities: the vector current and the axial current

$$J_V^{\mu a} = \bar{q} \gamma^\mu \tau^a q, \qquad J_A^{\mu a} = \bar{q} \gamma^\mu \gamma^5 \tau^a q \tag{2.6}$$

with the quark fields q and the isospin matrices τ^a. On the quark level this means, states which can be rotated into each other by this symmetry operation have the same Eigenvalues. If the same holds for the hadronic sector one would expect chiral partners (same spin but opposite parity) to be degenerate in mass: $m(J^+) = m(J^-)$.

In figure 2.3 some states observed in nature are shown together with their chiral partners. It is clearly visible that they are not degenerate in mass. The mass split is even of the order of the hadron masses themselves. Consequently, chiral symmetry is spontaneously broken on the hadronic level.

19

M(S_{11}) = 1535 MeV
$J^P = \frac{1}{2}^-$

M(σ) = 600 MeV
$J^P = 0^+$

M(a1) = 1260 MeV
$J^P = 1^+$

≈600 MeV

≈470 MeV

≈490 MeV

M(N) = 938 MeV
$J^P = \frac{1}{2}^+$

M(π) = 135 MeV
$J^P = 0^-$

M(ρ) = 770 MeV
$J^P = 1^-$
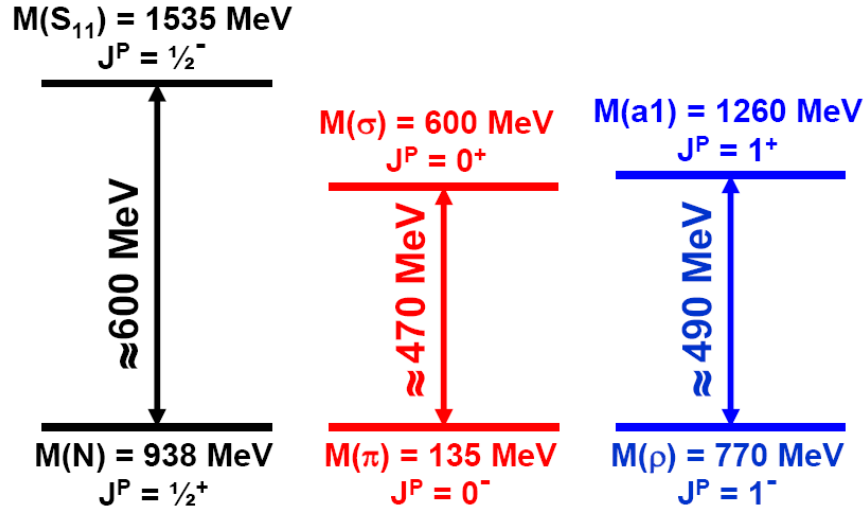
Figure 2.3: Mass splittings between chiral partners in the baryon and meson sector.

2.1.3. Chiral Symmetry Breaking and Restoration

A symmetry is spontaneously broken if the Lagrangian is invariant under rotations while the ground state is not. To illustrate this, figure 2.4 shows two rotational potentials. In figure 2.4(a) the ground state is located in the center of the potential, the

(a)

(y,π)

(x,σ)

(b)

(y,π)

(x,σ)
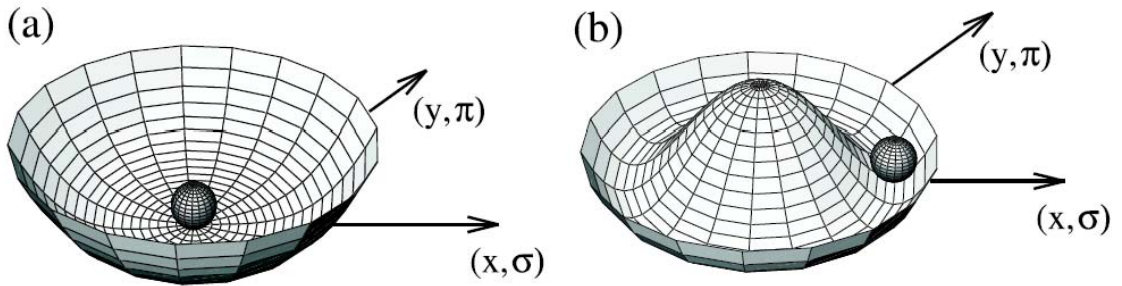
Figure 2.4: Potential illustrating the spontaneous breaking of chiral symmetry. (a) No spontaneous breaking of symmetry. (b) Spontaneous breaking of symmetry. The plot was taken from [Koc95].

potential is rotationally invariant. In figure 2.4(b) the center of the potential is a local maximum and therefore not stable. The ground state is some distance away which

breaks the rotational symmetry spontaneously.

Assuming that the effective QCD-Hamiltonian has a similar shape to the potential in figure 2.4(b), the x and y coordinates are replaced by the σ field for massive states and the π field for massless states. Rotational excitations along the π field do not cost energy. As a consequence massless particles are predicted, the so-called Goldstone bosons. The number of Goldstone bosons is $n_f^2 - 1$ where n_f is the number of massles quarks. Taking only the up and down quark as massless, there are three Goldstone bosons: π^0, π^+, π^- which are indeed not massless.

The small finite quark masses lead to an explicitly broken chiral symmetry and the QCD-Hamiltonian is no longer symmetric. Including non vanishing quark masses in the Lagrangian, the potential of figure 2.4(b) will slightly be tilted like it is shown in figure 2.5. Here rotational excitations along the π field do cost energy; the pions become massive particles.
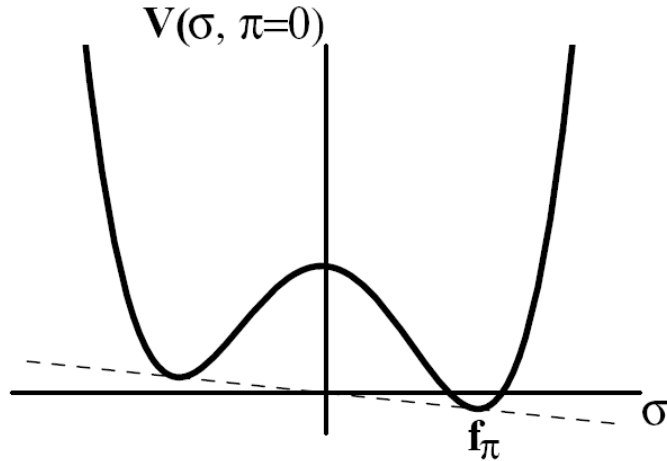
Figure 2.5: Spontaneous and explicit breaking of chiral symmetry. The plot was taken from [Koc95].

On the hadron level chiral symmetry is spontaneously and explicitly broken. But there are theoretical predictions that chiral symmetry is (partly) restored with increasing temperature or density. Therefore the explicit symmetry breaking has to be small. This seems reasonable, since the quark masses are small compared to the energy scale Λ_{QCD}.

Chiral symmetry is spontaneously broken due to the non-vanishing expectation value of the chiral condensate $\langle q\bar{q} \rangle \neq 0$, which represents the order parameter for the breaking of this symmetry. In figure 2.6 the chiral condensate is shown as a function of density and temperature. If the quark condensate drops to a value of zero, chiral symmetry is fully restored. Even at normal nuclear matter density ρ_0 a reduction of

30% of the chiral condensate is predicted which leads to a partially restored chiral symmetry. With the restoration of chiral symmetry one would expect a change of the properties of a hadron. The degeneracy of parity doublets should be recovered.
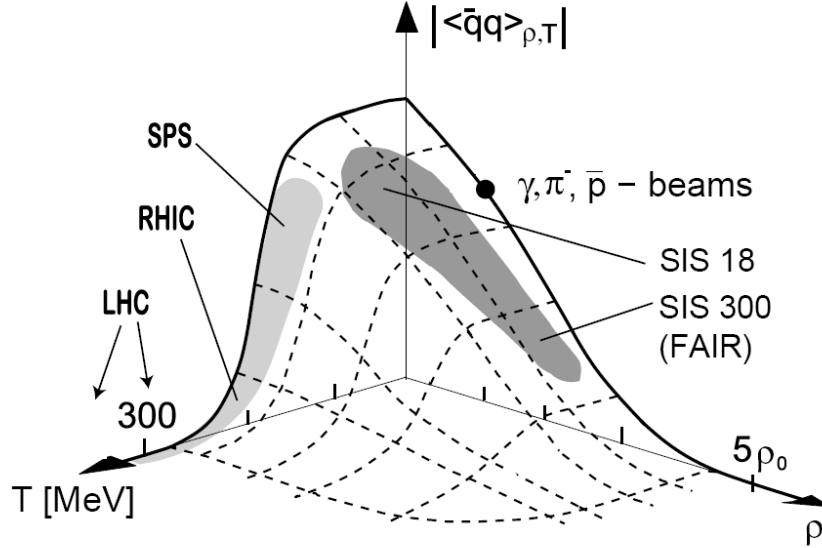
Figure 2.6: The chiral condensate as a function of density ρ and temperature T. Increasing density or temperature leads to a dropping of the chiral condensate. The shaded areas show the field which can be accessed with the actual particle accelerators.

2.2. In-Medium Effects

As already pointed out in the beginning of this chapter, the properties of a meson which are proposed to be modified are its width and life time, if the environment changes from vacuum to nuclear matter.

2.2.1. Collisional Broadening

Embedding a meson in a nuclear medium gives the meson the chance to interact with the nucleons. Due to these collisions the total width of the meson gets an additional

contribution. The total width Γ_{tot} is then given by the sum of the vacuum decay width Γ_{vac} and the collisional width Γ_{coll}.

$$\Gamma_{tot}\left(\mu, |\vec{p}|, \rho\right) = \Gamma_{vac}\left(\mu\right) + \Gamma_{coll}\left(\mu, |\vec{p}|, \rho\right) \tag{2.7}$$

Because of interactions with nucleons, the meson gets further decay possibilities due to additional inelastic channels, e.g. $\omega N \to \pi N$. This leads to an absorption of the ω meson and thus to a decreased life time τ which is directly connected to the total width of the meson.

$$\Gamma_{tot} = \frac{\hbar}{\tau} \tag{2.8}$$

2.2.2. Pole Mass Shift

A shift in the pole mass is expected, if the chiral symmetry is restored at high temperatures or baryonic densities.

Already two decades ago V. Bernard and U.-G. Meißner [Ber88] predicted on the basis of the Nambu-Jona-Lasinio model a restoration of chiral symmetry on the hadronic level. Going to high baryonic densities, the chiral condensate is predicted to vanish, therefore the chiral partners should be degenerate in mass as it is shown in figure 2.7. Here the mass of the scalar meson σ is predicted to drop considerably with increasing density whereas the mass of the vector mesons ρ, ω are almost independent of density.

The Brown-Rho-Scaling [Bro91] predicted that the in-medium hadron masses scale the same way as the chiral condensate. They predicted a drop of the in-medium mass by about 20% at normal nuclear matter density.

$$\frac{\langle 0^* | q\bar{q} | 0^* \rangle}{\langle 0 | q\bar{q} | 0 \rangle} = \frac{m_N^*(\rho_0)}{m_N} = \frac{m_{\sigma,\rho,\omega}^*(\rho_0)}{m_{\sigma,\rho,\omega}} \approx 0.8 \tag{2.9}$$

T. Hatsuda and S. H. Lee developed a consistent treatment of QCD sum rules in the nuclear medium [Hat92]. They derived a linear scaling law of the pole mass with respect to the density:

$$\frac{m_{\rho,\omega}^*(\rho_0)}{m_{\rho,\omega}} = 1 + \alpha\frac{\rho}{\rho_0} \tag{2.10}$$

α is a free parameter allowing for shifts of the in-medium mass in both directions. Here the parameter was estimated to be $\alpha = -0.16 \pm 0.06$ which is consistent with the result obtained by Brown and Rho ($\alpha = 0.20$).

In these calculations only the strength of a possible pole mass shift was investigated.
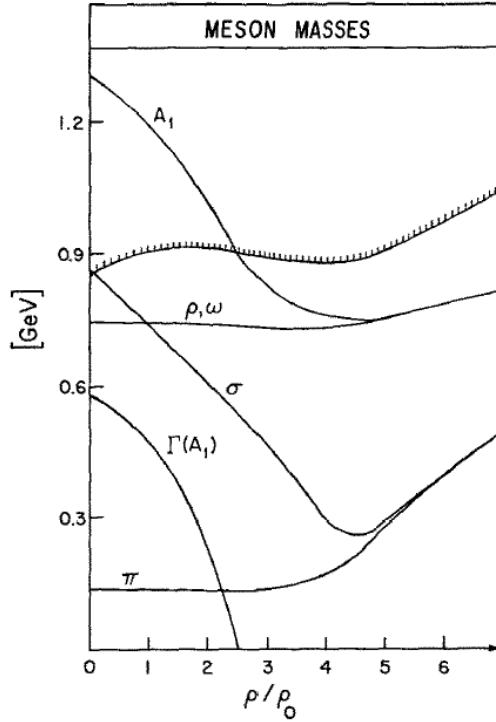
MESON MASSES

Figure 2.7: The meson masses as a function of density. The chiral partners $\sigma - \pi$ and $A_1 - \rho$ become degenerate in mass with increasing density.

But to learn more about how the shift is realized, hadronic models are necessary to describe the specifics of in-medium changes. Several models are described in the next section.

2.3. Theoretical Predictions for In-Medium Effects

M. F. M. Lutz, Gy. Wolf and B. Friman [Lut02] constructed a relativistic and unitary approach to pion-nucleon and photon-nucleon reactions. The final states πN, πN, ρN, ωN, ηN, $K\Lambda$, $K\Sigma$ are taken into account. This model generates dynamically nucleon resonances in terms of quasi-local interaction vertices. The photon-induced processes are described using a generalized vector-meson dominance assumption.

Their predictions for the ρ and the ω meson are shown in figure 2.8.

For the ρ meson, shown in the left panel of figure 2.8, the width of the signal increases going from vacuum to twice normal nuclear matter density. Also the development of a low mass shoulder was observed, due to the mixing with baryon resonances.
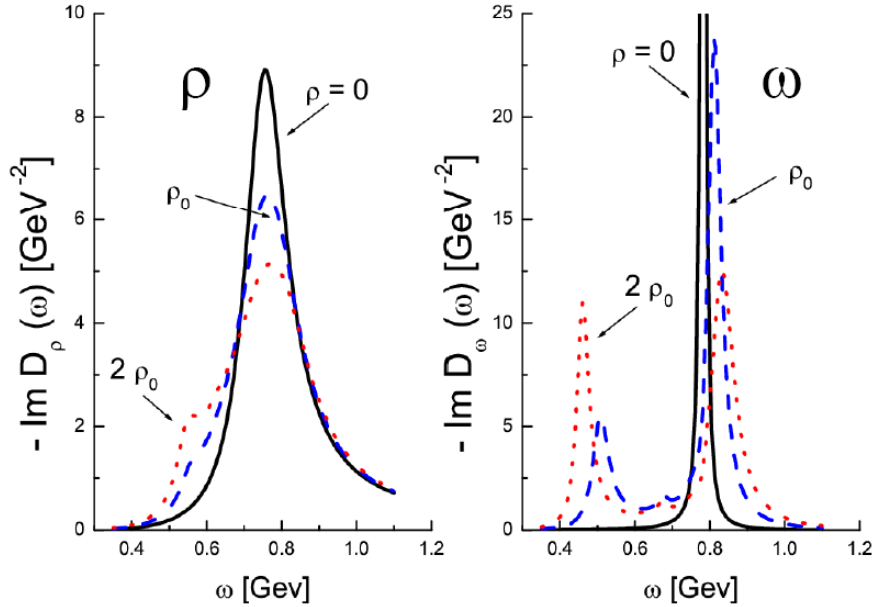
Figure 2.8: The imaginary parts of the ρ meson (left panel) and the ω meson (right panel) propagators in vacuum (solid line) and in nuclear matter at $\rho = \rho_0$ (dotted line) and at $\rho = 2\rho_0$ (dashed line) [Lut02].

The result for the ω meson is shown in the right panel of figure 2.8. With increasing density, an upward mass shift ($\approx$ 40 MeV) was observed. The peak-like structure around 0.5 GeV arises due to the coupling of the ω meson to the $D_{13}(1520)$ and the $S_{11}(1535)$ nucleon-hole states.

In [Mue06c] the ωN forward scattering amplitude was calculated with an unitary coupled-channel effective Lagrangian model that has been applied successfully to the combined analysis of pion-induced and photon-induced reactions. This model includes all resonance states with quantum number

$$J^P = \frac{1^{\pm}}{2}, \ \frac{3^{\pm}}{2}, \ \frac{5^{\pm}}{2} \tag{2.11}$$

up to masses of 2 GeV. This was used to calculate the self energy of the ω meson also for finite momenta.

Going from $\rho = 0$ to $\rho = 2\rho_0$ the peak of the ω spectral function is slightly shifted to higher masses as it is shown in figure 2.9. In addition the signal is broadened due to resonance-hole excitations. Due to the coupling to the $S_{11}(1535)$ resonance a second peak appears around 550 MeV.

In [Kli99] an effective Lagrangian based on $SU(3)_L \otimes SU(3)_R$ symmetry is used to
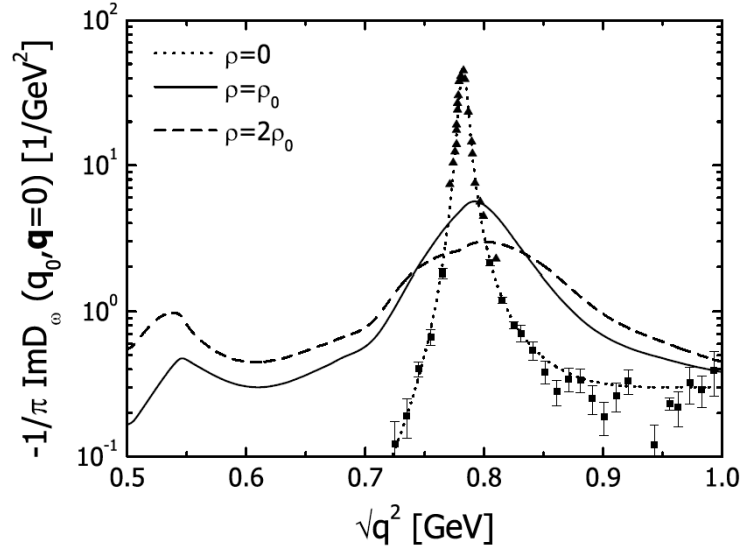
Figure 2.9: The ω spectral function for an ω meson at rest. The spectral function of a free ω meson is decribed by the dotted line going through the data points. Increasing the density to $\rho_0 = 0.16 fm^{-3}$ and $2\rho_0$ leads to the ω spectral function with the solid and the dashed curve, respectively. The plot was taken from [Mue06c].

calculate the ω spectral function. The result is shown in figure 2.10. Going from $\rho = 0$ to $\rho = \rho_0$ the ω meson mass is shifted downwards by about 15% from the free ω meson mass. The width is predicted to be five times larger than the free width.

Summarizing, the theoretical predictions for the ω meson so far give no clear conclusion. The ω meson is predicted to be shifted upwards in mass with no significant broadening of the width ([Lut02]), the same trend to an upward mass shift is seen in [Mue06c] but with an additional broadening in width. In contrast [Kli99] predict that the ω meson is shifted downwards in mass with an increased width.

2.4. GiBUU Transport Code Calculations

The theoretical predictions presented in the last sections concern the spectral function of vector mesons. But the spectral function is not directly observable in experiments; it is folded with the branching ratio and the density distribution of the nuclear medium. To relate the in-medium spectral function to measurable quantities the full propagation of vector mesons in a nuclear medium is needed. The Gießen theory group has
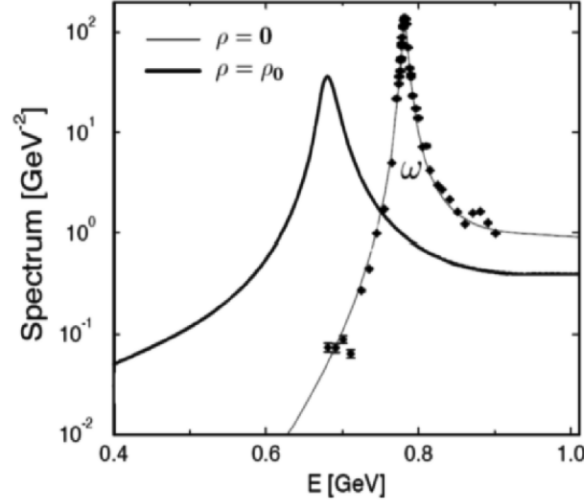
Figure 2.10: The ω spectral function in vacuum is given by the thin solid line through the data points and the theoretical prediction for $\rho = \rho_0$ is given by the bold solid line. The plot was taken from [Kli99].

developed a semi-classical BUU[1] transport model called *GiBUU*[2] for the numerical simulation of various nuclear processes, including collision and decay of particles in the medium. BUU models include a mean field potential which is generated by the sum of all nucleons and binds them together in the nucleus.

The dynamics are governed by the Boltzmann-Uehling-Uhlenbeck equation:

$$\left(\partial_t + \left(\nabla_{\vec{p}} H_i\right) \nabla_{\vec{r}} - \left(\nabla_{\vec{r}} H_i\right) \nabla_{\vec{p}}\right) f_i(\vec{r}, t, \vec{p}, \mu) = I_{coll}[f_i, f_j, ...] \tag{2.12}$$

It describes the time evolution of the phase space density f_i for different particle species $i, j, ...$ The decays and collisions of particles are described by the collision term I_{coll} while the Hamiltonian H_i contains the mean field potential.

In particular for the CBELSA/TAPS (Bonn) and CB/TAPS (Mainz) experiments three different scenarios were studied:

- No medium modification of the ω spectral function

- Collisional broadening with $\Gamma_{coll} = 150$ MeV

- Collisional broadening plus mass shift

---

[1]**B**oltzmann **U**ehling **U**hlenbeck

[2]http://gibuu,physik.uni-giessen.de

The mass shift was assumed to be given by:

$$m_\omega^* = m_\omega(\rho = 0) \cdot \left(1 - 0.16\frac{\rho}{\rho_0}\right) \tag{2.13}$$

For these three scenarios the lineshape of the ω meson was studied in two photon energy regimes 900 to 2200 MeV and 900 to 1300 MeV and afterwards compared to the experimental results.

2.5. Experimental Access to In-Medium Effects

In the following sections four different approaches to obtain informations on the modifications of a hadron in nuclear matter are discussed.

2.5.1. Lineshape Analysis

This is the analysis method used in this thesis. From the 4-momenta of the decay products the invariant mass of the ω meson is reconstructed. The shape of the signal may contain in-medium informations of the hadron, i.e. the signal can be broadend or the peak position can be shifted (see chapter 2.2). The main idea is to compare the ω meson lineshape for different target materials. If the specific properties of a meson are modified going from vacuum to a nuclear medium, the lineshape should differ for reactions with light nuclei (liquid hydrogen) and heavy nuclei (Niobium).

2.5.2. Momentum Analysis

A second Ansatz to obtain in-medium information from the ω decay is to look for the omega yield at different momenta. First theoretical GiBUU transport calculations show a promising difference in the momentum distribution among the four scenarios assuming no modification (red), collisional broadening (green) and collisional broadening plus mass shift (blue) and shift only (magenta) (figure 2.11).

2.5.3. Transparency Ratio

Experimentally the in-medium decay width of a particle can be deduced from its measured lineshape. But due to insufficient detector resolution it might be, that the analysis is not sensitive to the in-medium decay width.
Another approach to get access to the in-medim decay width is the so-called nuclear
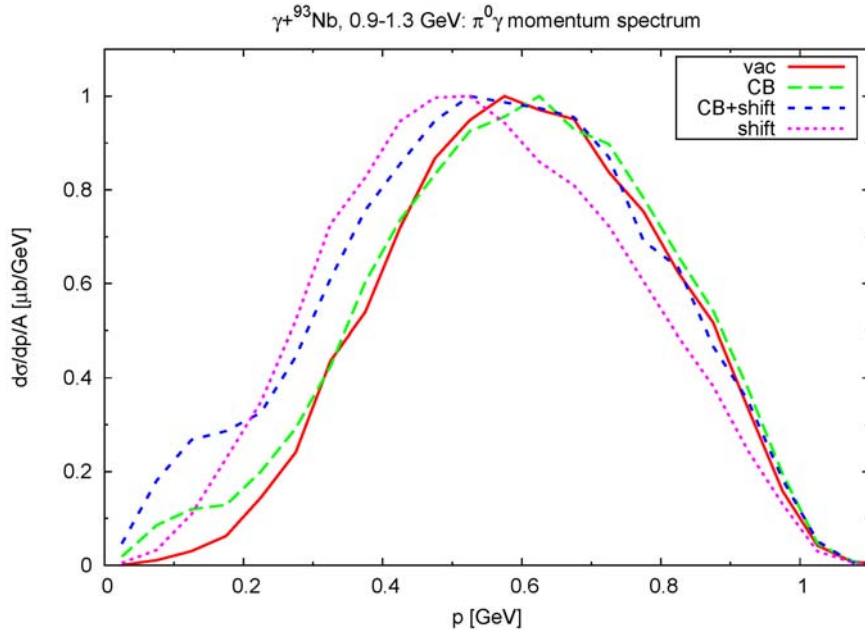
Figure 2.11: The ω yield as a function of its momentum for the four different scenarios: no in-medium modification (red line), collisional broadening (green line), collisional broadening plus mass shift (blue line) and shift only (magenta line) [Wei10].

transparency ratio. This method has already been applied in works on the ϕ meson [Mue06a]. Related to the topic of this thesis, former results obtained on the ω meson will be presented. Here, the transparency ratio is defined as:

$$T_A = \frac{\sigma_{\gamma A \to \omega X}}{A \cdot \sigma_{\gamma N \to \omega X}} \tag{2.14}$$

i.e. the ratio of the nuclear ω photoproduction cross section per nucleon within a nucleus with mass number A divided by the same quantity on a free nucleon. T describes the loss of flux of ω mesons in the nuclei and is related to the absorptive part of the ω nucleus potential and thus to the ω width in the nuclear medium. As shown in [Kot08], the transparency ratio of the ω meson for different target materials was determined and compared to two different theoretical calculations. The obtained transparency ratios were normalized to the carbon data to avoid systematic uncertainties. The results are shown in figure 2.12.

The data is shown in comparison to a Monte-Carlo type analysis by the Valencia group [Kas07] (left panel) and a BUU transport code calculation by the Gießen group [Mue06b] (right panel). In both cases the ω signal is strongly attenuated with increasing nuclear mass number. This is primary due to the strong absorption with increasing
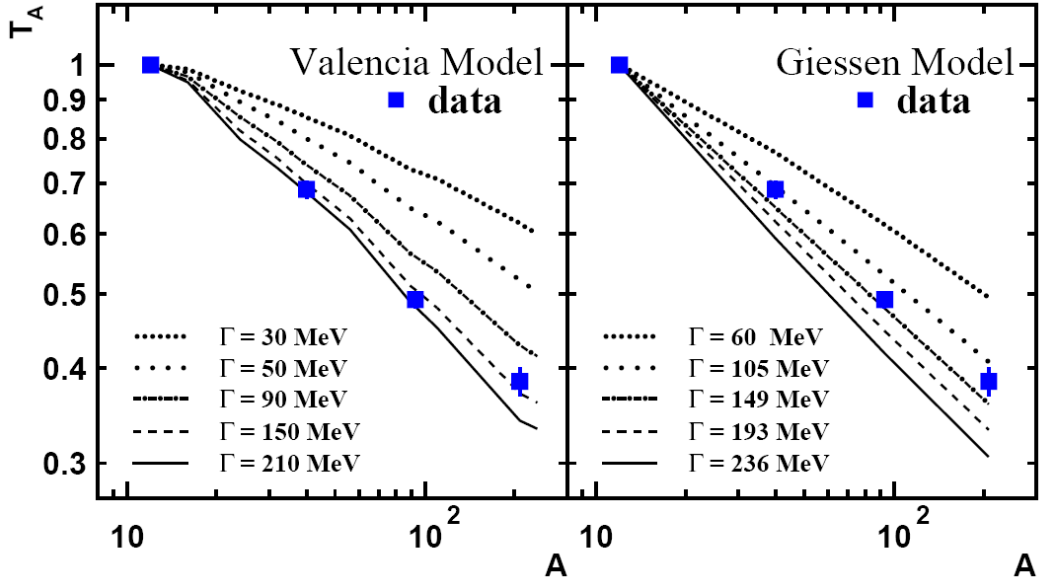
Figure 2.12: Experimentally determined transparency ratio for ω mesons normalized to carbon data. In the left panel the transparency ratio is compared to a Monte Carlo calculation, in the right panel to a BUU transport code calculation [Kot08].

nuclear matter density:

$$\Gamma_{med}(\rho(r)) = \Gamma_{med}(\rho_0)\frac{\rho(r)}{\rho_0} \tag{2.15}$$

where $\rho_0 = 0.16$ fm^{-3} is the normal nuclear matter density.

The in-medium decay width of the ω meson was determined from the transparency ratio to $130 - 150$ MeV which is approximately $16 \cdot \Gamma_{vac}$.

2.5.4. Excitation Function

For the excitation function the ω photoproduction cross section σ is plotted versus the energy of the incoming photons. The shape of the excitation function, in particular in the threshold region, can contain information about possible in-medium modifications. ω photoproduction on a free proton (e.g. lH$_2$ target) is only possible above the kinematic threshold energy, which can be calculated to:

$$E_{\gamma,thresh} = \frac{m_\omega^2 + 2 \cdot m_p \cdot m_\omega}{2 \cdot m_p} = 1108 MeV \tag{2.16}$$

According to equation 2.16, no ω mesons should be produced below 1108 MeV, i.e. the cross section should be zero. This can be seen in figure 2.13 where the ω excitation

function is shown. The data points measured by the SAPHIR collaboration belong to a production on liquid hydrogen. All points are above the production threshold energy.
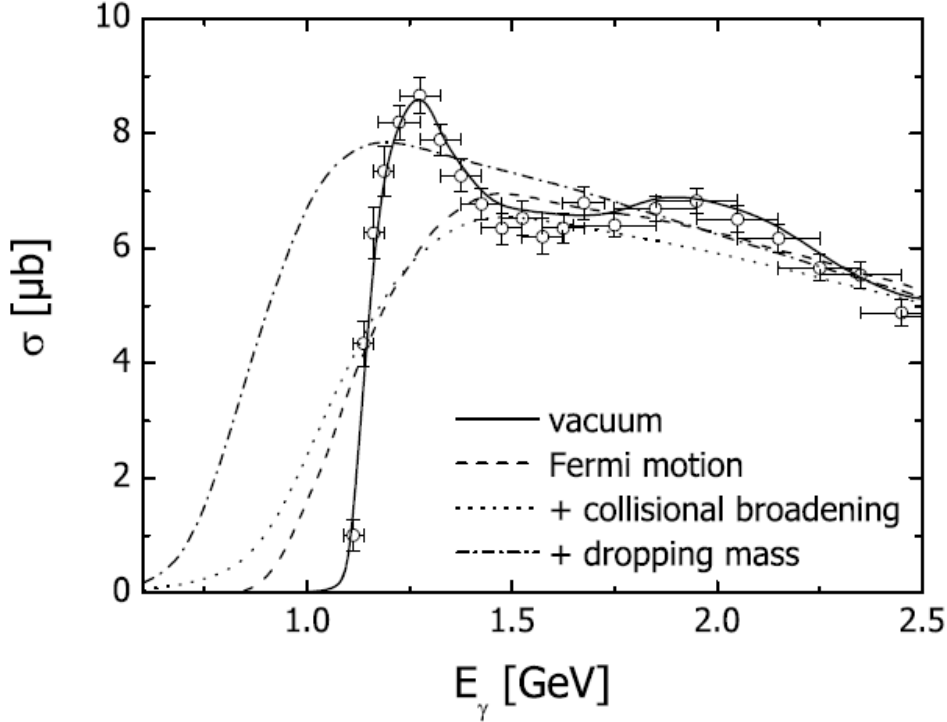
Figure 2.13: ω photoproduction cross section on the nucleon compared to the three different in-medium scenarios [Mue06b].

This threshold energy is of course lower for a coherent ω photoproduction on a nucleus. Then equation 2.16 is modified to:

$$E_{\gamma,thresh} = \frac{m_\omega^2 + 2 \cdot m_{nuc} \cdot m_\omega}{2 \cdot m_{nuc}} \qquad (2.17)$$

For the two solid targets used in the experiments analysed in this thesis the threshold energy for coherent production is:

$$E_{\gamma,thresh} \text{ (carbon)} = 809 \text{ MeV} \qquad (2.18)$$

$$E_{\gamma,thresh} \text{ (niobium)} = 786 \text{ MeV} \qquad (2.19)$$

Therefore also non-zero cross section values are expected below 1108 MeV. But the cross section for coherent ω photoproduction scales with the formfactor of the target nucleus squared $|F(q)|^2$; the effect is negligible.

Other effects can also cause a non-zero cross section below 1108 MeV. On the one hand, the nucleons in the target are not at rest, they have some Fermi momentum. On the other hand, due to additional decay channels offered by a solid target, the lifetime of the ω meson is reduced, it gets broader and due to the tail a production below threshold is possible.

As dicussed in chapter 2.2 also the mass of the meson can change in a nuclear medium which has an effect on the threshold energy according equation 2.16.

These three scenarios (fermi motion, collisional broadening and mass shift) were calculated by the Gießen theory group and are shown in figure 2.13 together with the data points.

More recently, B. Lemmer was investigating in his diploma thesis [Lem09] the ω excitation function on the solid targets carbon and niobium. He analysed the same data set like the ones used in this thesis. The analysis is still ongoing so that the final results cannot be presented here.

2.6. Former Experiments

According to various theoretical predictions for possible in-medium modifications of hadrons which have no clear conclusion, experiments are needed to prove or disprove the different scenarios. In the last years the focus was placed on experiments with short-lived vector mesons, i.e. ρ and ω meson. Two types of experiments can be used to get access to in-medium properties of hadrons:

- Heavy ion reactions

- Nuclear reactions with elementary probes

In the following section the recent obtained results for the ρ and the ω meson are described. First for two heavy ion collision experiments (CERES@SPS and NA60@SPS) and then for three experiments with elementary probes (CLAS@JLAB, E325@KEK and CBTAPS@ELSA).

2.6.1. CERES Experiment

With the CERES detector at the CERN SPS accelerator medium modifications of vector mesons were measured for the first time in ultrarelativistic heavy ion reactions. CERES was looking for the spectral shape of vector mesons $\rho, \omega, \phi \rightarrow e^+e^-$ in central Pb+Au collisions at 158 AGeV [Ada08]. Figure 2.14(a) shows the invariant mass spectrum after subtracting the combinatorial background. In the mass range from 300 MeV to 600 MeV an enhancement relative to the cocktail is observed. For a more

(a)   (b)
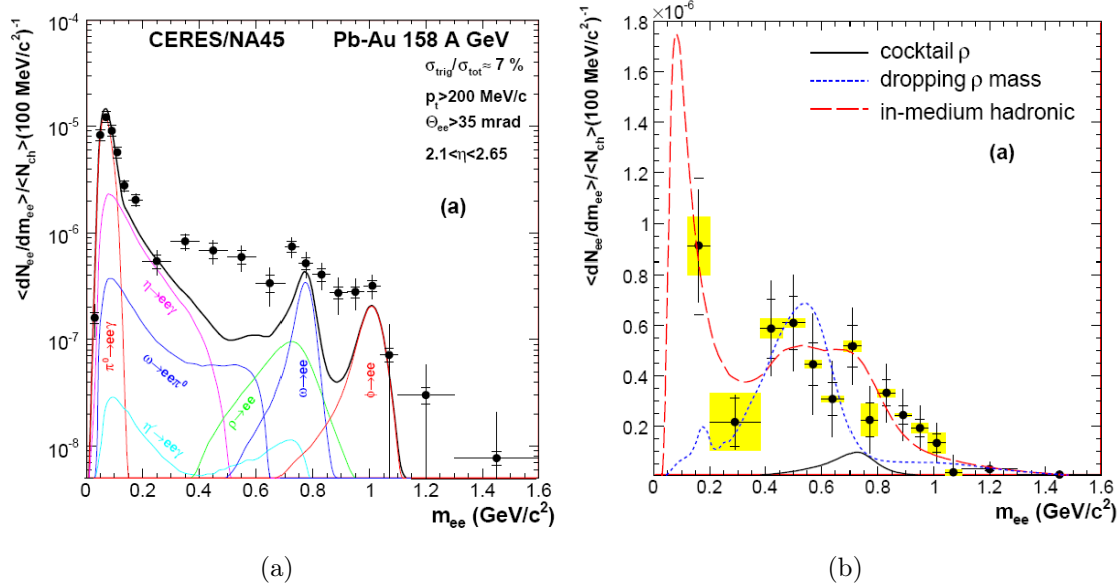
Figure 2.14: (a) e^+e^- invariant mass spectrum for central Pb+Au collisions. The contributions from different hadronic decays (solid line) cannot describe the shape of the data points in the mass region below the ϕ mass. (b) The cocktail subtracted data is compared to a broadening scenario (dashed line) and a mass shift scenario (dotted line) [Ada08].

detailed analysis of the ρ meson the contributions of the dilepton cocktail except for the ρ contribution was subtracted from the spectrum in figure 2.14(a). The result can be seen in figure 2.14(b) in comparison to two different theoretical scenarios. Within the limited statistics the data seems to favour the in-medium broadening scenario over the mass-shift scenario.

2.6.2. NA60 Experiment

The NA60 experiment at the CERN SPS used a 158 AGeV indium beam on a segmented indium target [Arn06]. The vector mesons are observed via their decay $\rho, \omega, \phi \rightarrow \mu^+\mu^-$, with particular interest of the ρ meson. Looking also at a dileptonic decay channel like the CERES experiment, NA60 improved statistics by a factor 1000 and the energy resolution by a factor two. By matching the tracks before and after the absorber in angle and momentum a mass resolution of 2.5% was achieved. In figure 2.15 the $\mu^+\mu^-$ invariant mass spectrum is shown. Clearly the peaks from $\omega, \phi \rightarrow \mu^+\mu^-$ are visible and can be subtracted from the invariant mass spectrum. The remaining part is attributed to the decay $\rho \rightarrow \mu^+\mu^-$. This leads to the conclusion that the ρ meson is strongly broadened in the medium, but it is not shifted in mass.
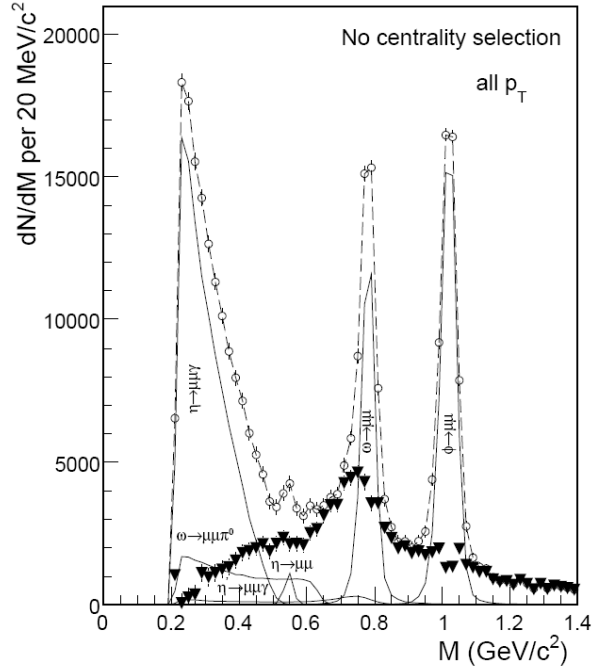
Figure 2.15: $\mu^+\mu^-$ invariant mass spectrum for In+In collisions at 158 AGeV. The open circles show the full spectrum after background subtraction. The black triangles show the ρ contribution after subracting the known hadronic decay sources [Arn06].

2.6.3. CLAS Experiment

For the experiment at Jefferson Laboratory electrons with energies up to 4 GeV from the CEBAF accelerator were used to produce a beam of bremsstrahlung photons. Bombarding various nuclear targets, the CLAS detector was used to identify the decay of vector mesons into lepton pairs $\rho, \omega, \phi \to e^+e^-$ with main focus on the properties of the ρ meson [Nas07]. Figure 2.16(a) shows the invariant dilepton mass spectrum after subtracting the combinatorial background. Figure 2.16(b) shows the invariant mass spectrum for $\rho \to e^+e^-$. From this a shift of the ρ meson mass was excluded, but a slight broadening of the signal was observed.

Due to limitations in the detector acceptance, only vector mesons with momenta larger than 800 MeV can be registered. This clearly reduces the number of in-medium decays, especially for the longer-lived particles (ω and ϕ meson). For the short-lived ρ meson this point is less crucial.
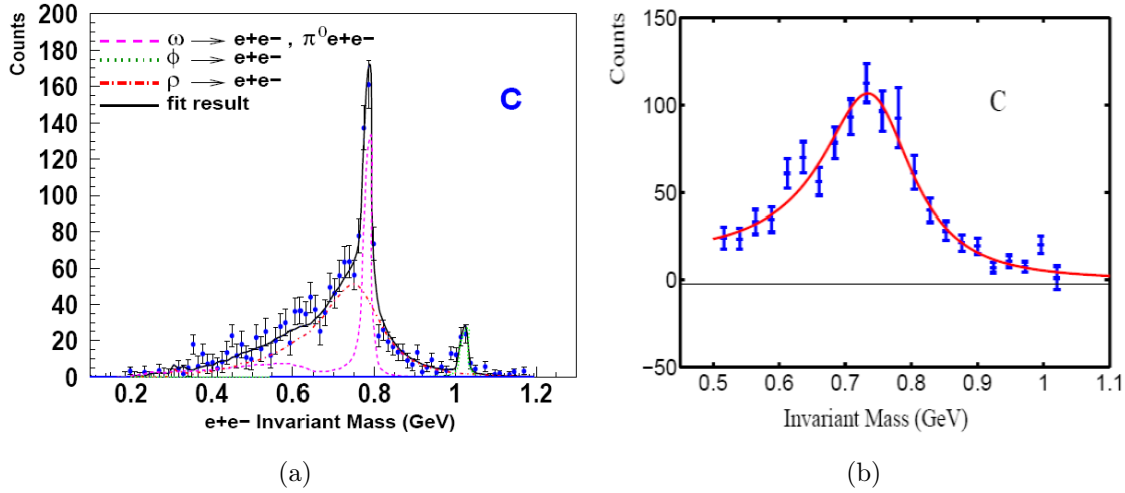
Figure 2.16: (a) e^+e^- invariant mass spectrum after subtracting the combinatorial background. (b) Invariant mass spectrum for the ρ meson decaying into e^+e^- [Nas07].

2.6.4. E325 Experiment

The experiment E325 has been performed at the KEK 12 GeV proton synchrotron. Possible modifications of the spectral shape of vector mesons in a nuclear medium were investigated in the decay channel $\rho, \omega, \phi \rightarrow e^+e^-$ [Nar06]. The shape of the e^+e^- invariant mass can be measured directly with a high mass resolution and high statistics. The focus lies on the detection of slow moving vector meson to increase the number of in-medium decays. The data shown in figure 2.17 shows an excess on the low mass side of the ω peak. It was concluded that the mass of the ρ as well as the mass of the ω meson is shifted downwards by 9 %. This is in good agreement with the theoretical prediction by Hatsuda-Lee with $\alpha = -0.09$.

2.6.5. The CBELSA/TAPS Experiment

In 2003 the CBELSA/TAPS experiment at Bonn was investigating possible in-medium modifications of the ω meson using electrons with energies up to 2.8 GeV from the ELSA accelerator to produce bremsstrahlung photons. The decay channel of interest was $\omega \rightarrow \pi^0\gamma$. The analysis of the niobium data set in the energy range 900-2200 MeV showed a shoulder at the lower mass side of the ω signal [Trn05]. This was interpreted as a signal from in-medium decays with a mass shift of 14 %.
Further studies showed that the extraction of the omega signal lineshape strongly depends on the determination of the background shape. A re-analysis of the data with a

(a)

(b)
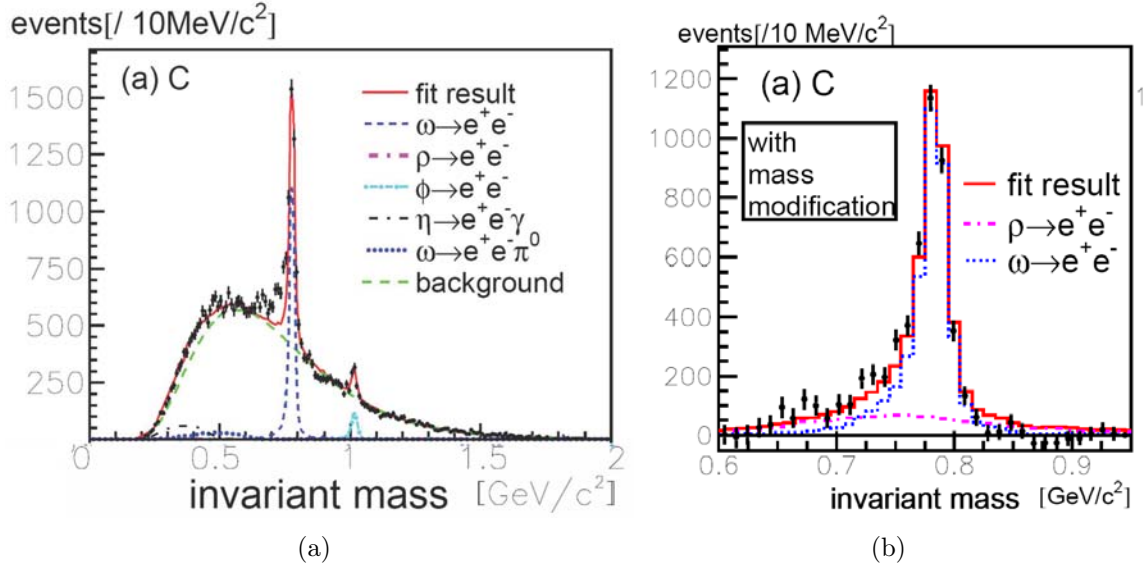
Figure 2.17: (a) e^+e^- invariant mass spectrum for the carbon target. (b) e^+e^- invariant mass spectrum. The combinatorial background as well as the shapes $\eta \rightarrow e^+e^-\gamma$ and $\omega \rightarrow e^+e^-\pi^0$ were subtracted [Nar06].

(a)

(b)
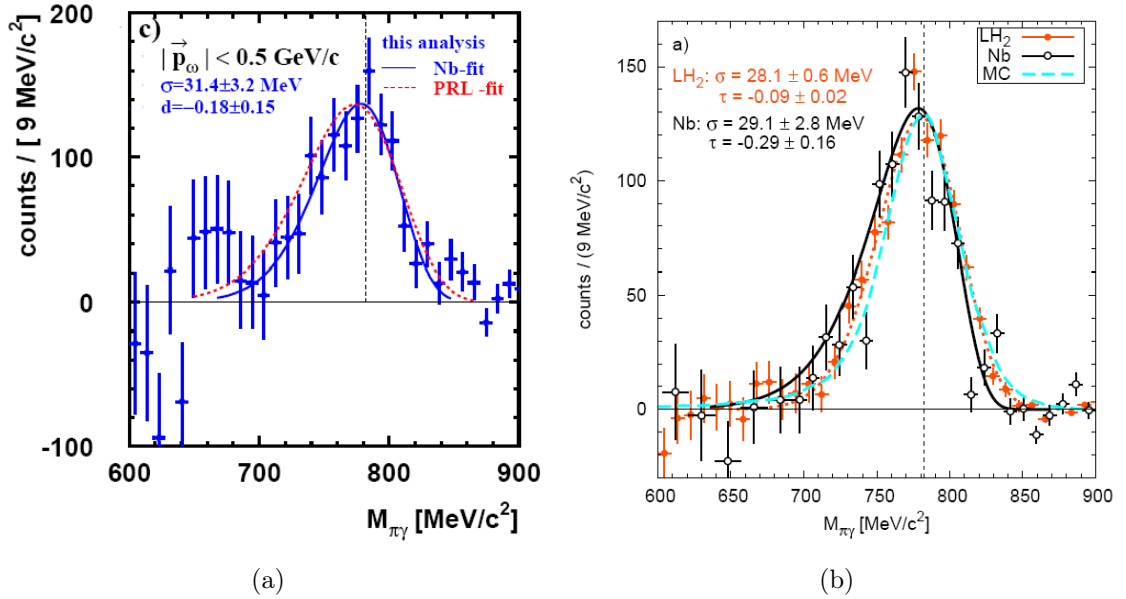
Figure 2.18: (a) $\pi^0\gamma$ invariant mass spectrum for the niobium target. The solid blue line is the fit of the re-analysis to the data, the dotted red line is the fit of the original analysis. (b) Niobium data compared to a fit to liquid hydrogen data (dotted line) and Monte Carlo simulations (dashed line) [Nan10b].

new background determination method was performed [Nan10a]. The obtained lineshape results were not inconsistent with the previously performed analysis predicting a mass shift, however they are also consistent with the reference signal (vacuum case: lH$_2$ target) where no mass shift is assumed (see figure 2.18). The conclusion is, that the lineshape is just not sensitive to possible in-medium modifications in this energy regime.

BUU transport code calculations predicted stronger deviations from the vacuum lineshape close to the ω photoproduction threshold $E_{\gamma,thresh} = 1108$ MeV. Due to the poor statistics in the lower energy range (900-1300 MeV) a second generation experiment with energies close to the production threshold was proposed. This is the purpose of this thesis.

2.7. The CB/TAPS Experiment in Mainz

2.7.1. Motivation

During the analysis of the CBELSA/TAPS data, BUU transport code calculations to this topic were performed from the Gießen theory group. Looking at the same decay channel $\omega \to \pi^0\gamma$, three different scenarios were studied:

- no medium modification

- collisional broadening

- collisional broadening + attractive mass shift of 16%

Two different energy ranges have been simulated: 900 to 2200 MeV and a region close to the ω production threshold ($E_{\gamma,thresh} = 1108$ MeV) 900 to 1200 MeV. The results for the $\pi^0\gamma$ invariant mass are shown in figure 2.19 for the higher energies (a) and for the lower energies close to threshold (b). In the left figure the three scenarios are not distinguishable, which is consistent with the experimental results obtained in the CBELSA/TAPS experiment in 2003.

But close to the threshold region a strong enhancement in the $\pi^0\gamma$ invariant mass spectrum for the collisional broadening plus mass shift scenario can be seen (right figure).

The CBELSA/TAPS experiment was not optimized to look at this low energy regime. Accordingly the statistics is too poor to favour or exclude one of the presented scenarios.

With the MAMI-C accelerator in Mainz and with photon energies up to 1400 MeV, an excellent tool is provided to study exactly the region where one expects to see possible modifications of the ω lineshape.

(a)   (b)
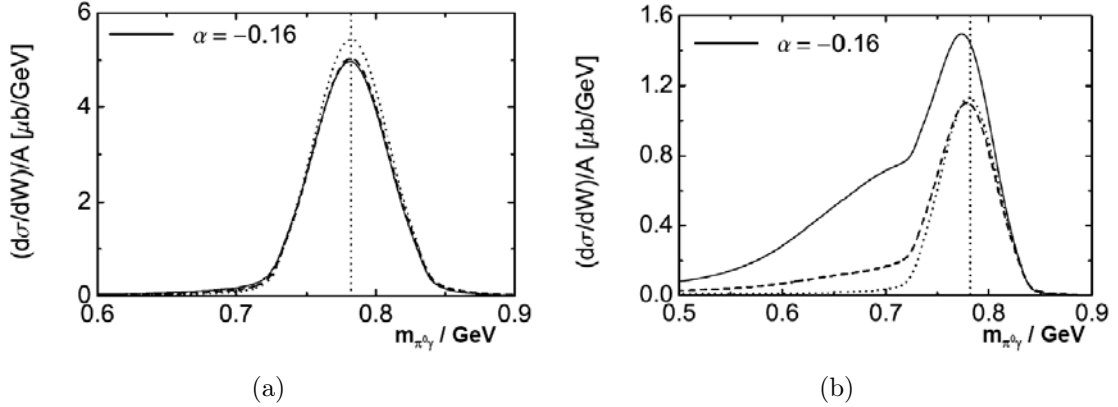
Figure 2.19: BUU simulations for three different scenarios: no medium modification (dotted line), collisional broadening (dashed line) and collisional broadening plus attractive mass shift of 16% (solid line). The left panel shows the $\pi^0\gamma$ invariant mass spectrum for 900 MeV to 2200 MeV. In the right panel the same spectrum is shown for 900 MeV to 1200 MeV. The plots were taken from [Gal08].

2.7.2. In-Medium Decays

To test the theoretically predicted in-medium modifications, experiments can study the specific properties of a hadron like its width or its life time if it is embedded in a strongly interacting environment. But not the hadron itself will be registered in the detector, only the decay products $H \to X_1 X_2$ can be detected. The in-medium mass μ of the hadron can be reconstructed by the four-momentum vector p_1, p_2 of the decay products:

$$\mu(\vec{p}, \rho, T) = \sqrt{p_1 + p_2} \qquad (2.20)$$

where $\vec{p}$ denotes the three-momentum of the hadron with respect to the nuclear medium. The in-medium mass μ depends on the density ρ and the temperature T.

To make sure that the hadron decays inside the nuclear medium, its lifetime has to be short so that the decay length is comparable to nuclear dimensions. Good candidates seem to be the light vector meson ρ, ω and ϕ. Their decay length is $\beta \cdot \gamma \cdot c \cdot \tau \approx 1.3$ fm, 23 fm and 46 fm, respectively. For the reactions of interest $\beta \cdot \gamma$ is in the order of one. To enlarge the amount of in-medium decays a cut on low meson momenta for the ω and the ϕ meson should be applied.

The experimentally observed mass distribution is a convolution of the spectral function with the branching ratio of the channel of interest.

$$\frac{d\sigma_{V \to final\ state}}{d\mu} \sim \mathcal{A}(\mu) \cdot \frac{\Gamma_{V \to final\ state}}{\Gamma_{tot}} = \frac{\mu \Gamma_{tot}}{\left(\mu^2 - m_V^2\right)^2 + \mu^2 \Gamma_{tot}^2} \cdot \frac{\Gamma_{V \to final\ state}}{\Gamma_{tot}} \qquad (2.21)$$

with

$$\Gamma_{tot} = \Gamma_{vac} + \Gamma_{med} \tag{2.22}$$

The in-medium width depends on the density which is not constant over the full range of the nucleus. Figure 2.20 shows schematically a density profile of a nucleus. The nearly constant density drops drastically if one comes closer to the surface.
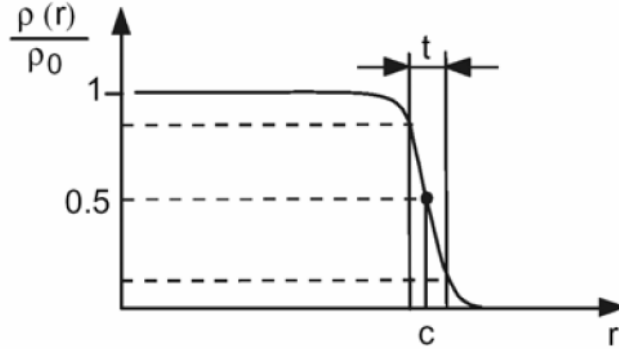
Figure 2.20: Density profile of a nucleus with radius c. Going closer to the surface the density drops.

In the low-density approximation the in-medium width can be calculated to:

$$\Gamma_{med}\left(\rho(r)\right) = \Gamma_{med}\left(\rho_0\right)\frac{\rho(r)}{\rho_0} \tag{2.23}$$

From the transparency ratio ([Kot08]) it is known that for the ω meson $\Gamma_{med} \approx 16 \cdot \Gamma_{vac}$, therefore $\Gamma_{tot}\rho/\rho_0$. Looking at equation 2.21 this implies that the second term is proportional to $\frac{1}{\rho/\rho_0}$. For masses μ near the pole mass m_V also the first term is proportional to $\frac{1}{\rho/\rho_0}$. In total this leads to a suppression of contributions with higher densities by a factor $\frac{1}{(\rho/\rho_0)^2}$.
This reduced ω yield at the pole mass is spread out in mass which makes it more difficult to distinguish the signal from the background. Figure 2.21(a) shows the ω yield for different in-medium widths. The signal strength is significantly reduced with increased width.

Despite of using all these tools to increase the amount of in-medium decays, only 20% of the ω decays occur at higher densities $\rho > 0.1 \cdot \rho_0$. In figure 2.21(b) it is shown that roughly 80% of the ω decays occur in vacuum. Those who are decaying inside the nuclear medium are spread out over a wide range of densities. If there is a modification of the lineshape due to an increased density, the signal will be smeared out due to this broad density distribution.

(a)   (b)
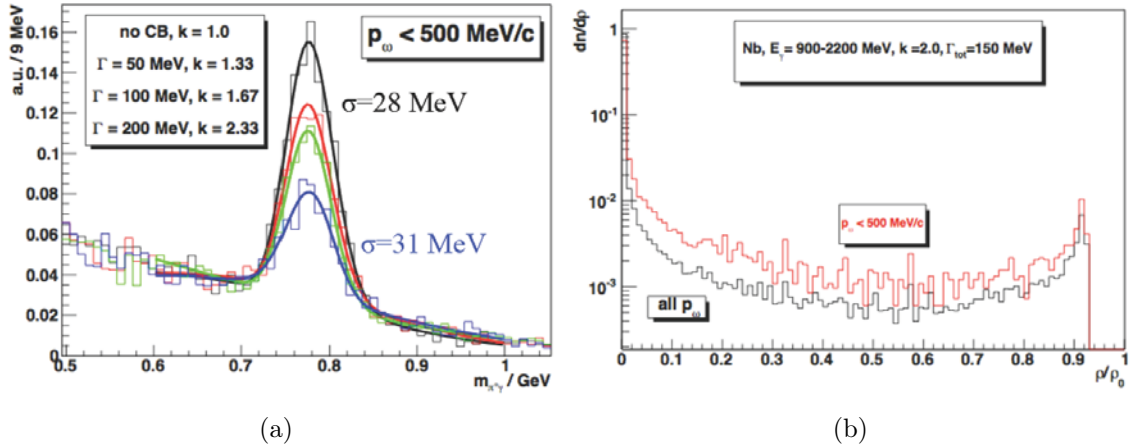
Figure 2.21: (a) $\pi^0\gamma$ invariant mass spectrum for different widths of the ω meson. The strength of the signal decreases with increasing in-medium width [Fri10]. (b) Profile of ω decays into $\pi^0\gamma$. Most of the decays occur outside the nuclear medium ($\rho = 0$) while the decays inside are spread out over the full density range. The amount of decays inside the nuclear matter can be enhanced by placing a cut on low ω momenta $\vec{p}_\omega < 500$ MeV (red curve) [Wei10].

This makes it really difficult to achieve in-medium information from the lineshape analysis and good statistics is necessary to distinguish between the different theoretical predictions.

2.7.3. The Decay Channel $\omega \to \pi^0\gamma$

The ideal decay channel to study in-medium modifcations of the ω meson is the decay into leptons $\omega \to l^+l^-$. Many of the experiments presented in this chapter used this decay mode for good reasons. Leptons do not underlie the strong force, therefore the decay products have no final state interactions. Thus, the measured 4-momenta of the leptons are undistorted and thus the invariant mass of the vector meson can be reconstructed without loss of important in-medium modifications. Looking for the dileptonic decay mode seems to be a clean and ideal method to study in-medium modifications. The question may arise: why looking at a different decay channel? The answer lies in the small branching ratios (BR) of vector mesons into dileptons. For the two lightest vector mesons ρ, ω the values are listed in table 2.1.
In addition to the small BR, the decay rates for the ρ and the ω meson are of the same order. The masses are very close, so it is difficult to seperate medium modifications of the ρ and ω meson in the e^+e^- invariant mass spectrum.

A different approach is the decay channel shown in figure 2.22.

Vector Meson	Mass	Decay Mode	BR
ρ	775.49 MeV	$\rho \to e^+ e^-$	$4.71 \cdot 10^{-5}$
		$\rho \to \pi^0 \gamma$	$6.0 \cdot 10^{-4}$
ω	782.65 MeV	$\omega \to e^+ e^-$	$7.16 \cdot 10^{-5}$
		$\omega \to \pi^0 \gamma$	8.92%

Table 2.1: Comparison of the dileptonic and hadronic decay modes for the ρ and ω meson.
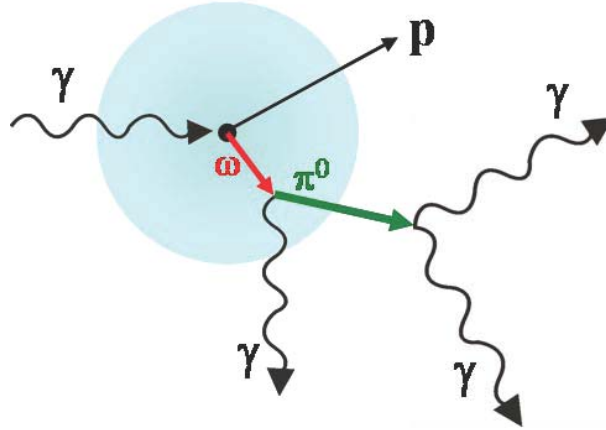
Figure 2.22: The ω meson produced in the nucleus decays into $\pi^0 \gamma$ with a further decay of the pion into two photons. The final state is $\omega \to \gamma\gamma\gamma$.

The ω meson is produced in the nuclear medium while a proton recoils and leaves the nucleus. The ω should decay inside the nucleus into $\pi^0 \gamma$ whereas the pion decays into two photons. The full decay channel can be written as

$$\omega \to \pi^0 \gamma \to \gamma\gamma\gamma \tag{2.24}$$

where the final decay products should carry the in-medium information of the ω meson. Looking again at table 2.1 the advantage compared to the dileptonic decay mode is obvious. The branching ratio is moderately high and the ρ decay into the same channel is suppressed by two orders of magnitude. In this sense, the invariant mass spectrum should be free of $\rho - \omega$ interference.

One clear disadvantage of the decay mode into $\pi^0 \gamma$ is the strongly interacting pion in the final state which can rescatter in the nuclear medium. Due to this final state interactions the 4-momentum of the π^0 can be changed which leads to a distorted ω invariant mass. These final state interactions have been investigated using BUU transport code calculations [Mes01]. Figure 2.23 shows the two-dimensional scatter

plot of the $\pi^0\gamma$ invariant mass versus the reconstructed kinetic energy of the pion T_{π^0}.
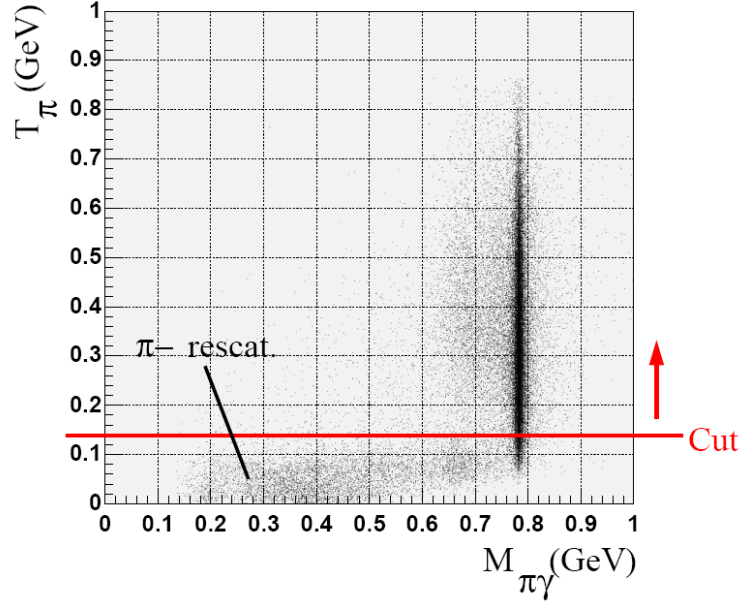
Figure 2.23: The kinetic energy of the pion as a function of the $\pi^0\gamma$ invariant mass. The spectrum is taken from [Mes01].

Pions which rescatter in the nuclear medium are moved to smaller masses. In the ω mass region the amount of distorted events due to FSI is small. With an additional cut on the kinetic energy $T_{\pi^0} > 150$ MeV these events can be suppressed further. Looking at the projection of figure 2.23 on the invariant mass axis, represented by figure 2.24, one sees the three contributions to this spectrum:

1. fraction of ω mesons decaying outside the nuclear medium

2. fraction of ω mesons decaying inside the nuclear medium, where the pion does not rescatter

3. fraction of ω mesons decaying inside the nuclear medium, where the pion does rescatter

In the left panel of figure 2.24 the contributions are shown for the full projection while in the right panel only those events are plotted where $T_{\pi^0} > 150$ MeV.

Under these conditions the contribution of distorted events is negligibly small and therefore an observed deviation in the ω lineshape would be a direct evidence for an in-medium modification.
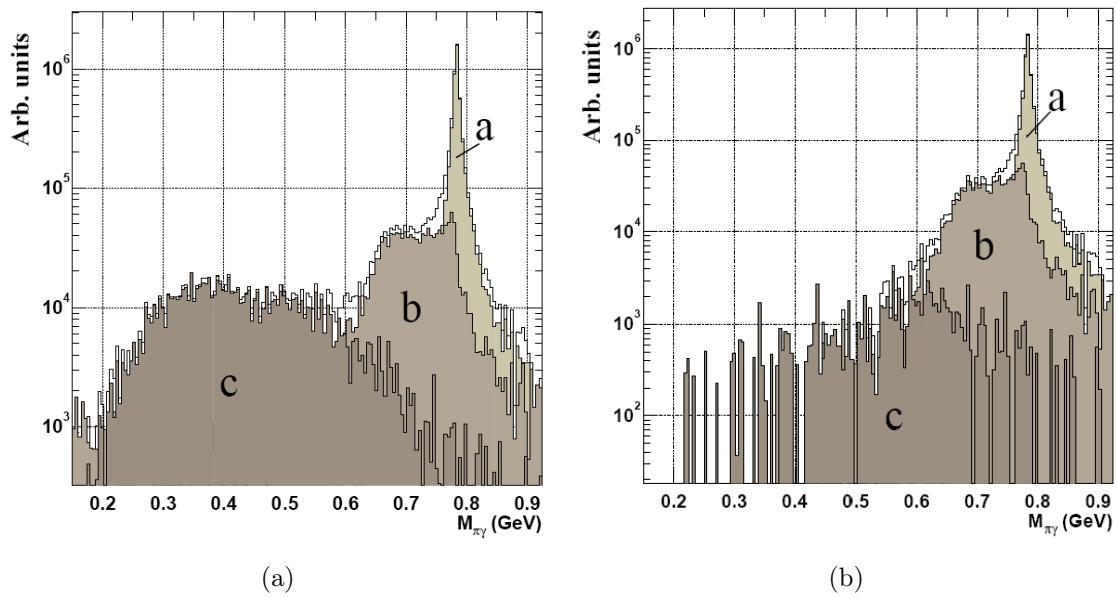
Figure 2.24: $\pi^0\gamma$ invariant mass spectrum without cut (left panel) and with cut $T_{\pi^0} > 150$ MeV (right panel). The plots are taken from [Mes01].

Chapter 3.

The Experimental Setup

The data presented in this thesis were obtained from experiments in the year 2008, which were performed at the tagged photon facility in the A2 hall of the Institut für Kernphysik, Johannes Gutenberg Universität, Mainz. The experimental setup consists of a tagging spectrometer and a detector system combining the Crystal Ball and TAPS calorimeters, which cover almost the full solid angle of 4π. Figure 3.1 shows both detector systems in their measuring position.

Figure 3.1: On the left side the Crystal Ball on its platform, on the right side the TAPS detector with its readout electronics is shown. TAPS is mounted on rails, so it can be moved easily close to the Crystal Ball for measurements.

In the next sections the accelerator and the experimental setup used during the beam-times in 2008 will be described in detail.

3.1. The MAMI Accelerator

The **MA**inz **MI**crotron MAMI is one of the worlds largest microtrons. The heart of the accelerator are the three racetrack microtron stages (RTM1 to RTM3) and since December 2006 the harmonic double sided microtron (HDSM). One of its advantages is the continuous wave mode, which provides a 100 μA continuous wave (cw) electron beam. Figure 3.2 shows the floor plan of the Institut für Kernphysik. The four microtron stages as well as the different experimental areas are shown.
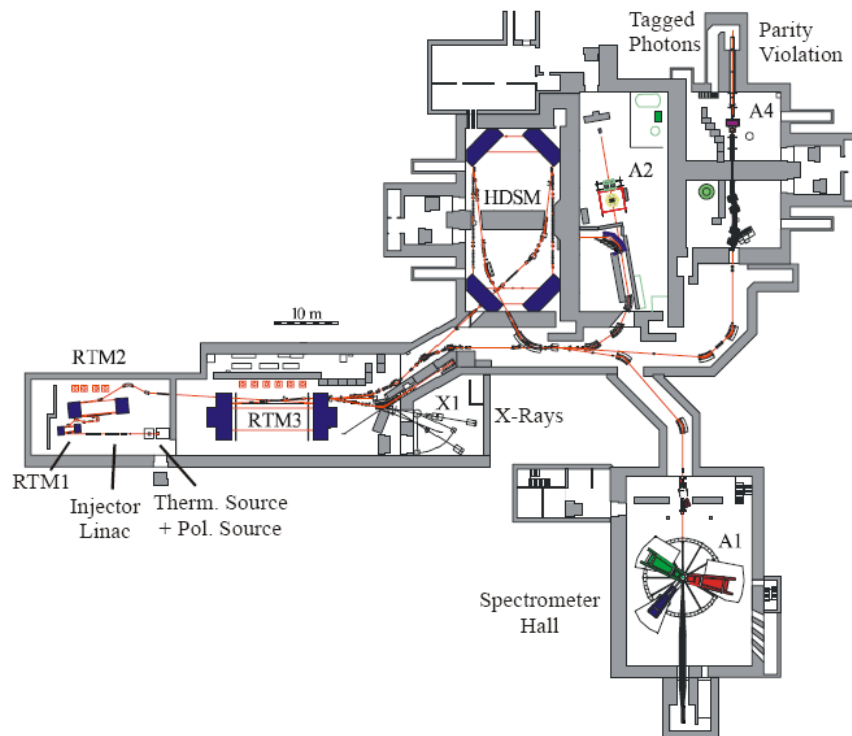
Figure 3.2: Floor plan of accelerator complex at the Institut für Kernphysik in Mainz. The different accelerator parts are shown, together with the experimental halls A1, A2, A4, and X1.

But before the electron beam can be injected in the microtron stages, one first has to produce free electrons and afterwards pre-accelerate them. Unpolarized electrons are produced using the electrongun EKAN, where a cathode is heated up to produce

the free electrons which are then accelerated up to 100 keV. The second electrongun PEKAN emits electrons which are polarized up to 75%. Electron emission is induced by a pulsed laser with a frequency of 2.45 GHz and a wavelength of 832 nm impinging on a crystal.

The free electrons (polarized or unpolarized) are accelerated further in a linear accelerator (short: linac). But not only the velocity has to be high enough, also the electrons have to have the right phase before they can be injected into the first racetrack microtron.

The major components of the accelerator are described in more detail in the next sections.

3.1.1. The Racetrack Microtrons

A racetrack microtron (RTM) consists of a linear accelerator stage and two dipole magnets which deflect the electrons by 180° redirecting them into the linac stage after each turn. Due to the homogeneous magnetic field of each dipole magnet the electron paths are half-circles whose radii increase by a discrete amount after each recirculation. Hence, for each trajectory one has to provide an individual beam pipe that allows the electrons to move in an extremely good vacuum.

The principle structure of a racetrack microtron is illustrated in figure 3.3.
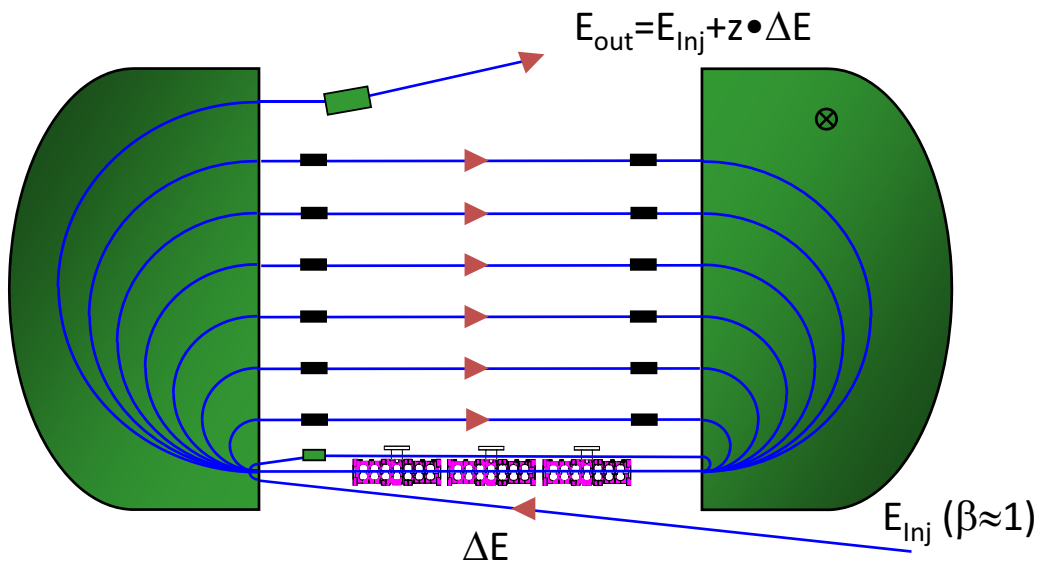
Figure 3.3: Principle of a racetrack microtron.

The electrons have to gain a specific amount of energy per turn, which can be calculated:

$$\Delta E = \frac{ec^2 B}{2\pi\nu_{HF}},\tag{3.1}$$

where e is the electric charge, c the speed of light, B the magnetic field and ν_{HF} the typical MAMI frequency of 2.45 GHz.

The electrons which are injected in the first racetrack microtron have an energy of 3.97 MeV. When the electrons pass the last turn of RTM1 they are injected in RTM2 and from there finally injected in RTM3. This three racetrack microtron cascade is called MAMI-B. The main parameters are listed in table 3.1.

	Linac	RTM1	RTM2	RTM3
Injection Energy [MeV]	0.1	3.97	14.86	180.0
Extraction Energy [MeV]	3.97	14.86	180.0	855.1
Number of cycles	-	18	51	90
Energy Gain per Cycle [MeV]	-	0.599	3.24	7.5
Dipole Field [T]	-	0.1026	0.555	1.2842
Weight per Magnet [t]	-	1.3	43	450

Table 3.1: Main parameters of the racetrack microtron cascade [Col09a].

3.1.2. The Harmonic Double Sided Microtron

To extend the physics program, the energy range of the MAMI accelerator was roughly doubled and increased to 1.6 GeV. In this energy range it is not practical to design a fourth stage of a racetrack microtron. The weight of the magnets is increasing proportional to E^3. A normal conducting dipole magnet that would bend electron trajectories by 180° at 1.5 GeV would require about 2000 tons of iron per magnet. It is far more convenient to use two dipole magnets which turn the beam by 90° each, thereby reducing the weight by a factor of eight. This last stage is called MAMI-C.

The setup of a so-called harmonic double sided microtron (HDSM) is illustrated in figure 3.4. One advantage of the HDSM is the second dispersion free line, which can be used for a second linear accelerator. Therefore the energy gain per turn can be calculated to:

$$\Delta E = ecB\frac{\lambda}{\pi - 2}.\tag{3.2}$$

Table 3.2 summarizes the main parameters of the fourth stage, which has been now operating since December 2006.

Figure 3.5 shows the upgraded accelerator. From the linac the electrons are injected
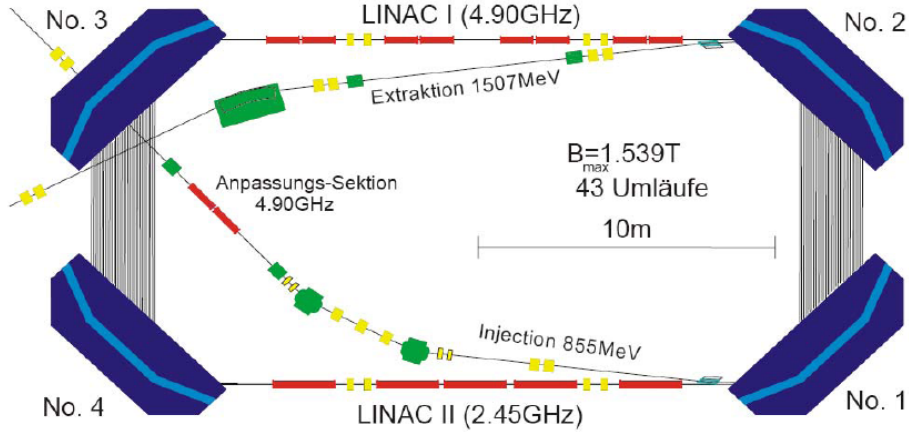
Figure 3.4: Principle of a harmonic double sided microtron.

	HDSM
Injection Energy [MeV]	855.1
Extraction Energy [MeV]	1508.0
Number of cycles	43
Energy Gain per Cycle [MeV]	13.9 - 16.64
Dipole Field [T]	0.95 - 1.53
Weight per Magnet [t]	250

Table 3.2: Main parameters of the harmonic double sided microtron [Col09a].

in the first racetrack microtron passing the other two RTM stages. Finally the electrons are injected in the HDSM where they are extracted with a maximum energy of 1508 MeV. By further investigations the accelerator group was able to increase the maximum energy. Up to now the energy limit is $E_{e^-} = 1604$ MeV ([Hei10]).

3.2. The Mainz-Glasgow Tagger

The Mainz-Glasgow Tagger consists of a momentum-dispersive electron spectrometer and a focal plane detector. It is used to convert the electron beam into a quasi monochromatic beam of real energy tagged photons. To provide a well-determined photon flux, the technique of Bremsstrahlung tagging is used. When the electrons with an incident energy E_0 hit a thin metallic foil, the so-called radiator (10 μm thick copper in our beamtime periods), Bremsstrahlung photons of an energy E_γ are generated. The scattered electrons are deflected in the magnetic field of the wide-range
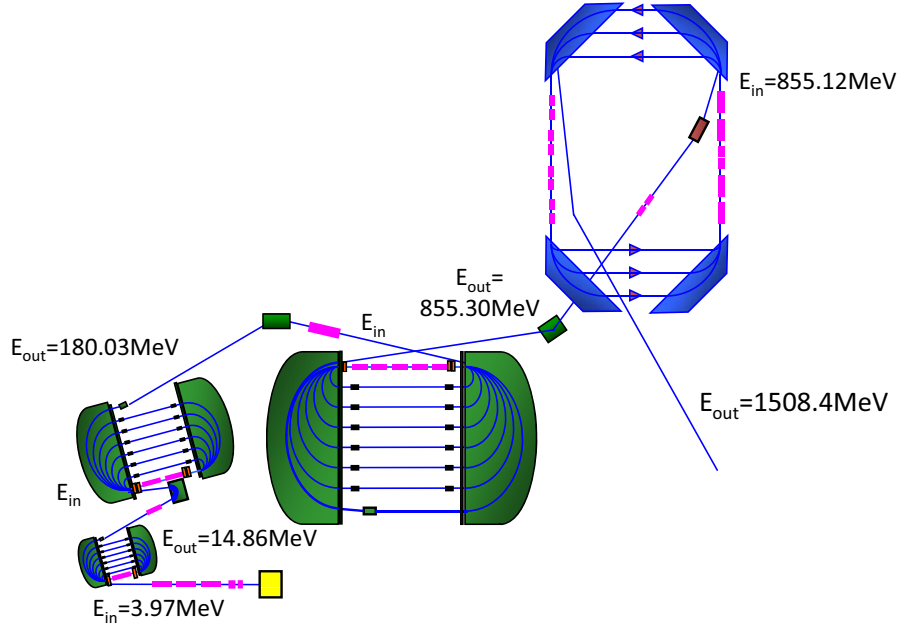
Figure 3.5: Complete accelerator including the linear accelerator, RTM1, RTM2, RTM3, and the HDSM.

momentum-dispersive electron spectrometer and focussed onto the focal plane. The electrons are deflected due to the Lorentz force on a circle with radius r

$$r = \frac{p}{e \cdot B} \tag{3.3}$$

where p is the momentum of the electron, e its charge and B the magnetic flux density of the tagging spectrometer. By measuring the point of impact on the focal plane the energy of the scattered electron E_{e^-} can be determined. Knowing the energies of the incoming and the scattered electron, the energy of the photon is given by

$$E_\gamma = E_0 - E_{e^-}. \tag{3.4}$$

The principle of the tagging spectrometer is shown in figure 3.6.

This technique has been used very successfully since the installation of the tagging spectrometer in the A2 hall in 1991. To cope with the new maximum MAMI energy, the spectrometer magnet had to be modified to provide a magnetic flux density of up to 1.9 Tesla which is necessary to guide the unscattered electrons onto the electron beam dump. The modifications were done by adding top, bottom and back yokes [McG08].

Since the performance of the existing tagging spectrometer is excellent, the idea was to keep the design of the focal plane including the spectrometer optics. The focal
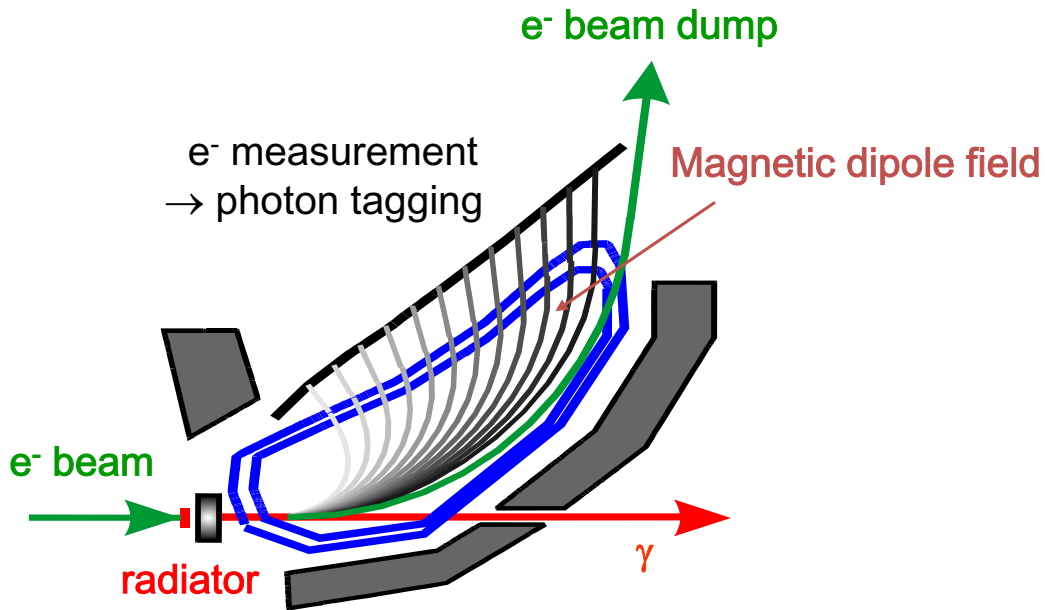
Figure 3.6: Schematic view of the tagging spectrometer.

plane detector still consists of 353 plastic scintillators, each overlapping half with its neighbours. They have a length of 80 mm, a thickness of 2 mm and widths between 9 and 32 mm. The scintillators cover an energy range of approximately 5% to 93% of the incident electron beam energy. The energy resolution for an electron beam energy of 1500 MeV is in the order of 4 MeV. Each plastic scintillator is read out with a Hamamatsu R1635 photomultiplier tube.

During the experiment it is possible to have more than one electron hit in the focal plane detector. To find the right corresponding electron-photon pair, the signal of the electron in the tagging spectrometer has to be in prompt coincidence with the trigger produced by the detector systems CB/TAPS.

3.3. The TAPS Detector System

In the 1980's the international TAPS collaboration with its members GSI (Darmstadt, Germany), GANIL (Caen, France), KVI (Groningen, The Netherlands), Universities of Gießen, Munich, Münster (Germany), and University of Valencia (Spain) was founded. The goal was to develop and design an electromagnetic calorimeter which allows to perform a very large variety of experiments. In addition the calorimeter should be usable in different setup configurations.

The name TAPS (**T**wo **A**rm **P**hoton **S**pectrometer) originates from its construction

time in 1990 [Nov91]. Since that time, TAPS has been utilized at several accelerator facilities all over Europe. Depending on the experimental demands, TAPS was set up either in the original two arm configuration or in different blocks around the target region, or as a forward wall as it is presently being used in Mainz and Bonn.

For the beamtime period 2004/2005 the readout electronics of TAPS was redesigned completely [Dre02]. With the new fast VME based readout boards it was possible to put the electronics as close to the detector as possible. Figure 3.7 shows the complete detector setup.

Figure 3.7: Photograph of the TAPS detector system. The readout electronics is mounted on the TAPS frame on both sides of the forward wall. The electronics for 4 blocks, together with the high voltage supplies are shown.

After the beamtime period 2004/2005 in Mainz TAPS was dismounted. The detector modules were transported to Gießen to perform a quality check of the crystals, the photomultiplier tubes, voltage dividers and the connection between them. For the following beamtime period some of the crystals together with crystals purchased by the university of Bonn were used to build a „Mini"-TAPS detector system consisting of 216 BaF$_2$ crystals. This left the Mainz TAPS setup with 384 instead of 510 detector modules.

The original frame of the TAPS detector in Mainz was re-used; the missing crystals were replaced with plastic modules of the same geometry, so-called dummy modules. The new TAPS wall is segmented into six blocks, every block comprises 64 crystals. Figure 3.8 shows a schematic view of the arrangement of the blocks.
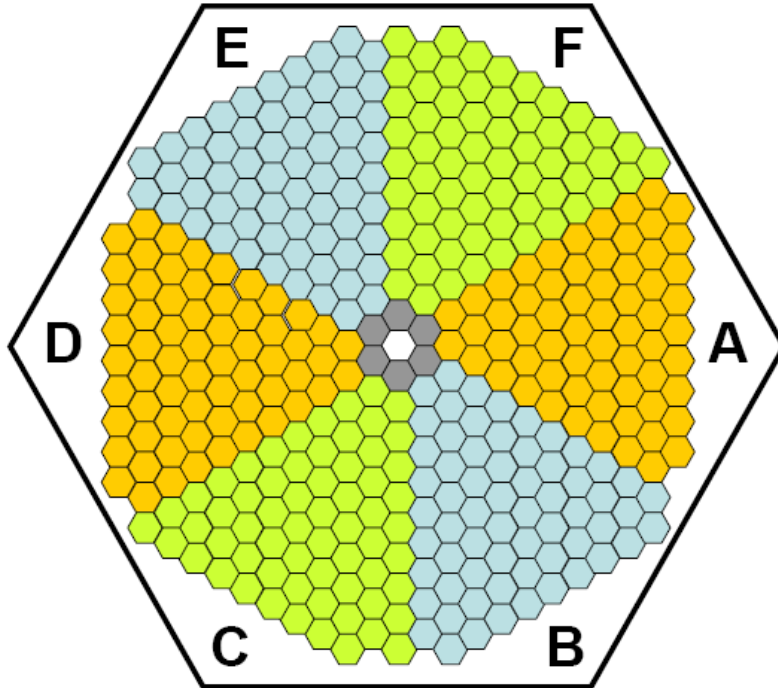
Figure 3.8: The TAPS forward wall configuration: 378 BaF_2 crystals, segmented into 6 block, labelled A to F (downstream view). In grey the 6 $PbWO_4$-modules of the inner ring are shown.

With the upgrade of the Mainz accelerator the maximum photon energy increased from 885 MeV to approximately 1600 MeV. At these higher energies electromagnetic background will be Lorentz boosted to much smaller polar angles leading to much higher count rates in the modules close to the primary photon beam. These increased rates together with the relatively long relaxation time of the scintillator material result in a saturation of the signal readout that limits the lifetime of the detector system. The possible options to mend this are a decrease in beam current or an increase of the CFD thresholds of the innermost detectors. Both options are not satisfying: the latter does not overcome the internal pile-up of scintillation light in the crystal and in addition discards low energy signals; the former option leads to an increase in beam time requirements to reach the desired precision.

To benefit from the high photon energies and a high current simultaneously, it was decided to exchange the crystals in the inner ring of TAPS. The deadtime of the

system is dominated by the decay time of $\tau = 620$ ns of the BaF_2's slow scintillation light component. A material with a faster decay time is lead tungstate ($PbWO_4$) with $\tau = 6$ ns which was chosen as a replacement for the BaF_2.

In March 2008 about one third of the TAPS detector was unmounted to allow for the installation of the $PbWO_4$ crystals. It was of importance to restore each module to its original position after the installation of the inner six lead tungstate modules to be able to keep the high voltage and threshold settings.

3.3.1. Barium Fluoride Crystals

Until Spring 2008 the TAPS calorimeter was completely made of barium fluoride crystals (BaF_2) only. The properties of this material are listed in table 3.3. With

Density ρ	4.89 g/cm^3
Radiation Length X_0	2.05 cm
Crystal Length	25 cm $\approx 12X_0$
Molière Radius R	4.3 cm
max emission: wavelength fast component decay time	195 nm, 220 nm 0.6 ns
max emission: wavelength slow component decay time	320 nm 620 ns
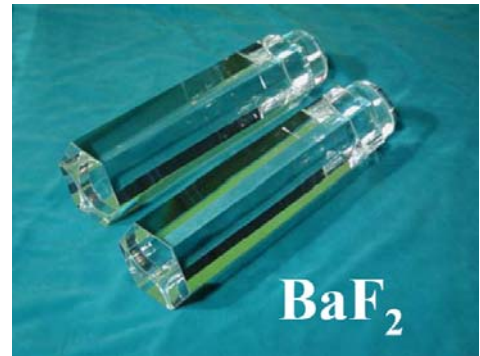
Table 3.3: Properties of BaF_2

Figure 3.9: BaF_2 crystals

BaF_2 a material was chosen which allows to grow large crystals. The crystals have a hexagonal shape with a front face diameter of 5.9 cm and a length of 22.5 cm. In addition there is a cylindric end cap with a diameter of 5.4 cm and a length of 2.5 cm. The overall length is 25 cm. Figure 3.9 shows a photograph of the crystals.

The BaF_2 crystals are wrapped in a thin layer of Teflon foil (Tetratex PTFE 1.5 mill) and aluminum foil. At the end cap the photomultipier tube (R2059-01) together with a voltage divider are coupled to the crystal. To get the complete setup light tight, everything is put in a black shrinking tube. Figure 3.10 illustrates the setup of one detector module.

The BaF_2 crystals used for TAPS can stop charged pions up to 185 MeV and protons up to 380 MeV kinetic energy [Mar98]. Due to the high light yield per MeV deposited energy TAPS provides a good energy resolution which was determined to

$$\frac{\sigma}{E} = \frac{0.79\%}{E_\gamma} + 1.8\% \quad \text{[Gab94].} \tag{3.5}$$
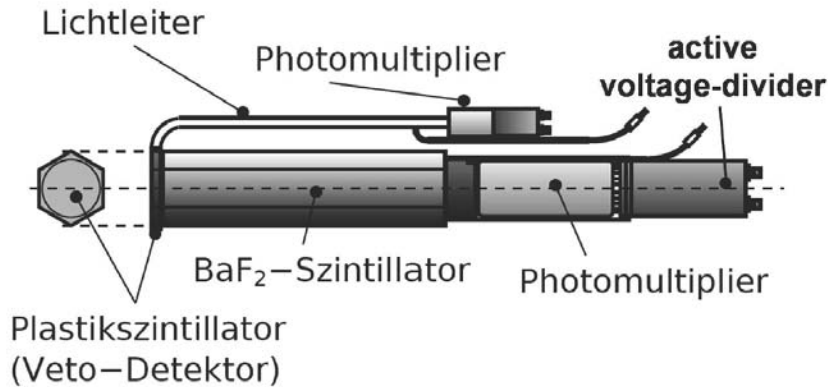
Figure 3.10: Schematic view of one BaF_2 module: crystal, photomultiplier tube, voltage divider and the plastic scintillator in front of the crystal.

3.3.2. Lead Tungstate Crystals

Lead tungstate ($PbWO_4$) is a material which becomes more and more interesting for modern calorimeters. The electromagnetic calorimeter of the CMS detector (CERN) comprises approximately 76000 crystals and also the electromagnetic calorimeter of the P̄ANDA detector, which is part of the FAIR facility at the GSI Darmstadt, will consist of about 16000 $PbWO_4$-crystals.

Lead tungstate is an achromatic scheelite-type crystal which is nearly transparent for visible light. The advantage of this material is the high density, which leads to a short radiation length and a small Molière radius. This allows building very compact calorimeters. In addition, $PbWO_4$ has a decay time of only 6 ns, so it is a very fast scintillator with hardly any slow component.

A disadvantage of lead tungstate crystals is the poor light yield per MeV at room temperature. Selected properties of $PbWO_4$ are listed in table 3.4.

Density ρ	8.28 g/cm^3
Radiation Length X_0	0.89 cm
Crystal Length	25 cm $\approx 12X_0$
Molière Radius R	2.0 cm
max emission: wavelength	420 nm
fast component decay time	6.0 ns

Table 3.4: Properties of $PbWO_4$ taken from [Col05].

3.3.3. The PbWO$_4$ Insert

The six innermost BaF$_2$ crystals are replaced by an array of lead tungstate crystals. Replacing the crystals one by one would not work because of the smaller Molière radius of the PbWO$_4$-crystals. Smaller crystals with a rectangular shape would produce undesired dead space between the lead tungstate crystals and the hexagonal BaF$_2$ crystals. Hence, not all the energy of a particle would be registered by the crystals and the reconstructed energy of the shower would be too small.

Taking this into account it was regarded the best solution to use trapezoidally shaped PbWO$_4$ crystals with dimensions chosen in such a way as to replace one BaF$_2$ module with four PbWO$_4$ modules, see figure 1.12(b). The dimensions are 34.4 mm and

(a) A single PbWO$_4$ crystal. (b) 4 PbWO$_4$ crystals forming a BaF$_2$ module. (c) Mechanical housing for the PMTs.
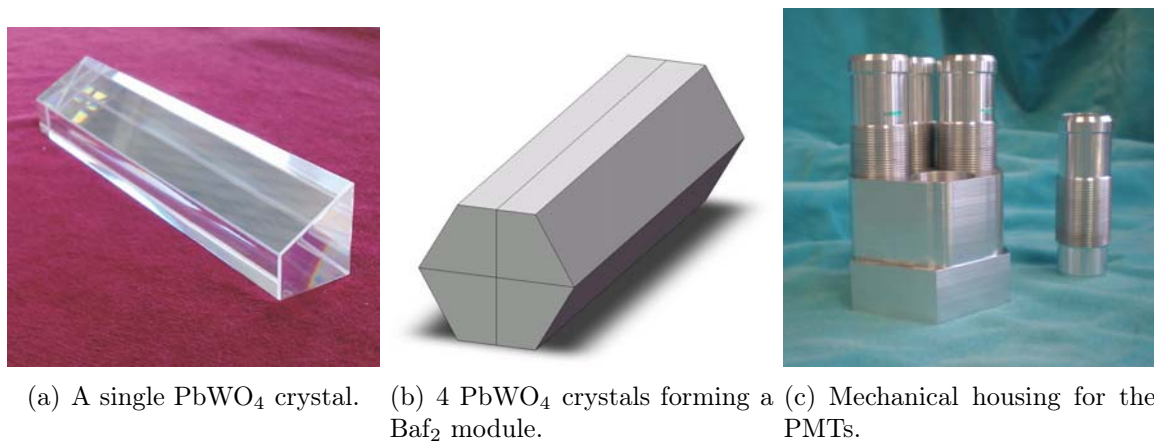
Figure 3.11

17.1 mm for the two parallel sides and 29.8 mm and 34.4 mm for the other two sides respectively. The length of the crystals is 200 mm. In figure 3.11(a) a single PbWO$_4$ crystal is shown.

To build a complete modul, each crystal was first wrapped in 70 μm thick reflectorfoil VME 2000 (from the company 3M) and then surrounded by an additional layer of 20 μm aluminum foil to guarantee that most of the light stays in the crystal. For the photomultiplier readout four PMTs per module have to be fixed and stabilized. Therefore, a mechanical housing made of aluminum was built by the mechanical workshop in Gießen. Figure 3.11(c) shows the main block together with the four cylindrical housings for the PMTs which are screwed into the main block.

The four PbWO$_4$ crystals were grouped together and the main housing block was fixed with a layer of black tape at one face of the crystals. In the last step shrinking tube was put around the four crystals, which covers also part of the mechanical housing for the PMTs.

Now the photomultiplier tubes (XP1911 from Photonis) together with the voltage dividers need to be prepared to couple them to the crystal. In total 24 detectors were

required. The PMTs were covered by a layer of capton foil, surrounded by a thin layer of μ-metal for magnetic shielding. Every PMT has a cylindric housing with an external thread, so that they can separately be inserted into the main housing (with thread inside) after this is fixed to the crystals. Figure 3.12(a) shows one complete module made of four $PbWO_4$ crystals. Further shown is one photomultiplier tube already assembled with the voltage divider and its housing which has to be screwed into the main block.

(a) A complete module consisting of 4 $PbWO_4$ crystals. In front a single PMT is shown and the main housing block for the PMTs for coupling to the crystals.

(b) 24 $PbWO_4$ crystals as the inner ring, mounted in the TAPS forward wall.

Figure 3.12

In figure 3.12(b) the 24 $PbWO_4$-crystals (labeled A1 to F4) forming now the inner ring of TAPS are shown. They are surrounded by the BaF_2-crystals.

3.3.4. The Veto Plastic Scintillators

The main function of the veto plastic scintillators is the identification of charged particles. The idea is to have the veto detectors in front of the crystals. Because of the versatility of the TAPS setup, the geometry of the charged particle detector system should allow for the same flexiblility. Hence, the decision was made to have individual veto plastic scintillators with the same hexagonal geometry which can be arranged in different configurations. For the present setup in Mainz 384 veto modules form a forward wall. The general concept is the read out of the plastic scintillators via green light emitting wavelength-shifting fibers (WLS-fibers) and multi-anode photomultipliers. The veto modules are made of 5 mm thick plastic ELJEN EJ 204 with a groove machined on one side for the WLS-fiber as illustrated in figure 3.13.

Multi-clad fibers BCF-92 (Bicron) with a diameter of 1 mm are chosen due to their extremely fast response and a time resolution of 2 ns FWHM. For details see [Jan99]. The radius of the groove is only 26 mm, which means the fibers have to be strongly bend. To avoid cracks in the WLS-fibers they are heated up to a temperature of T $\approx$ 85 °C, preshaped, tempered, and annealed. Figure 3.14 shows the wavelength-shifting fiber embedded in the groove of the veto module. The absorption wavelength of these fibers is $\approx$ 410 nm, the emission wavelength $\approx$ 492 nm. To handle the large number of read out channels, multi-anode photomultipliers H6568 from Hamamatsu with 16 channels are used. Figure 3.15 shows the final configuration of the veto detector.

The individual plastic scintillators are assembled in a hexagonal frame which is closed in the end by a lighttight black foil. The multi-anode PMTs are mounted on the outer side of the frame. The veto detector is mounted directly in front of the TAPS detector, which means each BaF$_2$ crystal has a veto plastic scintillator in front of it.
Figure 3.15 shows the setup of the Veto wall. In the frame the 384 plastic scintillators are arranged, in the middle the opening for the beam and on the outer sides the photomultiplier tubes are visible. After the detector is made light tight using a black plastic foil, the frame is put in front of the crystals.

Figure 3.13: Schematic drawing of a veto module with WLS-fiber (green) in the side view (top) and front view (bottom).
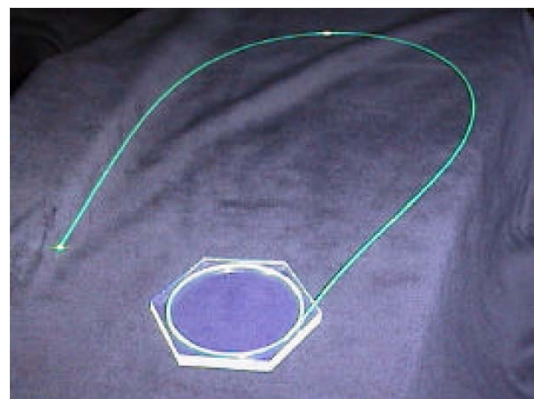
Figure 3.14: Picture of a plastic scintillator with the WLS-fiber embedded in the groove.
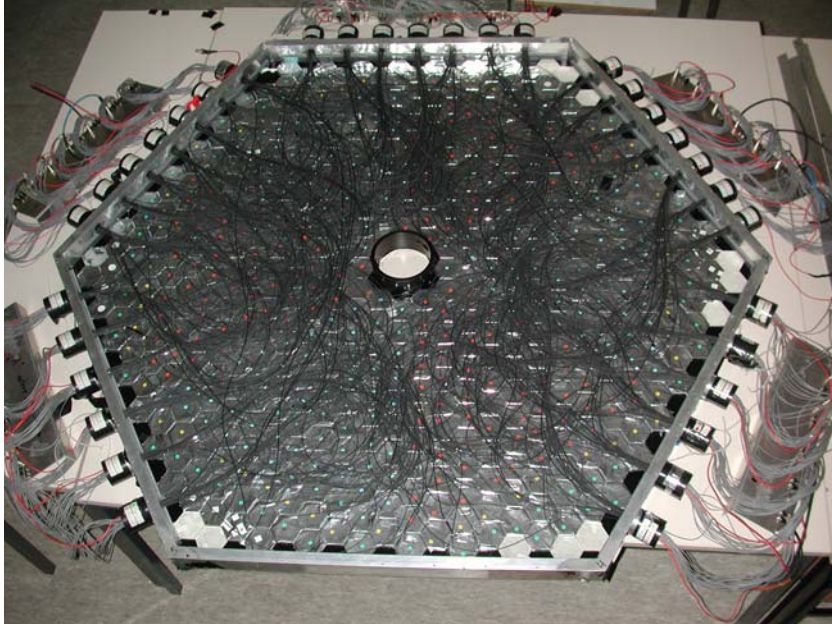
Figure 3.15: View inside the Veto detector.

3.3.5. The Readout Electronics

The TAPS detector system now comprises of three different components:

- BaF_2 crystals

- Veto plastic scintillators

- $PbWO_4$ crystals

Each sub-system has specific requirements and constraints to the readout electronics which need to be fulfilled as good as possible.

The BaF_2 Readout Electronics

The readout chain for the BaF_2 crystals was completely re-designed beginning 2000. The idea was to have the complete electronics part as close to the detector system as possible to avoid long cables and reduce cross-talk in the transmission lines. The readout system should also keep all the features the old electronics provided like energy, time and pulse-shape information in digitized form. Taking all these constraints into account a compact and fast VME[1] based readout board was developed [Dre00], [Dre04].

---

[1]**V**ersa **M**odule **E**urocard

One board can process the information of four BaF_2 channels, where energy, time, and pulse-shape informations are digitized by a 12 bit ADC (**A**nalog to **D**igital **C**onverter). To start the QAC (**C**harge to **A**mplitude **C**onverter) for the charge integration and the TAC (**T**ime to **A**mplitude **C**onverter) for the time measurement the detector response has to be larger than the CFD (**C**onstant **F**raction **D**iscriminator) threshold. Figure 3.16 shows the principle structure of the energy and the time branch.
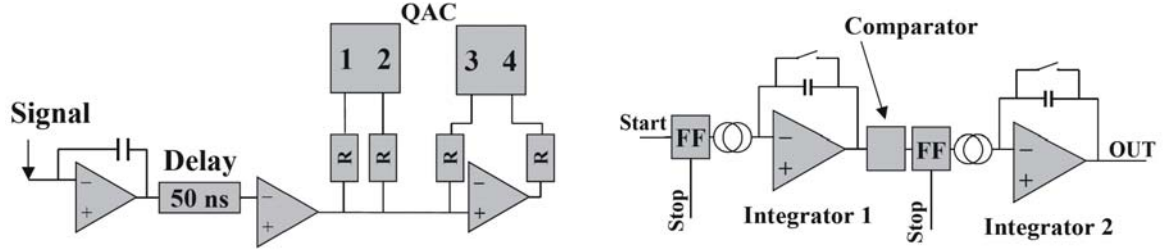
(a) Schematic block diagram of the energy branch.

(b) Schematic block diagram of the time branch.

Figure 3.16: Schematic block diagrams of the BaF_2 readout electronics taken from [Dre02].

For the pulse-shape information, which can be used to distinguish between photons and protons, it is necessary to have two different charge integration gates: one over the full time response (2 μs) and one over the fast component (40 ns). Both charge integration gates are foreseen with low and high gain.
For the time information a dynamic range of 400 ns in the TAC was used which leads to a time resolution of 100 ps/channel.
Per channel there are in total three discriminators, one CFD and two LEDs (**L**eading **E**dge **D**iscriminator). They can be used for trigger selection, e.g. as low and high threshold.
The readout electronic is running in common stop mode: every crystal is starting individually while the trigger delivers the common stop signal for all the crystals. Thus, the CFD and the two LEDs signals are freely running, the total count rate is limited due to the dead time to roughly 400 kHz.

The Veto Readout Electronics

The readout electronics of the BaF_2 crystals was adapted for the readout electronics of the Veto plastic scintillators. The same board could be used with only slight modifications. The CFD is not used for the Veto readout and there is only one LED per channel. Instead of the four charge integration gates per BaF_2 channel here one integration gate of 110 ns is sufficient. For the time information the same TAC design

is used. With these modifications it was possible to have 8 channels on one board. The big advantage of the new Veto readout electronics is that the energy and time information of the plastic scintillator response is available.

The PbWO$_4$ Readout Electronics

The inner ring was replaced with PbWO$_4$ crystals to increase the count rate capabilities. With the readout electronics optimized for a BaF$_2$ signal with 2 μs shaping time one cannot make use of the faster response of the PbWO$_4$ crystals. Hence, an additional electronic branch for the readout of the inner ring was necessary. To this end parts of the old TAPS electronics could be used together with new components (QDC, multi-hit TDC). Figure 3.17 shows the schematic drawing of the inner ring PbWO$_4$ readout electronics.

In contrast to the BaF$_2$ readout, here a common start mode is used. The trigger signal starts a common gate for all crystals. Therefore the analog energy signals have to be delayed.
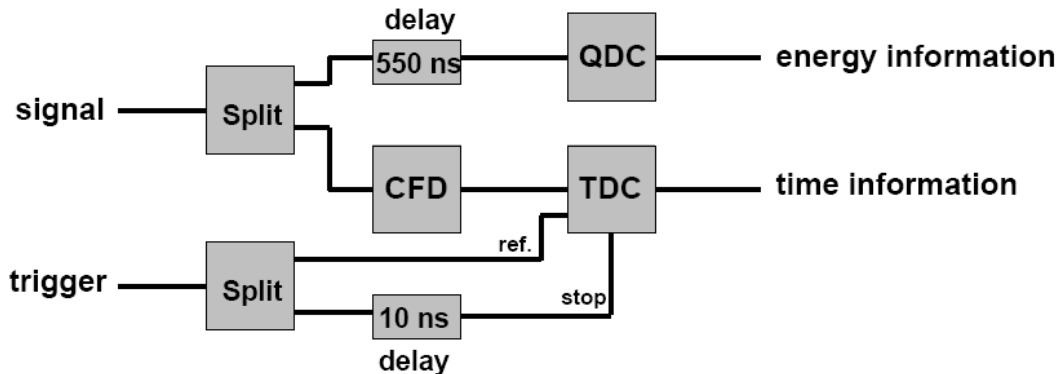
Figure 3.17: Schematic drawing of the readout electronics for one PbWO$_4$ channel.

Like for the BaF$_2$ signal energy and time information is read out and digitized. Thus an active splitter box is used for splitting up the incoming signal into one energy and time branch. For the energy information the signal is delayed by 550 ns before it is digitized in the QDC. The used module is a 16 channel dual range QDC (V965, CAEN nuclear physics). In the time branch the signal has to be larger than the threshold set in the CFD, where the module FCC8 from GAN ELEC is used. Afterwards the signal is digitized in the multi-hit TDC module (**T**ime to **D**igital **C**onverter, V1190 CAEN nuclear physics). The trigger signal is split up, too. One branch is used as a

time reference signal and has to be subtracted from the output of the TDC. The other branch is delayed by 10 ns and stores the events in the multi-hit TDC.

3.4. The Crystal Ball Detector

The Crystal Ball detector (CB) was originally designed for meson spectroscopy at e^+/e^- collider facilities. It was running at SPEAR (SLAC) performing Ψ, Ψ' spectroscopy or at DORIS (DESY) for e.g. Υ spectroscopy [Nef95]. In November 2002 the CB was transported to Mainz and installed in the hall of the A2 collaboration. Since 2004 it has been running together with the TAPS detector.
The Crystal Ball detector comprises 672 NaI(Tl) crystals shaped as truncated triangular pyramids with an edge length of 5.1 cm close to the target region and 12.7 cm at the outside. The crystals are 40.6 cm long which corresponds to 15.7 radiation lengths. They form a ball-like structure: a icosahedron.
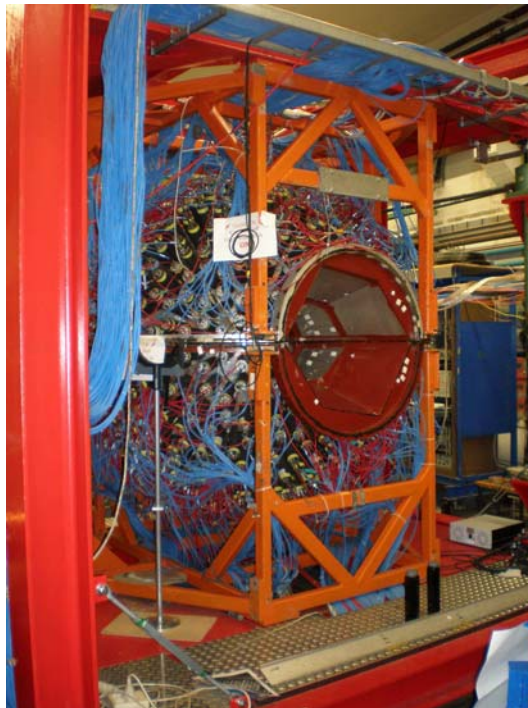
Figure 3.18: Photograph of the Crystal Ball detector.

Figure 3.19 shows a projection of the CB to a plane. There are 20 major triangles (one of them drawn red), each divided in four minor triangles (in green) consisting of 9 single crystals (in blue). In total 11 different crystal geometries were needed to

construct the icosahedron shape. Also visible are the entrance and exit holes (size of 24 crystals each), which were originally needed for the beam pipes of the collider experiments. This maybe a disadvantage at first sight but at least in forward direction not really a problem. In a fixed target experiment (like in Mainz) the produced particles are mostly boosted in forward directions. The insensitive area of the CB in forward direction is covered by a detector system (TAPS) downstream of the Crystal Ball. For practical reasons the CB is assembled in two hemispheres. Each of them is capsuled hermetically to protect the hygroscopic sodium iodide crystals from humidity. The inside is kept at vacuum to increase the mechanical stability of the detector. The inner walls are made of thin steel to get as low energy losses of the reaction products as possible. The top hemisphere can be lifted separately to get access to the equipment located inside of the Crystal Ball. In the closed position there is still a gap of $d \approx 5$ mm. In spite of the entrance and exit holes and the inactive area at the equatorial plane the CB covers roughly 94 % of the solid angle, together with TAPS the complete system reaches ≈ 98 %.

Polar Acceptance	$20° \le \theta \le 160°$
Azimuthal Acceptance	$1.2° \le \phi \le 178.8°$ and $181.2° \le \phi \le 358.8°$
Energy Resolution [$\sigma/$E]	$\frac{2.7\%}{\sqrt[4]{E(GeV)}}$
Time Resolution FWHM	≈ 2.5 ns
Minimum Ionizing Energy	197 MeV
Stopping Range of Protons	425 MeV

Table 3.5: Properties of the Crystal Ball.

Figure 3.18 shows the Crystal Ball detector while in table 3.5 its main properties are summarized.

The individual NaI crystals are first wrapped in 150 μm thick reflecting paper and in 50 μm thick aluminum foil for optical insulation. This should reduce the insensitive material and energy loss between the crystals. In table 3.6 the main properties of the NaI crystals are listed. NaI crystals of this size can stop protons up to a kinetic energy of 425 MeV while roughly 98% of the energy of an electromagnetic shower is deposited in a cluster of 13 crystals.
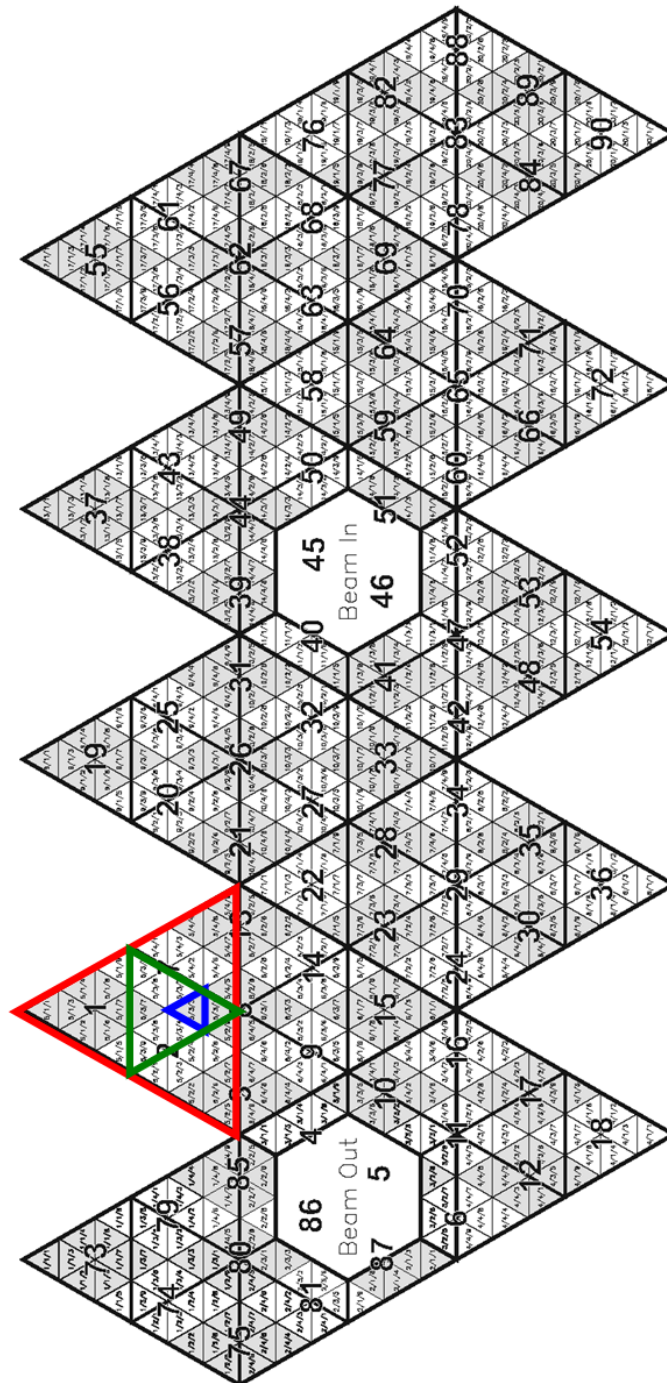
Figure 3.19: Segmentation of the Crystal Ball.

Density ϱ	$3.67 \frac{\text{g}}{\text{cm}^3}$
Maximal λ of emitted light	410 nm
Decay time	230 ns
Light yield	40000 photons / MeV
Radiation length X_0	2.59 cm
Crystal length l	40.6 cm $\widehat{=}$ 15.7 X_0
Molière radius R_m	4.3 cm

Table 3.6: Properties of NaI.

3.5. The Particle Identification Detector

To study different decay channels it is always important to identify all the detected particles. Therefore first of all a discrimination of charged and neutral particles is necessary. While the method of time-of-flight (ToF) can be used for TAPS because of the sufficiently long distance between the target and the detector, the distance in case of the Crystal Ball detector is too small to exploit the time-of-flight information. Thus, a Particle Identification Detector (PID) was built (see [Dow06]) to identify charged particles and to discriminate between protons, charged pions and electrons.

Because of the limited space inside the Crystal Ball the PID detector is located between the target area and the Multi Wire Proportional Chamber (MWPC).

The Particle Identifiction Detector consists of 24 plastic scintillators. Each scintillator strip has a length of 310 mm, a height of 13 mm and a thickness of 2 mm, all together the strips are forming a barrel of 100 mm diameter. For optical insulation, each strip is wrapped in Mylar foil. They are aligned along the beam axis where each plastic scintillator covers 15° in ϕ. Figure 3.20 shows a picture of the PID detector.

For an identification of the different charged particles the energy deposition in the NaI crystals is compared to the energy deposited in the PID scintillators.

Figure 3.20: Photograph of the PID ([Dow06]).

3.6. Targets

To investigate possible modifications of the meson properties caused by in-medium effects, two different solid targets were used for the three ω-photoproduction beamtimes in 2008. They had to be placed directly in the center of the Crystal Ball detector. Therefore an additional aluminum beam pipe part was manufactured, which was used instead of the target cell for e.g. liquid hydrogen. To place the solid target at the right position a special target holder was constructed which is shown in figure 3.21. The thickness of the individual targets is roughly $0.1 \cdot X_0$ (see tables 3.7/3.8). The thicker Carbon target is fixed by the compression of the 2 screws while the thinner Niobium target fits into the slits of the screws. Since the center position of the Crystal Ball is known, the mechanical workshop produced a tool which directly moved the target holder to the right center position.
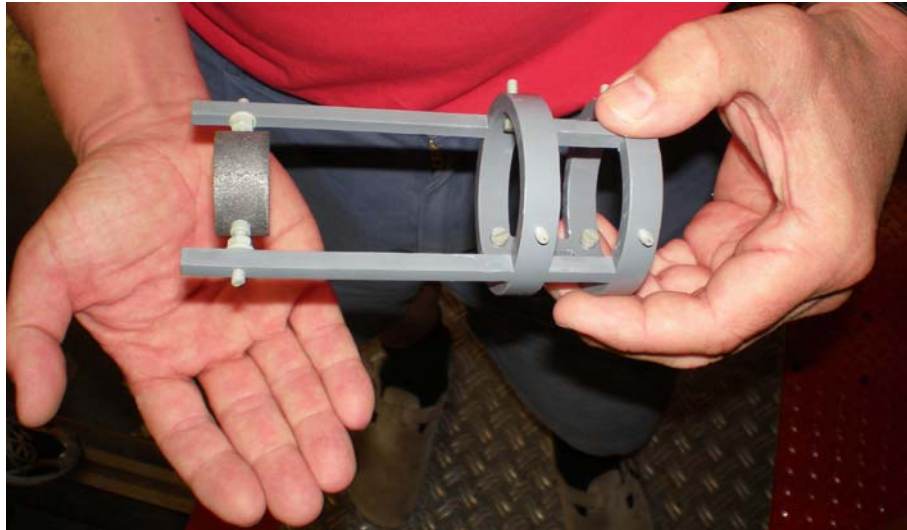
Figure 3.21: Target holder with the Carbon target fixed between the screws. This is put in the center of the Crystal Ball.

3.6.1. Niobium

The niobium target was used in the April/May and the August beamtimes. The properties like mass, length, and diameter were measured before and after the beamtimes. In table 3.7 the averaged values are listed together with the main characteristics of ^{93}Nb.

Niobium Target	
Atomic Number Z	41
Mass Number A	93
Radiation Length X_0	11.58 mm
Mass m	6.11 g
Thickness l	1.0 mm
Diameter d	30.0 mm
Densitiy ϱ	8.64 $\frac{g}{cm^3}$

Table 3.7: Properties of the ^{93}Nb target.

In addition, the number of target nuclei per cm^2 plays a role. This number is decreasing with higher mass number A and in this case the beam current can be increased.

$$N_{\text{target}} = \varrho \cdot x \cdot \frac{N_A}{A} \tag{3.6}$$

$$= 8.64 \frac{g}{cm^3} \cdot 0.1 cm \cdot \frac{6.022 mol^{-1}}{93 \frac{g}{mol}} \tag{3.7}$$

$$= 5.59 \cdot 10^{21} cm^{-2} \tag{3.8}$$

3.6.2. Carbon

For the June beamtime the carbon targed was used. The properties were also measured before and after the beamtime and are shown in table 3.8.

Carbon Target	
Atomic Number Z	6
Mass Number A	12
Radiation length X_0	193.2 mm
Mass m	17.70 g
Thickness l	15.0 mm
Diameter d	15.0 mm
Densitiy ϱ	1.669 $\frac{g}{cm^3}$

Table 3.8: Properties of the ^{12}C target.

Calculating as well the number of target nuclei per cm^2 for the ^{12}C target gives the

following number which is of course larger compared to the number for Niobium.

$$N_{\text{target}} = \varrho \cdot x \cdot \frac{N_A}{A} \tag{3.9}$$

$$= 1.669 \frac{\text{g}}{\text{cm}^3} \cdot 1.5\text{cm} \cdot \frac{6.022\text{mol}^{-1}}{12\frac{\text{g}}{\text{mol}}} \tag{3.10}$$

$$= 1.236 \cdot 10^{23}\text{cm}^{-2} \tag{3.11}$$

3.7. Beamtime Overview

The aim is to study the photoproduction of ω-mesons close to the production threshold $E_{\gamma,thresh} = 1108$ MeV. Therefore the maximum available electron beam energy of 1508 MeV[2] was choosen with the corresponding maximum tagged photon energy of 1400 MeV. In all the ω-production beamtimes a 10 μm thin copper foil was used as radiator to produce the Bremsstrahlungsphotons together with a 4 mm Tungsten collimator. The parameters are summarized in table 3.9.

Beam Energy E_{e-}	Tagged Photon Energy E_γ	Radiator	Collimator
1508 MeV	1400 MeV	10 μm Copper	4 mm Tungsten

Table 3.9: Common parameters of the three beamtimes for ω-photoproduction in 2008.

The channel of interest is the decay $\omega \to \pi^0\gamma \to \gamma\gamma\gamma$. To focus on these events the trigger conditions were set accordingly. To fulfill the trigger condition a multiplicity of either at least 2 or at least 3 is required. That implies two or three crystals in the CB/TAPS detector had a signal above the LED/CFD threshold. Because of the large number of events with a multiplicity of 2 they were downscaled by a factor 2. In addition to the multiplicity trigger condition the total energy deposition in the Crystal Ball had to be larger than 300 MeV.

The selected trigger conditions worked fine and were used in all three beamtimes. They are listed in table 3.10 together with the used currents for the different targets and the periods of data taking.

In the April/May beamtime we started with a beam current of 6 nA. But first extrapolations showed that the number of produced ω-events would be too low. Thus the current was increased to 12 nA and kept also for the August beamtime. With the carbon target we started with 8 nA but the deadtime of the system was too high, accordingly the current was reduced to 6 nA. For this analysis the complete data with

---

[2]Up to now the maximum beam energy is 1604 MeV

Date	Target	Hours	Current	Trigger
22.04. - 28.04.2008	^{93}Nb	80 h	6 nA	M2/2, M3, $\sum$ E > 300MeV
29.04. - 13.05.2008	^{93}Nb	370 h	12 nA	M2/2, M3, $\sum$ E > 300MeV
18.06. - 19.06.2008	^{12}C	15 h	8 nA	M2/2, M3, $\sum$ E > 300MeV
19.06. - 30.06.2008	^{12}C	210 h	6 nA	M2/2, M3, $\sum$ E > 300MeV
05.08. - 21.08.2008	^{93}Nb	330 h	12 nA	M2/2, M3, $\sum$ E > 300MeV

Table 3.10: Parameters for the different beamtimes looking for ω-photoproduction in 2008.

all current settings were used.

Unfortunately, 82 hours of data of the August beamtime are not accessible due to a failure of the A2 storage system in Mainz.

Chapter 4.

Calibration

During data taking, all information about energy deposition in the detector components, timing, etc. is digitized and stored on hard disk. The calibration provides means to convert the digital information, i.e. QDC and TDC channel numbers, back to energy and time information.

In the following sections the calibration procedures for the different detector systems as well as the results for the Carbon beamtime will be presented.

4.1. Crystal Ball

4.1.1. NaI Energy Calibration

Every time a photon hits the detector material it will generate an electromagnetic shower which deposits a certain amount of energy in the crystal. One makes use of the fact that a part of the deposited energy produces scintillation light with an intensity proportional to the amount of deposited energy. The light generated in the crystal has to be converted into an electronic signal. This can be realized using a photomultiplier tube (PMT) which is coupled to the end face of the crystal. In the PMT the photons initiate an electron cascade where the amount of produced electrons is proportional to the energy deposition in the crystal. This information is stored in the corresponding QDC channel. The correlation between QDC channel number and deposited energy is linear and in the easiest form it is given by

$$E = \text{gain} \cdot (\text{channel} + \text{offset}) \,. \tag{4.1}$$

If QDC channel number zero corresponded to the zero energy value the offset parameter could be neglected. Since this is usually not the case, one has to determine the offset value from the pedestal position which corresponds to the zero energy. To obtain the gain factor another point is needed. Therefore the invariant mass of the π^0-meson is used.

One problem is that the energy calibration has to be done for each crystal separately but the invariant mass of the π^0 will be measured via the decay $\pi^0 \rightarrow \gamma\gamma$. From the decay products the pion can be reconstructed via

$$\mathrm{m} = \sqrt{2 \cdot \mathrm{E}_1 \cdot \mathrm{E}_2 \cdot (1 - \cos\alpha)} \tag{4.2}$$

where E_1 and E_2 are the energies of the photons, and α is the opening angle between them in the lab system.

The ideal scenario would be two hits in the detector array, so that the complete energy information of every photon would be stored in just one crystal. But due to the creation of an electromagnetic shower the energy will be distributed over a large number of crystals, a so called cluster.

However, selecting now for events with two neutral hits in the Crystal Ball, the energy of the central cluster crystal is plotted versus the corresponding detector number in a two-dimensional histogram. A macro written by Dominik Werthmüller and Igal Jaeglé determines the position of the pion peak for each crystal via a fitting routine. With these values the new gain can be calculated:

$$\mathrm{newgain} = \mathrm{oldgain} \cdot \frac{m_{\pi^0}^{PDG}}{m_{\pi^0}^{meas}}. \tag{4.3}$$

This calibration procedure is an iterative process. Starting with old gain factors from
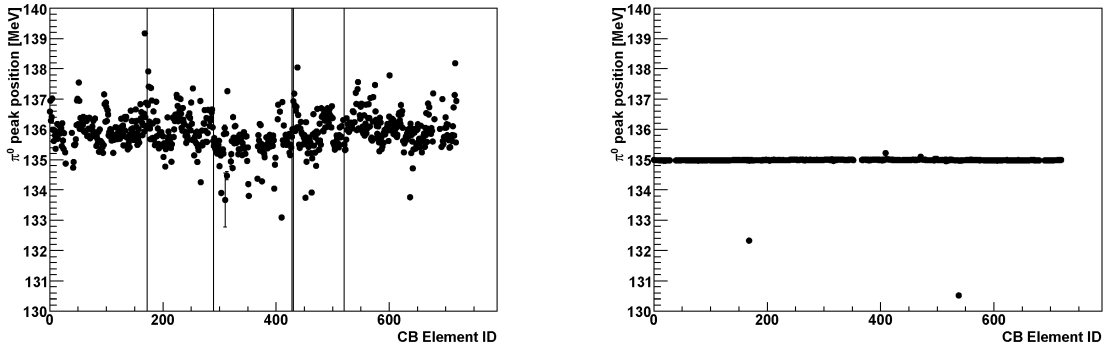
(a) Position of the pion peak in the CB before the calibration.

(b) Position of the pion peak in the CB after the calibration (already after the second order calibration).

Figure 4.1: Calibration of the calorimeter using the π^0 mass as fix point (Carbon beamtime).

previous beamtimes, the position of the π^0-mass scatters around 136 MeV which is close to the value listed in the PDG (**P**article **D**ata **G**roup), see figure 4.1(a). After some iteration steps a sharp line around the pion mass is visible (see figure 4.1(b)).

Hence, the pion peak being at the correct position, the same should hold for the η-meson because of the linear channel-energy-correlation assumed. Unfortunately, the η-mass is off by roughly 10 MeV. The goal is now to shift the η-mass without changing the aligned π^0-mass. Boris Lemmer investigated a new second order calibration method, for details see [Lem09]. The result for the Carbon beamtime can be seen in figure 4.2(b). The mass of the π^0 was not affected. Figure 4.1 shows the position of the π^0 peak already after the second order calibration.
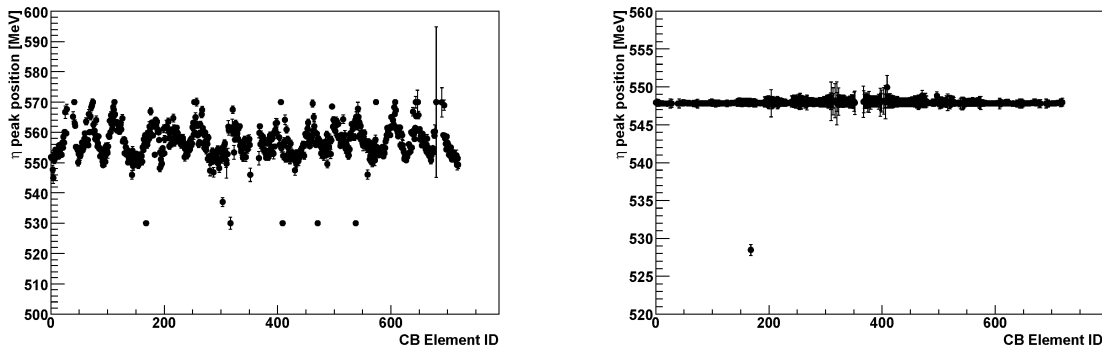
(a) Position of the η peak in the CB before the calibration.

(b) Position of the η peak in the CB after the calibration.

Figure 4.2: Calibration of the calorimeter using the η mass as fix point (Carbon beamtime).

4.1.2. NaI Time Calibration

The goal of the time calibration is to have all the prompt peak positions of the 672 NaI detectors at the same position in the TDC spectrum. Similar to the energy calibration there are two parameters: gain and offset. The gain is set by the time range used in the TDC module and hence cannot be modified. Only the offset parameter can be chosen at will in a way that all prompt peaks arrive at the same position of the TDC spectrum. It is determined by looking for events where only two photons hit the CB, i.e. two clusters were detected. The time difference of the two clusters is then shifted accordingly. Similar to the energy calibration only the time information of the central crystal is used. The peak is fitted with a Gaussian distribution and from the position information a new offset value can be calculated. This is again an iterative procedure until all peaks are at zero. But shifting the peaks to zero timing is not enough. The timing of the Crystal Ball is determined by leading edge discriminators (LED). For the experiment a certain energy threshold is set in the LEDs. Whenever a particle generates a signal higher than the threshold the TDCs get a common stop signal. The
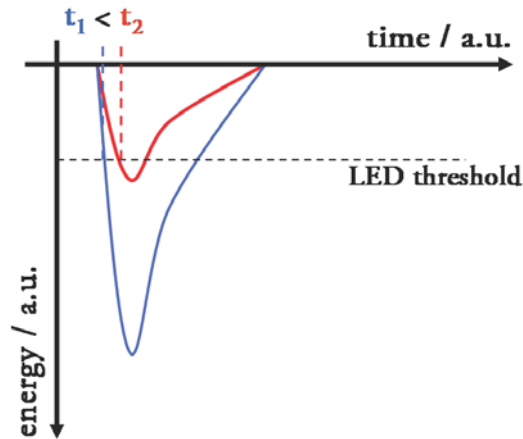
Figure 4.3: The red signal with a low amplitude (corresponding to a small amount of energy deposited in the detector) has a longer rise time than the blue signal with large amplitude. The LED threshold, shown as a dashed line, is crossed earlier by the blue signal although both events occured at the same time.

timing of the stop signal depends on the signal amplitude because the rise time of large signals is shorter than that of small signals. This effect is known as time-walk. Since signals of large amplitude correspond to large energy deposition in the detector, this effect is said to be energy dependent. In figure 4.3 you can see how the time for lower energies (red) increases passing the energy threshold at a later time.
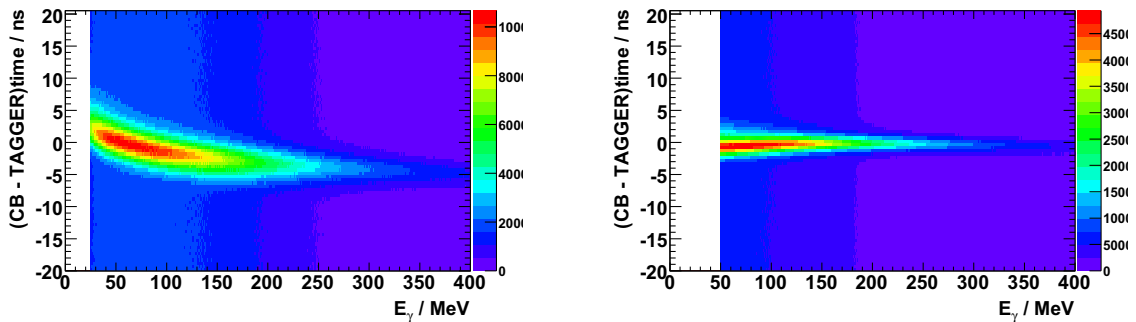
(a) Timing before walk correction in the CB.

(b) Timing after walk correction in the CB.

Figure 4.4: Timewalk correction for the Carbon beamtime.

In the data this shift in time is visible in the energy versus time plot (figure 4.4(a)). For lower energies the time of the photons increases. This effect has to be corrected

for. In figure 4.4(b) the walk-corrected data is shown. Now the time information is independent of the energy which corresponds to the straight line.

After the complete time calibration of the Crystal Ball including the calculation of the correct offset parameter for each channel and the timewalk correction one achieves a time resolution of 3.16 ns FWHM (**F**ull **W**idth **H**alf **M**aximum) looking at the time difference (figure 4.5(a)). The CB timing against the tagger has a time resolution of 2.17 ns FWHM presented in figure 5.9(b).
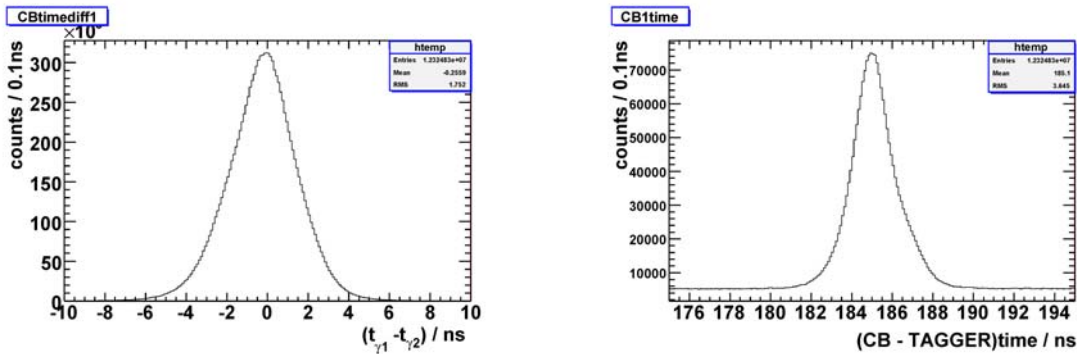
(a) Time difference from two hits in the CB detector.

(b) Time of a photon in CB against the tagger time.

Figure 4.5: Results of the time calibration for the Carbon beamtime.

4.2. TAPS

4.2.1. BaF$_2$ Energy Calibration

The energy calibration of the TAPS BaF$_2$ crystals is a two step process. Before a beamtime starts, the crystals are calibrated with cosmic muons. To be sure, that the calibration is stable, it's better to have additional cosmic runs during the experiment and afterwards.
Minimum ionizing particles like cosmic muons deposite a specific amount of energy per path length when they travel through a crystal. The energy deposition for a hexagonal BaF$_2$ crystal of 6 cm height is 37.7 MeV [Roe91]. The calibration has to be done for every individual crystal. From the measurement of cosmic muons one gets two peaks in the QDC spectrum as shown in figure 4.6: the pedestal and the minimum ionizing peak. The pedestal corresponds to an energy value of zero, while
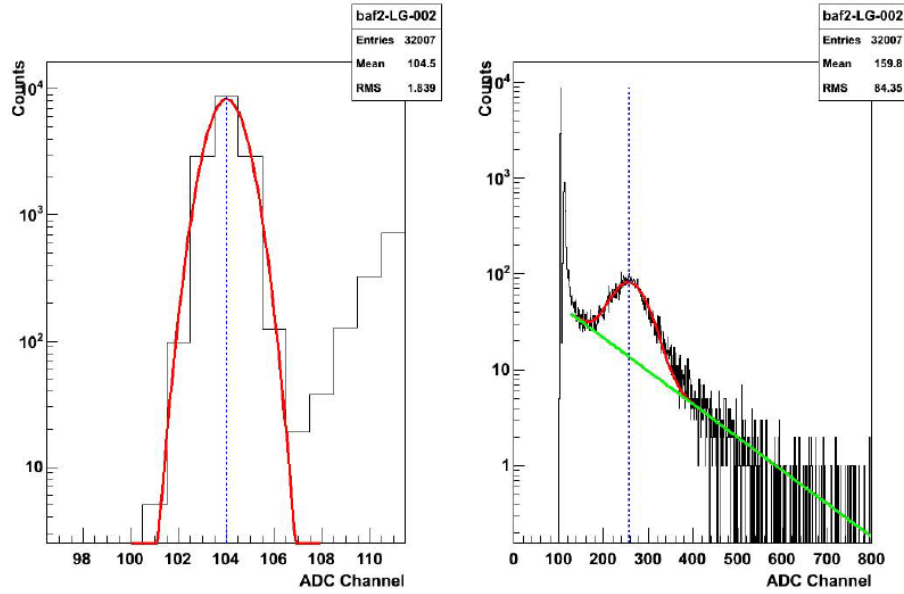
Figure 4.6: The energy deposition in channels of cosmic muons in a BaF_2 crystal. Left: The pedestal fitted with a Gaussion distribution to determine the peak position. Right: The cosmic peak with the corresponding fit in red. In green the background is drawn.

the minimum ionizing peak correponds to the amount of deposited energy in the BaF_2 crystal which is 37.7 MeV. The QDC channel numbers are proportional to the energy deposition in a crystal. Hence, knowing QDC channels and the full energy range they cover, the position in channels of the minimum ionizing peak can be calculated. If the crystals are uncalibrated the peak has to be shifted to the correct position by changing the high voltage (HV) for every single crystal. To calculate the right HV the gain for every crystal is needed:

$$\text{gain} = \frac{\text{energyrange}}{\text{range}_{QDC} - \text{pedestalposition}}. \tag{4.4}$$

For our beamtimes the range was set to 1000 MeV in a QDC range of 4096 channels. With the obtained gain the new HV value can be estimated

$$\text{gainbias} = \text{HV}_{old} - (\text{BaF}_2\text{slope} \cdot \log{(\text{peakposition} - \text{pedestalposition})}), \tag{4.5}$$

$$\text{HV}_{new} = \text{BaF}_2\text{slope} \cdot \log{\left(\frac{37.7 \text{ MeV}}{\text{gain}}\right)} + \text{gainbias}, \tag{4.6}$$

where BaF_2slope equals 153.

The maximum photon energy in the experiment is roughly 1400 MeV, hence a calibration using two reference points with energies smaller than 100 MeV is not satisfying.

To check if the calibration also holds for higher energies the invariant masses of the π^0- and η-mesons are determined. It turns out that the mass for the π^0 is some MeV off, while for the η the situation is worse. To get the higher energies in the right correlation to the channel numbers, another calibration step is necessary. Starting with the check of the π^0-mass, one needs events with two neutral hits. In principle the same method like used for the Crystal Ball can be applied for calibrating the TAPS detector. But due to the smaller solid angle covered by TAPS, the chance to have two neutral events only in this detector system is very small. This lowers the possible statistics which is needed to get a clean and visible signal. To increase the statistics to be able to calibrate the TAPS crystals individually one allows for one hit in TAPS and one in CB. Depending on the target material, one has more or less background. The
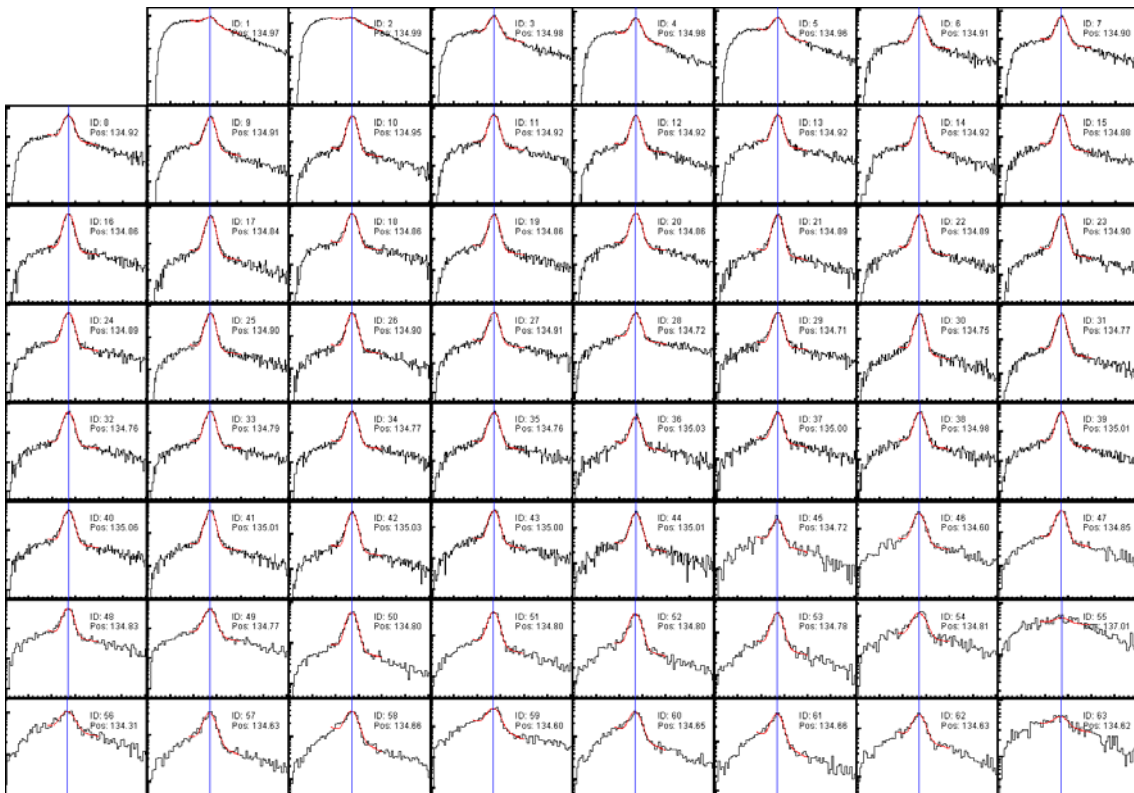
Figure 4.7: The invariant mass spectra for all the 63 BaF$_2$ crystal in block A. In red the fit to the π^0-peak is shown.

figure 4.7 shows the 63 channels of block A for the Carbon beamtime, where it was much easier to fit the signals in the single crystals. For the innermost crystals as well as for the outermost ones, the peaks were hard to identify, so it was impossible to fit the invariant mass reliably. That means no correct gain factor could be obtained. For those crystals the factor was extrapolated using the information from neighbouring

crystals or taken from other runs where the signal was clean enough to determine this factor. In figure 4.8 the comparison of the π^0-peak position before (a) and after (b) the energy calibration is shown. After the π^0-calibration the η-mass position was
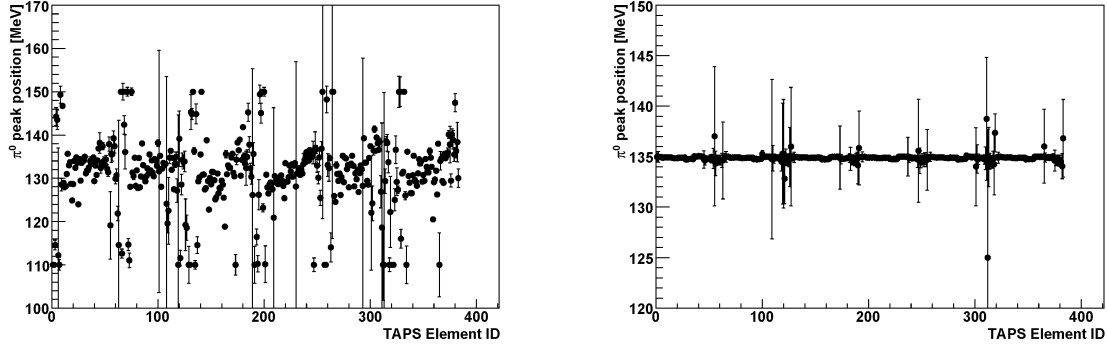
(a) Position of the π^0 peak of every BaF$_2$ crystal before the TAPS calibration.

(b) Position of the π^0 peak of every BaF$_2$ crystal after the TAPS calibration.

Figure 4.8: Calibration of the BaF$_2$ modules using the π^0-meson as a fixed point (Carbon beamtime).

checked. Unfortunately the same problem we had in the CB occured here and the mass was about 10 MeV off. This shows that the correlation between channel numbers and energy is not linear. To get the η-meson mass at the right position a second order calibration is necessary for the TAPS detector. With the statistics in the case of the π^0-meson already being poor, the invariant mass of the η would be impossible to fit. Boris Lemmer developed a new method to calibrate the η-meson in the BaF$_2$ crystals. For details see his diploma thesis [Lem09]. The main idea is to calibrate the detector system ringwise. Figure 4.9(a) shows the situation before, figure 4.9(b) after the second order ring correction.

4.2.2. BaF$_2$ Time Calibration

The time calibration for the TAPS crystals is similar to the calibration for the CB crystals. The big advantage is the use of CFDs (**C**onstant **F**raction **D**iscriminator) instead of LEDs. Here the time dependence on the height of the signal is negligible. Nevertheless the peak position of the time difference from two hits in TAPS has to be shifted to zero with the same method used for the CB. Figure 4.10(a) shows the achieved result with a FWHM of 670 ps. The timing of TAPS against the tagger as shown in figure 5.8(b) gives a time resolution of 1.1 ns (FWHM). Very nicely the separation between photons and neutrons can be seen.
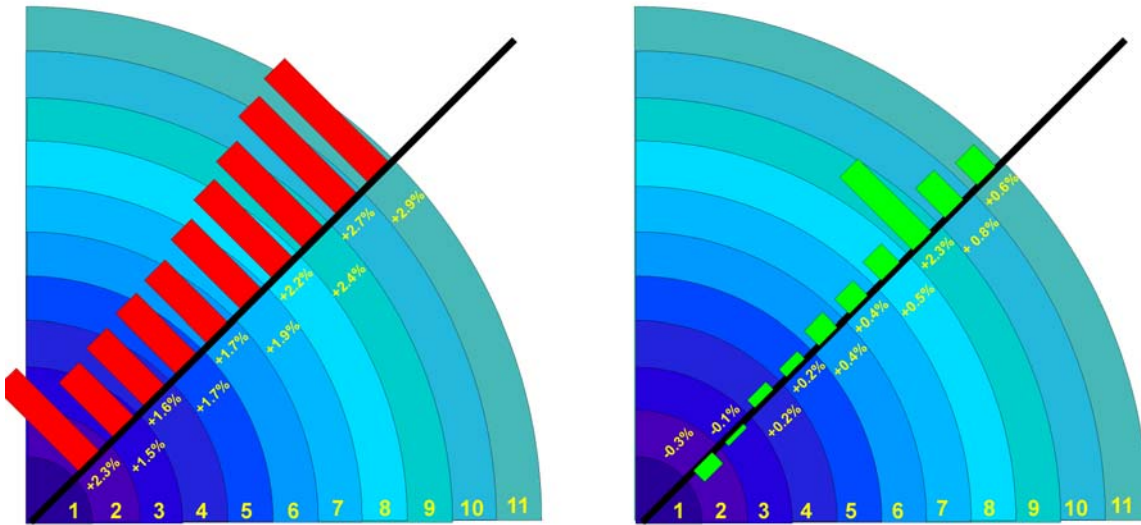
(a) Deviation of the η peak from the PDG value for every TAPS ring in percent before the 2nd order calibration.

(b) Deviation of the η peak from the PDG value for every TAPS ring in percent after the 2nd order calibration.

Figure 4.9: Position of the η-meson in TAPS for the Carbon beamtime.
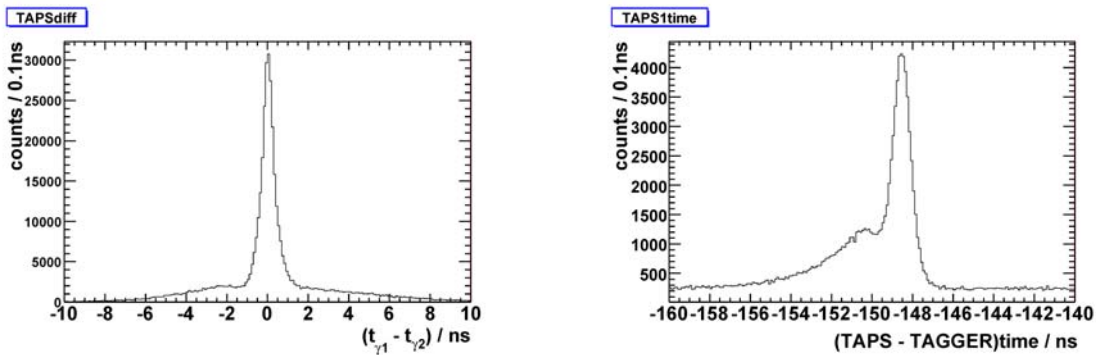
(a) Time difference for two hits in the TAPS detector.

(b) Time of a neutral hit in TAPS against the tagger time.

Figure 4.10: Results of the time calibration of TAPS for the Carbon beamtime.

4.2.3. Veto Plastic Scintillator Energy Calibration

The Veto plastic scintillators are used to discriminate between charged and uncharged particles using the well known $\Delta E/E$ method. Once a particle is marked charged due to a hit in the plastic scintillators one further can distinguish between charged pions and protons by placing properly set cuts in the ΔE versus E histogram. To make use of this method, all 383 plastic scintillators have to be energy calibrated. This method was developed by Thomas Geßler and is described in his Bachelor thesis [Geß08]. Theoretical models were used to calculate the energy depostion of protons in the plastic scintillators. In the end the proton bands of each module should overlay so it is possible to set one cut which fits for all. In figure 4.11 the sum of all Veto detectors are displayed together with the applied proton cut which will be used in the analysis to identify the protons.
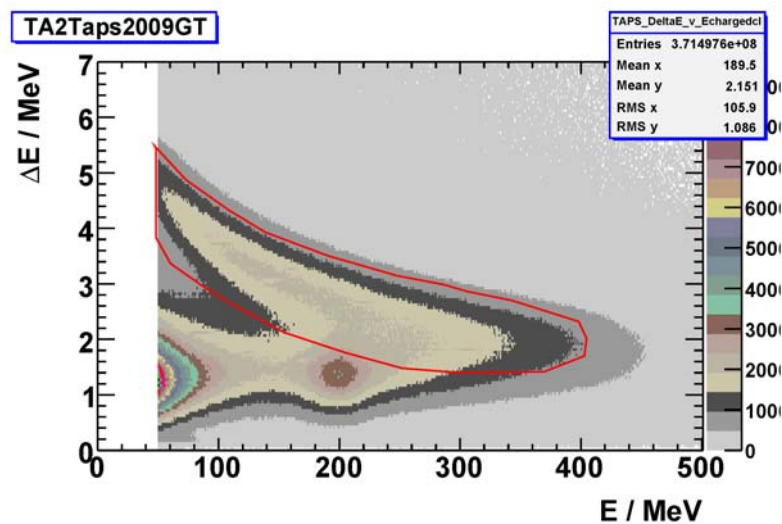
Figure 4.11: ΔE vs E for the TAPS Veto plastic scintillators. In red the cut to identify protons is shown.

4.3. PID

The Particle Identifiction Detector (PID) is used to discriminate charged from uncharged particles like the veto plastic scintillators in front of TAPS do.

The PID consists of 24 plastic scintillator strips. Whenever a particle is registerd in the Crystal Ball, the PID element in front of this crystal is checked if there was an energy deposition in its corresponding scintillator strip. So it is important to know the position of the single PID elements relative to the position of the NaI-crystals. Therefore the Φ-angle of every scintillator strip has to be known. To get the right correlation one fills a 2D histogram as shown in figure 4.12(a) whenever there is a coincident hit in the CB and the PID. The peak position for every PID strip can be determined by projecting the 2D histogram to the time axis as it is shown for PID element 3 in figure 4.12(b). The obtained correlation is stored in the configuration file. With the
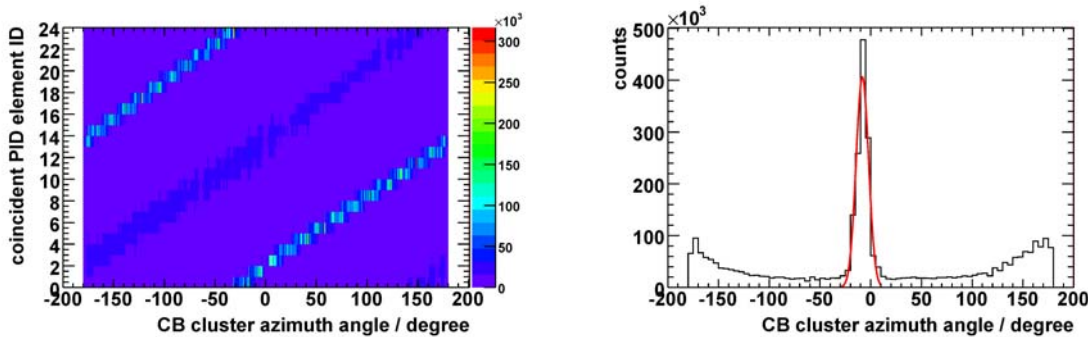
(a) The azimuthal angle Φ is plotted versus the corresponding PID element number.

(b) Projection of the left figure onto the time axis for PID element 3.

Figure 4.12: For coincident hits of the CB and the PID: angle calibration of the PID for the Carbon beamtime.

exact position of the PID detector relative to the NaI-crystals known, the next step can be its energy calibration. Different types of particle deposit different amounts of energy. In the ΔE versus E plot one can see the different bands for the protons and charged pions. To separate them a so called banana cut can be applied. After the energy calibration one cut would be enough for all 24 PID strips. But because of the small number of detector elements I decided to do no energy calibration and place a separate cut in each of the 24 histograms. One example is shown for element number 2 in figure 4.13.

4.4. Tagger

In the case of the tagger, we have to determine the offset parameter for every channel like it was done for the TAPS detector. To reduce the background the tagging efficiency
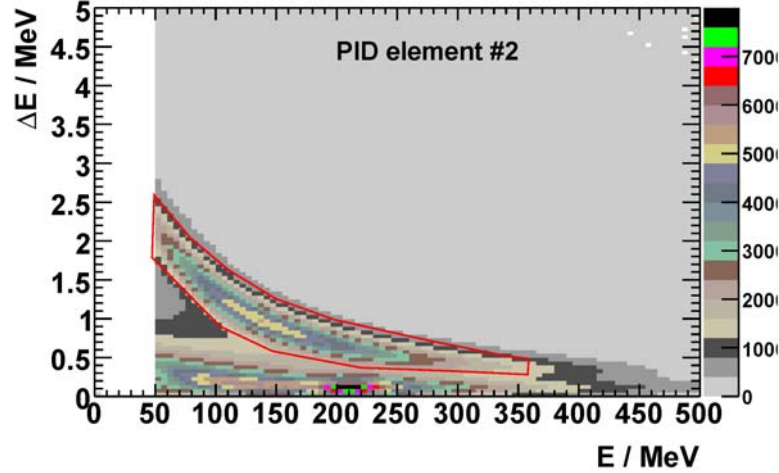
Figure 4.13: dE versus E for the PID element number 2. In red the applied proton cut is shown.

runs, running with a low current, can be used for the time alignment. The Pb-glass detector is the trigger so this will start the TDC. A hit in the tagger ladder will stop the TDC. For every ladder scintillator module the peak position is determined by a Gaussian fit and used as a new offset value. The result is illustrated in figure 4.14.

4.5. Calibration Stability

Looking for possible in-medium modifications of the ω-meson it is necessary to have a very accurate energy calibration. One has to make sure, that observed diviations from the vacuum value are not due to a poor calibration. As a first step to check the calibration one has to prove that the mass of a pion and an eta meson is independent of its momentum. Hence a two-dimensional histogram is produced where the momentum of two photons is plotted versus the mass of the two photons (see figure 4.15). 50 MeV wide slices in the momentum range from 100 MeV/c to 1100 MeV/c are generated and projected on the mass axis. In these 12 histograms (figure 4.16) the π^0 and η peaks are fitted by the Novosibirsk function:

$$\mathrm{f(x)} = \mathrm{A} \cdot \exp\left[-\frac{1}{2}\left(\frac{\log \mathrm{q}_x}{\mathrm{d}}\right)^2 + \mathrm{d}^2\right] \tag{4.7}$$
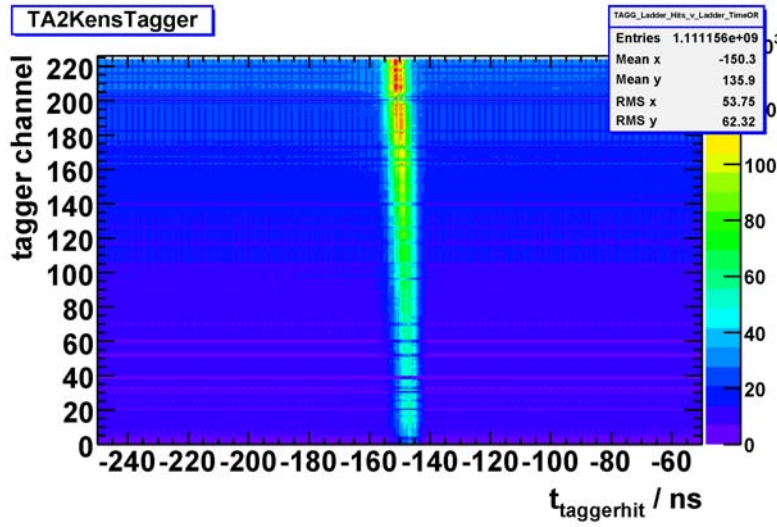
Figure 4.14: Tagger channel versus the time of a tagger hit.
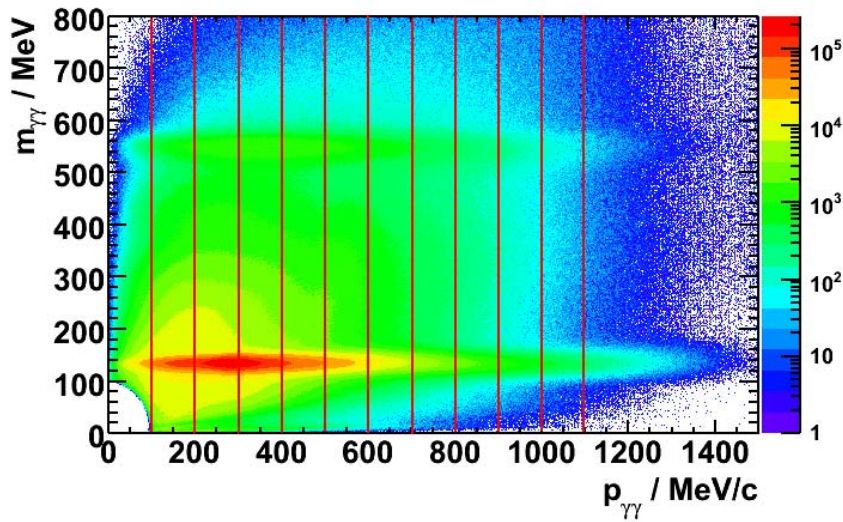
Figure 4.15: Momentum of two photons versus their invariant mass for the Carbon beamtime.

where

$$q_x = 1 + \frac{2.35(\mathrm{x} - \mathrm{x}_0)}{\mathrm{FWHM}} \cdot \frac{\sinh(\mathrm{d}\sqrt{\log 4})}{\log 4}. \tag{4.8}$$
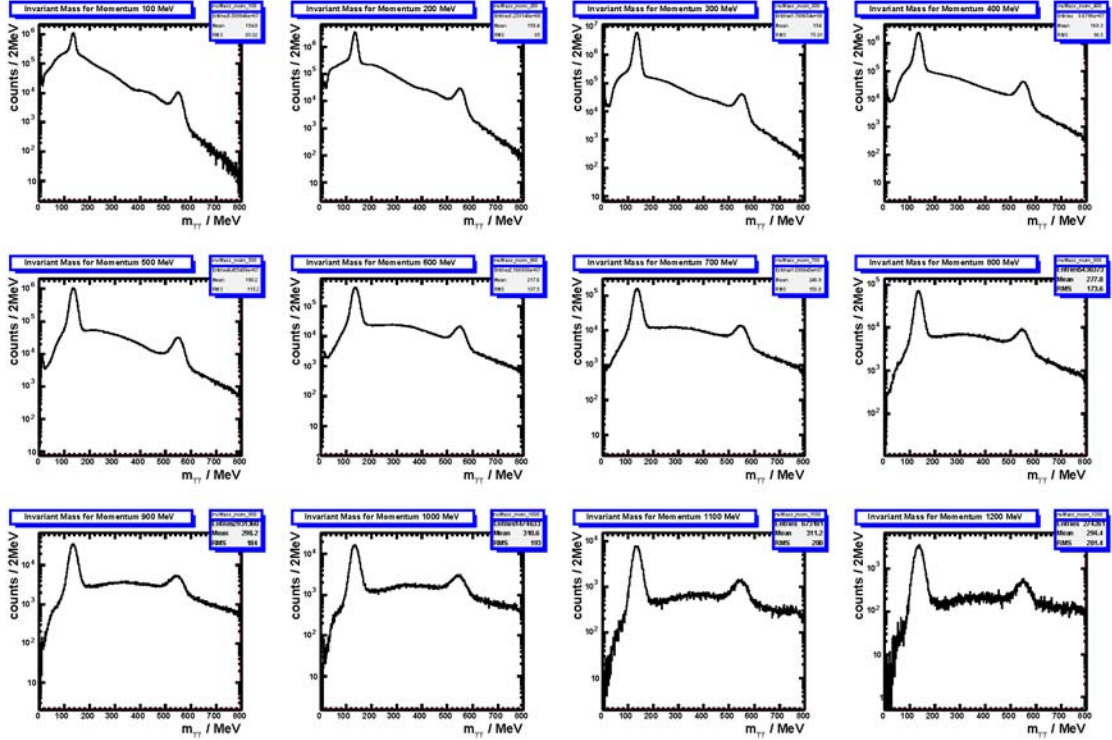
Figure 4.16: Momentum of two photons versus their invariant mass for the Carbon beamtime.

The parameter A gives the amplitude of the signal and d is the asymmetry parameter. The value of the peak position x_0 is plotted for the different momentum bins in figure 4.17(a) for the π^0 and in figure 4.17(b) for the η meson. This check is performed for all the three ω production beamtimes. In figure 4.18 the two dimensional histogram for the August Niobium beamtime is shown. Already here it is visible that for Niobium there are many more low energetic events compared to the Carbon target. The results for the π^0- and η peak positions for the two Niobium beamtimes are plotted together with the Carbon data in one picture. The good agreement is clearly seen in figure 4.19(a) for the π^0-meson and in figure 4.19(b) for the η-meson. But not only the momentum-independentness of the mass, also the width is important. To prove that there are no larger deviations the invariant mass of the π^0 (4.20(a)) and for the η (4.20(b)) for the three beamtimes are plotted in one histogram. The width was determined by a Gaussian fit and the results are listed in table 4.1. Since the masses
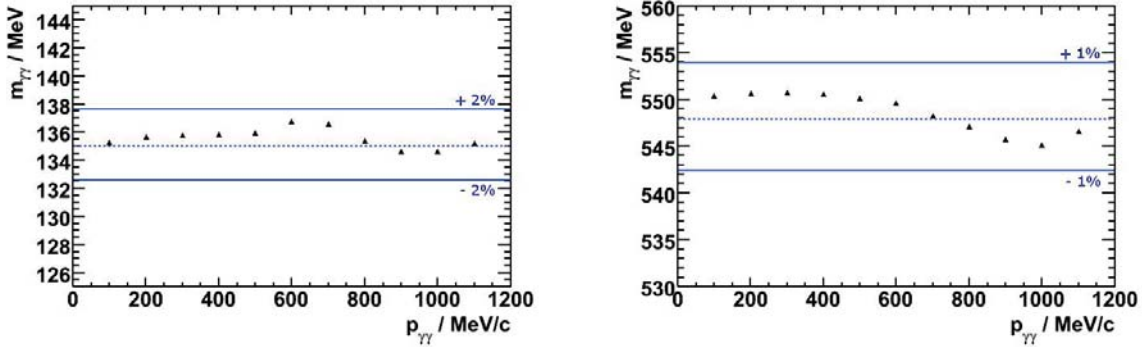
(a) Momentum dependence of the π^0 invariant mass.

(b) Momentum dependence of the η invariant mass.

Figure 4.17: Stability of the calibration in a large momentum range.
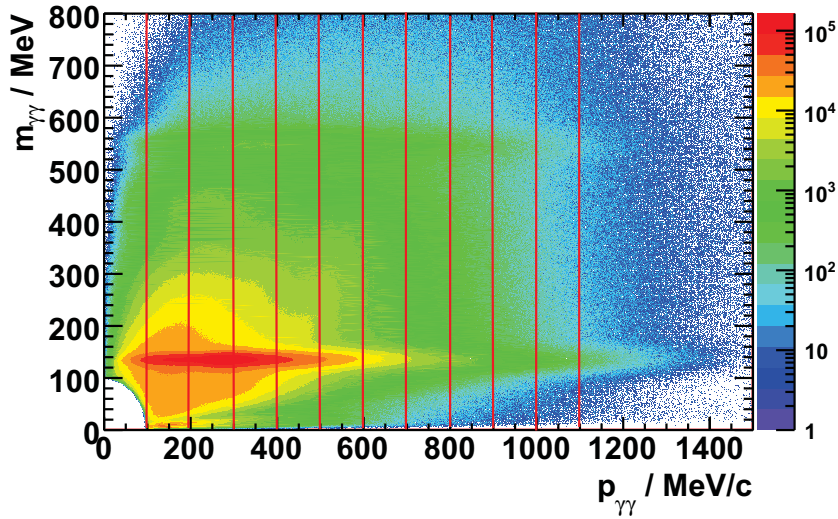
Figure 4.18: Momentum of two photons versus their invariant mass for the August Niobium beamtime.

beamtime	peak position π^0	σ_{π^0}	peak position η	σ_η
April/May	135.49MeV	8.28MeV	549.36MeV	16.23MeV
June	135.51MeV	8.06MeV	549.93MeV	16.13MeV
August	135.63	8.19MeV	549.85MeV	16.25MeV

Table 4.1: Position and width of the π^0- and η-meson for the three beamtimes.
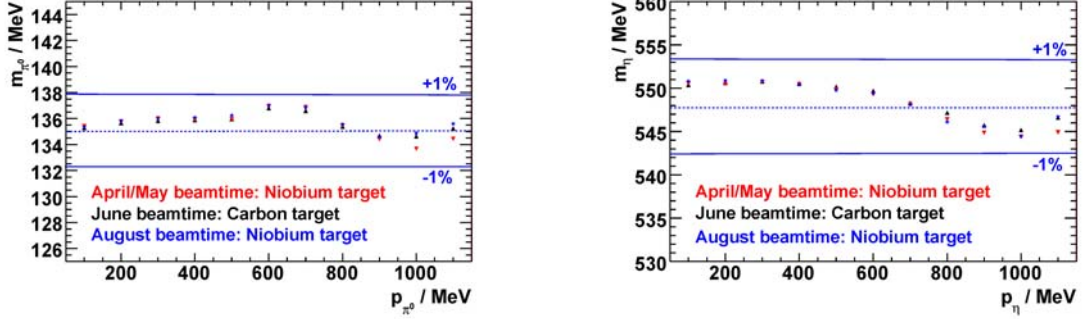
(a) Momentum dependence of the π^0 invariant mass.

(b) Momentum dependence of the η invariant mass.

Figure 4.19: Stability of the calibration in a large momentum range.
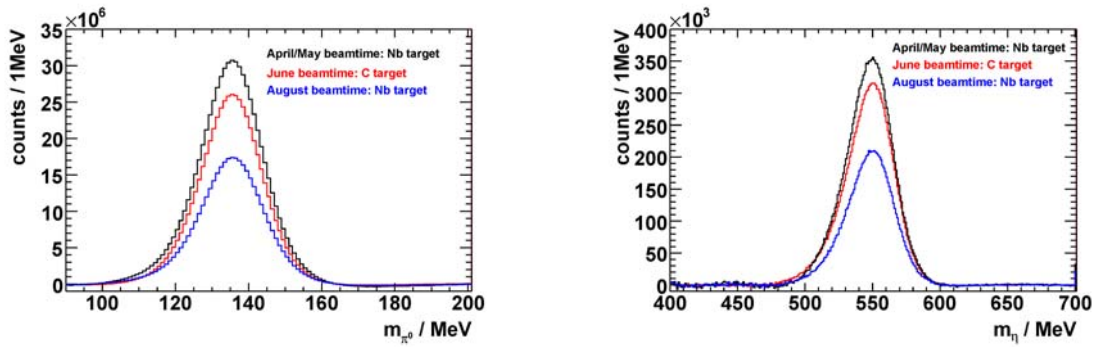
(a) π^0 invariant mass for all 3 beamtimes

(b) η invariant mass for all 3 beamtimes

Figure 4.20: Calibration check for all 3 beamtimes

are stable over a large momentum range and comparable in the three beamtimes it is possible to compare the obtained results for the ω-analysis for the different targets. So it can be excluded that a (possible) observed in-medium effect arises from a wrongly calibrated detector.

Chapter 5.

Data Analysis

Once the data is calibrated, the events of interest have to be selected. Looking for the reaction

$$\gamma A \rightarrow (A-1)\omega p \rightarrow (A-1)\pi^0\gamma p \rightarrow (A-1)\gamma\gamma\gamma p \qquad (5.1)$$

three photons are in the final state. From their 4-momenta the ω will be reconstructed. For an exclusive analysis, the proton needs to be identified, too.

In the following, the cuts applied for the event selection as well as the reconstruction and discrimination of particles are described.

5.1. Event Selection

According to equation 5.1 three photons are in the final state which have to be registered in the detector systems. In addition the proton can be required. This leads to two different analysis parts which were performed within this thesis:

- **exclusive analysis**: three photons and a proton are required in the final state.

- **semi-exclusive analysis**: three photons are required in the final state.

For the exclusive analysis the proton is identified via ΔE versus E in the PID and in the TAPS Veto detector and in addition via time of flight (ToF) in the TAPS Vetos.

5.2. Particle Identification

In the analysis of the experimental data one has to distinguish on the lowest level between charged and uncharged particles. For the charged particle identification the PID located in the Crystal Ball and the Veto detectors in front of TAPS are used.

5.2.1. Photons

For the identification of photons the particle has to be marked as uncharged. Whenever a photon creates an electromagnetic shower in one of the calorimeters, the corresponding PID / Veto detector in front should not respond to mark this event as uncharged. To distinguish between photons and neutrons tight time cuts are applied in the two detector systems.

5.2.2. Protons

In first order charged particles can be identified using the PID in the Crystal Ball or the Veto detectors in front of TAPS. To identify a charged particle as a proton, further cuts have to be applied in both detectors.
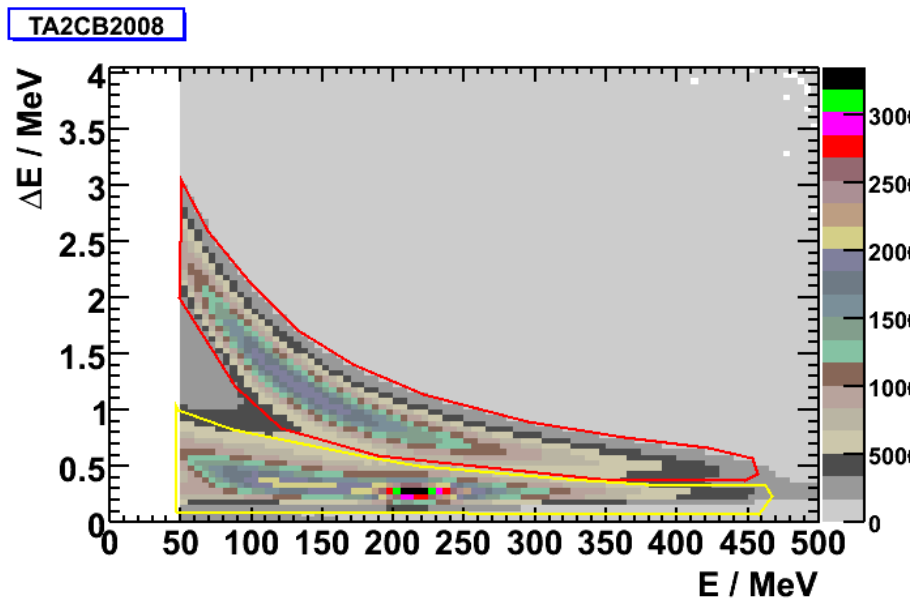
Δ E vs E in the PID

Figure 5.1: The energy in the NaI crystals is plotted versus the energy deposition in the PID. Two bands can be identified. Protons can be selected by placing the cut shown in red, charged pions lie in the area indicated by the yellow cut.

Whenever a PID strip in front of a NaI cluster has fired, the event is marked as charged. Looking at the energy deposition in the PID versus the corresponding cluster energy

in the NaI two bands can be seen. This can be used to further specify the type of charged particle. For the exclusive analysis the proton has to be identified, which can be achieved by a cut around the proton band in the two dimensional Δ E versus E plot as it is shown in figure 5.1.

Proton Identification in the Veto Detectors of TAPS

The charged particle can be identified in the Veto detector via ΔE vs E, which works quite similar to the one used with the PID detector. Again, the cluster energy of the BaF_2 crystals is plotted versus the corresponding energy deposition in the Veto plastic scintillator. The maximum energy deposition in a BaF_2 crystal is 400 MeV. Two body kinematics calculations showed that for the reaction $\gamma p \rightarrow \omega p$ the proton can have energies up to 600 MeV for the maximum incident photon energy of 1400 MeV as it is shown in figure 5.2. Due to the higher kinetic energy T_p these protons will be faster
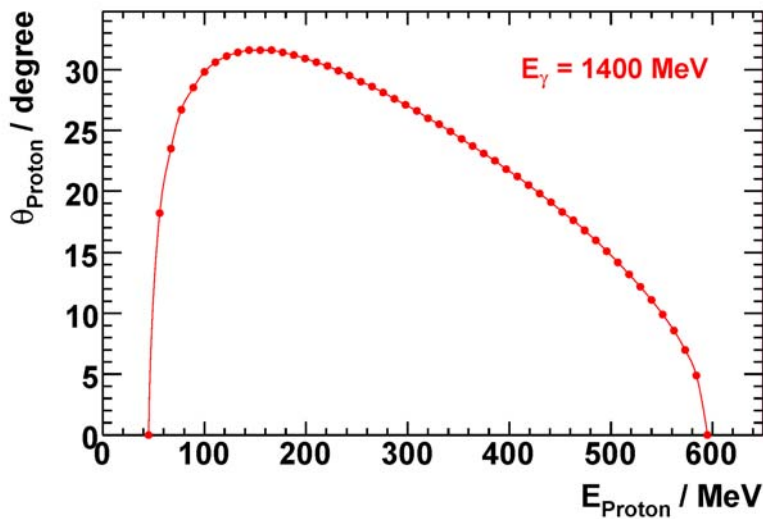
Figure 5.2: Two body calculations for the reaction $\gamma p \rightarrow \omega p$ for an incoming photon energy $E_\gamma = 1400$ MeV. The energy of the proton is plotted versus its θ angle.

and therefore their energy deposition in the crystals is smaller. Looking at the ΔE vs E plot in figure 5.3 these events can be found between the minimum ioninizing peak and 400 MeV and have to be taken into account for the correct cut setting. The
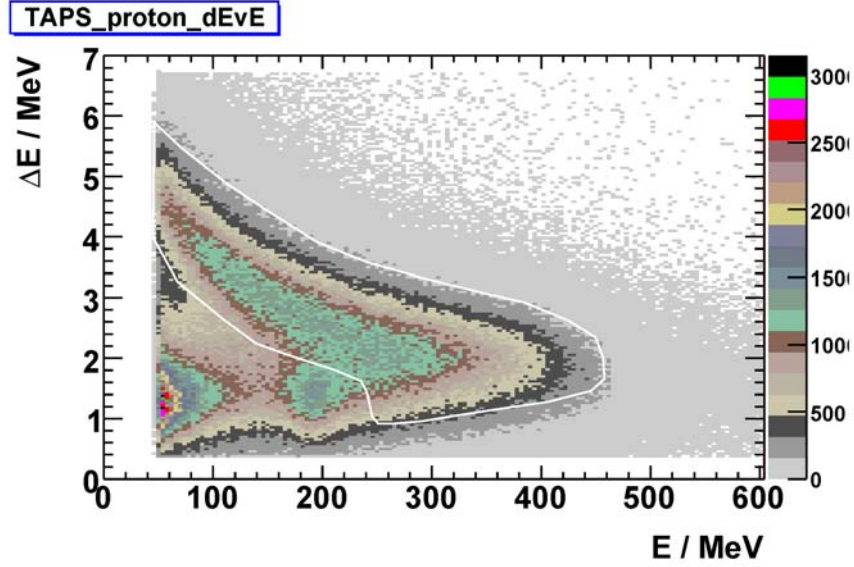
Figure 5.3: The energy in the BaF$_2$ crystals is plotted versus the energy deposition in the Veto plastic scintillators. The white line indicates the applied proton cut.

difficulty is not to cut to tightly and thereby loosing protons, but also the cut should exclude the region around the minimum ionizing peak. Therefore the flight time of the protons can be calculated to see how large the corresponding energy deposition in the crystals is. The flight time for photons can be calculated to:

$$t_\gamma = \frac{d}{\cos\theta \cdot c} \tag{5.2}$$

with the distance d between target and TAPS and the speed of light c. For a proton, the flight time is calculated to:

$$t_p = \frac{d}{\cos\theta \cdot \beta \cdot c} \tag{5.3}$$

with

$$\beta = \frac{T_p}{T_p + m} \cdot \sqrt{1 + \frac{2m}{T_p}} \tag{5.4}$$

In table 5.1 the calculated values are listed for protons with $T_p = 400$ MeV and $T_p = 600$ MeV. The protons can be detected in TAPS in the polar angle range $0° \leq \theta \leq 20°$. Hence, we are interested in the fastest protons, the calculations are

T_p [MeV]	β	t_γ [ns] for $\theta = 0°$	t_p [ns] for $\theta = 0°$	$t_p - t_\gamma$ [ns] for $\theta = 0°$
400	0.713	4.87	6.83	1.96
600	0.792	4.87	6.15	1.28

Table 5.1: Caculated flight time for photons and protons for the distance target - TAPS (1.46 m).

performed only for $\theta = 0°$. The calculated values are shown together with the measured flight times versus the energy of the corresponding BaF_2 cluster in figure 5.4. The prompt peak ($t = 0$ ns) is indicated by the white line. Protons with $T_p = 400$ MeV are registered 2.0 ns after the photons, those with $T_p = 600$ MeV 1.3 ns after the photons.
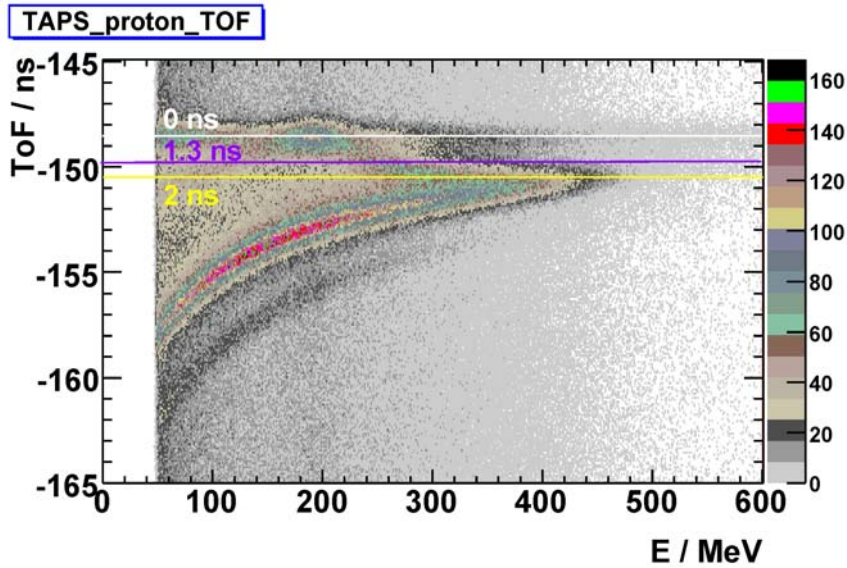
Figure 5.4: Time of flight versus the energy of the corresponding BaF_2 cluster. The timing of the prompt peak is indicated by the white line. The flight time for protons with $E_p = 400$ MeV and $E_p = 600$ MeV are shown in yellow (2 ns) and purple (1.3 ns), respectively.

These calculations can be used to place a proper cut, including the area up to 1.3 ns. The applied cut is shown in figure 5.5. From the cut placed in figure 5.5 the energy of the proton can be read off. This value can be used to place the cut in the ΔE vs E
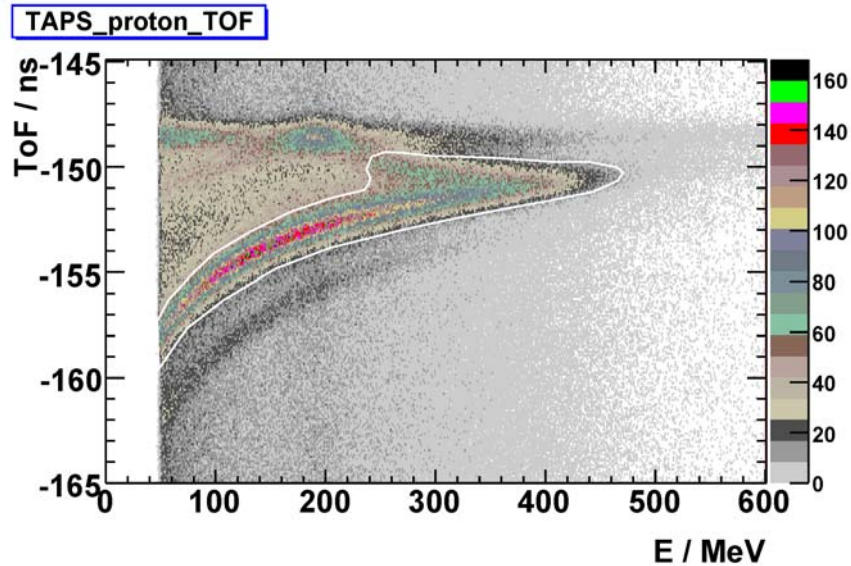
Figure 5.5: Time of flight versus the energy of the corresponding BaF$_2$ cluster for the carbon beamtime. In white the cut for the proton identification is drawn in. In addition also a deuteron band can be seen.

plane which is shown in figure 5.3.

Dead Time Effects

A proton can only be registered as a charged particle in TAPS if the Veto plastic scintillator is not busy at the time the proton passes by. Due to the high count rates in TAPS of around 400 kHz, the readout electronics is running at the limit. Therefore, the dead time of the system can cause misidentifications of particles.

To check if dead time effects really play a role, the amount of charged and uncharged particles are plotted versus their flight time in figure 5.6. In the left panel the situation is shown for the carbon data, in the right panel for the niobium data. The direct comparison shows that the carbon data is much cleaner and less distorted from dead time effects of the Veto detector. For the charged as well as for the neutral particles plateaus on both sides of the prompt peak are visible. For the niobium beamtimes the consequences of the high count rates are directly visible. The tagger plateau is falling for charged particles and rising for neutral particles. The falling tagger plateau indicates charged particles passing the Veto scintillator while it is busy. As a
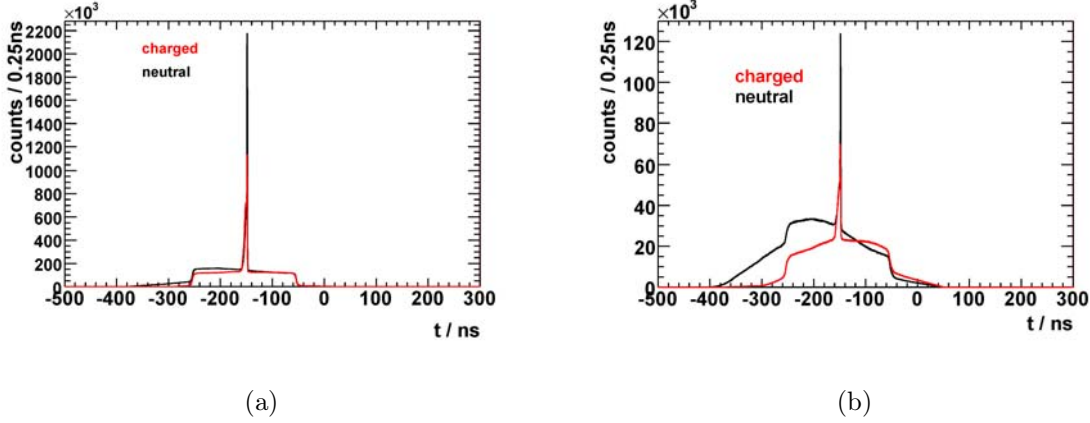
Figure 5.6: Flight time for charged particles in red and neutral particles in black registered in the innermost BaF$_2$-ring of the TAPS detector. (a) Carbon beamtime, (b) niobium beamtimes.

consequence the charged particle is marked as neutral which leads to the rising plateau of the neutral events.

5.3. Cuts

5.3.1. Incident Photon Energy

As pointed out in chapter 2.7.1, BUU transport calculations predicted a change in the ω meson lineshape due to in-medium modifications. The expected differences for the three scenarios (no in-medium modification, collisional broadening, collisional broadening plus mass shift) seem to be most pronounced close to the production threshold $E_{\gamma,thresh} = 1108$ MeV. Therefore this analysis was performed in the photon energy regime from 900 to 1300 MeV, taken into account that the threshold for ω production on nuclei is lower than the production on a free nucleon.

5.3.2. Kinetic Energy of the π^0

To avoid distortion of the ω signal due to a rescattering of the pion in the nucleus, a cut on the kinetic energy of the π^0 meson was applied: $T_{\pi^0} > 150 MeV$. Monte Carlo simulation results presented in chapter 2.7.3 showed that such a cut suppresses the number of events where the pion undergo final state interactions.

5.3.3. Angular Cuts

Looking at the geometry of the present detector setup in Mainz, roughly the full solid angle of 4π is covered by CB and TAPS. The entrance and exit holes in the CB cover an angular range from $0° \leq \theta \leq 20°$ (downstream) and $160° \leq \theta \leq 180°$ (upstream). The downstream region is covered by the TAPS detector (see figure 5.7).
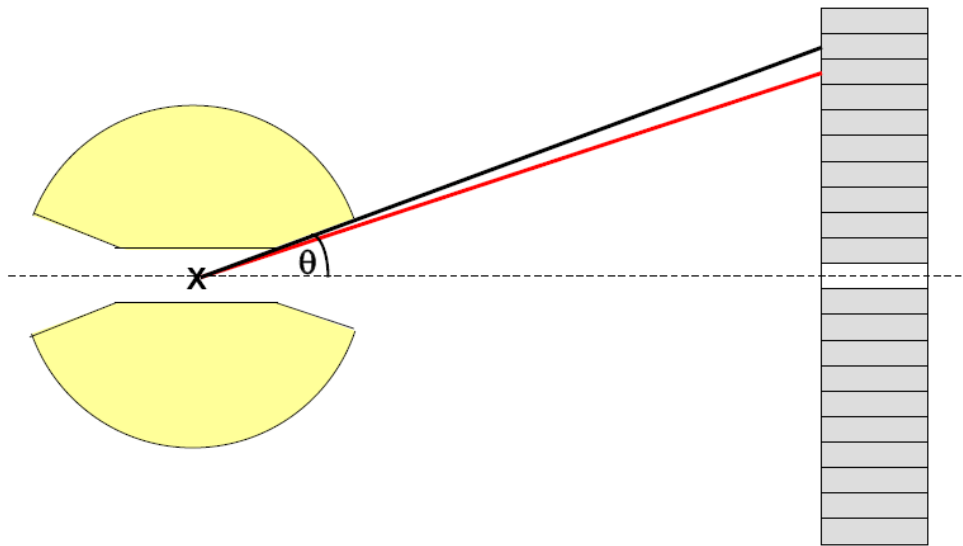
Figure 5.7: Schematic view of the Crystal Ball (yellow) and the TAPS detector (grey). The black line indicates a polar angle of $\theta = 20°$, the red line $\theta = 17°$.

Nevertheless it is necessary to exclude a certain angular range to avoid distortion due to insufficient reconstructed shower energies. In table 5.2 the applied angle cuts are listed.

Detector system	θ angle cut	ϕ angle cut
CB	$23° \leq \theta \leq 157°$	$23° \leq \theta \leq 157°$ and $-23° \leq \theta \leq -157°$
TAPS	$0° \leq \theta \leq 17°$	—

Table 5.2: Angular cut settings.

For the Crystal Ball additional cuts in ϕ are applied to exclude the inactive area at the equatorial plane, for TAPS the whole ϕ angular range can be used.

5.3.4. Cluster Threshold

Every time a photon hits the detector material it will generate an electromagnetic shower which deposits a certain amount of energy in the crystals. But it can also happen that a single photon will be registered as two showers if the threshold energy of the cluster is too low. This happens when part of the electromagnetic shower escapes into disjunct neighbouring detectors. These "split offs" have, , typically quite low energies. (< 50 MeV). Monte Carlo simulations show a strong contribution to the three γ invariant mass spectrum from single η photoproduction $\eta \to \gamma\gamma$ due to the large cross section in the energy regime we are interested in. To suppress the contributions from split-off events the energy threshold for each cluster is set to 50 MeV.

5.3.5. Prompt Time Coincidences

For both analysis methods (exclusive and semi-exclusive), three photons are required in the final state. To identify the photons, tight time cuts are applied in the Crystal Ball and in the TAPS detector. In addition the detector systems Tagger, CB and TAPS have to be in coincidence. To ensure promptness and coincidences of the signals, the following three different time cuts are applied.

Tagger minus TAPS Timing

Both detector systems run in the common stop modus, i.e. the start signal for Tagger and TAPS is generated individually while the trigger gives the common stop signal. To eliminate uncertanties from the trigger, the relative timing between Tagger and TAPS is given by:

$$\Delta t = (t_{trigger} - t_{TAPS}) - (t_{trigger} - t_{Tagger}) = t_{Tagger} - t_{TAPS} \tag{5.5}$$

The timing of neutral hits in TAPS is shown in figure 5.8. The photons are within the prompt peak, located around zero. To select these prompt photons, the peak was fitted with a Gaussian distribution and time cuts were applied corresponding to $\pm 3\sigma$ of the fit.
The tail on the right side comes from neutrons or misidentified protons. Protons can be wrongly marked as neutral particles due to dead time effects in the Veto detector (see chapter 5.2.2). Massive particles, like neutrons and protons, do not travel with the speed of light c; that is why neutrons (and protons) need more time for the distance target - TAPS and therefore are registered at later times in the detector system.
The enhancement on the left side of the prompt peak comes from random hits in

the Tagger. To get rid of this background contributions, the random hits have to be subtracted (see chapter 5.3.6).
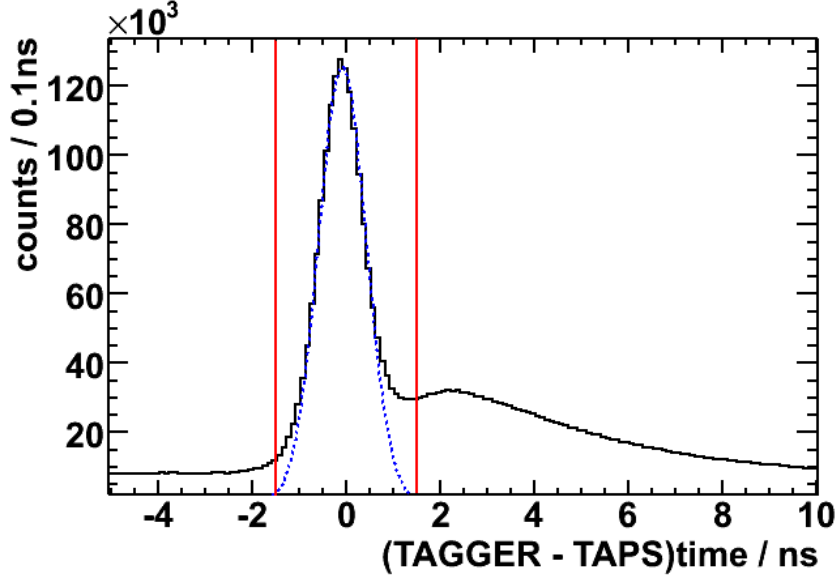
Figure 5.8: The timing of neutral hits in TAPS. To select photons, the peak was fitted with a Gaussian distribution (dashed blue line) and the applied time cuts ($\pm 3\sigma$) are indicated by the red lines.

CB minus Tagger Timing

The Crystal Ball readout, in contrast to the Tagger and TAPS detector, runs in a common start modus, i.e. the start signal is given by the trigger while the stop signals are provided by the individual NaI crystals. The relative timing between CB and Tagger can be calculated:

$$\Delta t = (t_{trigger} - t_{Tagger}) - (t_{trigger} - t_{CB}) = t_{CB} - t_{Tagger} \tag{5.6}$$

Figure 5.9 shows the timing for the neutral hits in the Crystal Ball. The distance to the target is much shorter compared to the TAPS detector. Therefore the separation of photons and neutrons is much poorer. Nevertheless, the photon peak was fitted and the cut limits were calculated in the $\pm 3\sigma$ range. Again the background contribution from random hits in the tagger is visible on the right side of the photon peak.
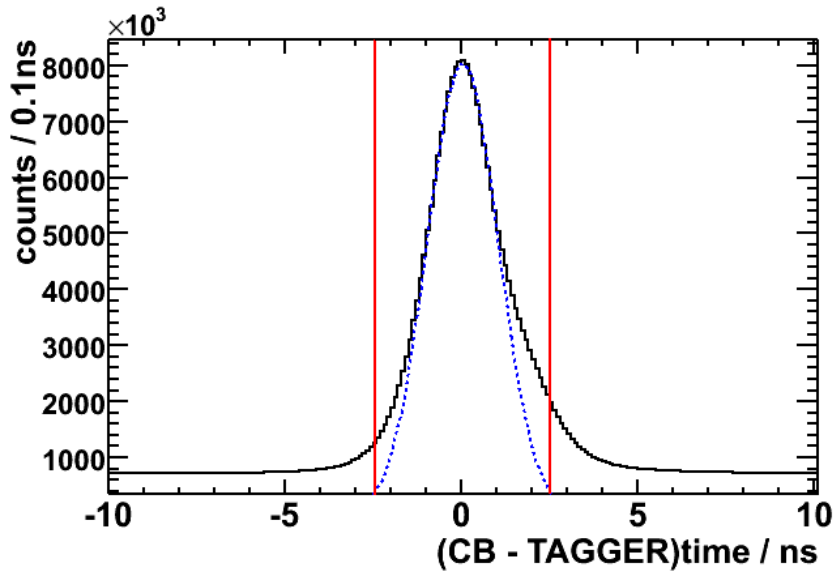
Figure 5.9: The timing of neutral hits in the Crystal Ball. To select photons, the peak was fitted with a Gaussian distribution (dashed blue line) and the applied time cuts ($\pm 3\sigma$) are indicated by the red lines.

CB minus TAPS Timing

Not only the Crystal Ball and the TAPS detector alone have to be prompt, also both detector systems have to be prompt with the Tagger.

$$(t_{CB} - t_{Tagger}) + (t_{Tagger} - t_{TAPS}) = t_{CB} - t_{TAPS} \tag{5.7}$$

The corresponding plot together with the applied time cuts is shown in figure 5.10.

5.3.6. Random Time Coincidences

As already indicated in the last section, looking at the time spectra of the different detector systems, one always sees a background contribution to the prompt peak. To avoid these contributions, the background can be subtracted using the sideband subtraction technique. Therefore one looks at the two dimensional histogram where the $t_{tagger} - t_{TAPS}$ timing is plotted versus the $t_{CB} - t_{tagger}$ timing shown in figure 5.11. Three bands are marked with colours:

- **Blue**: L1 sideband, TAPS time is not prompt.
- **Red**: L2 sideband, CB time is not prompt.
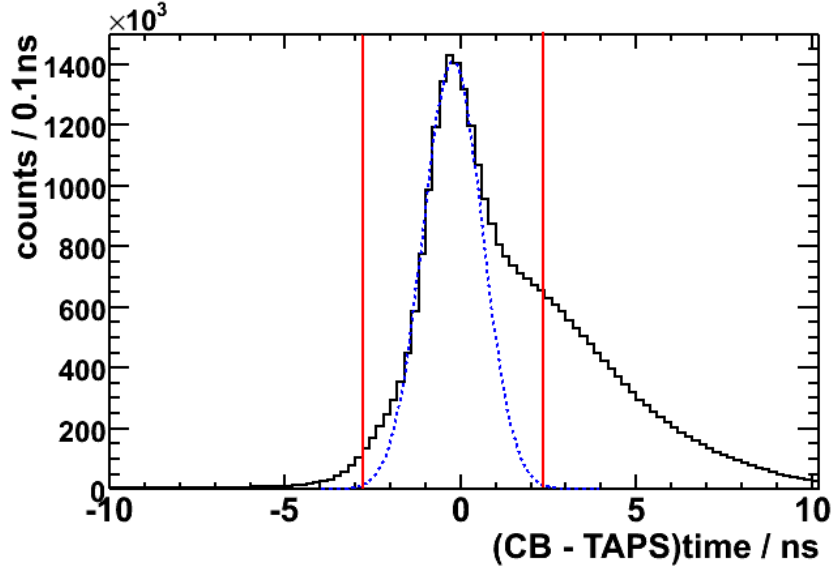
Figure 5.10: The timing of neutral hits in the CB minus the timing of neutral hits in TAPS. To select prompt photons the peak was fitted with a Gaussian distribution (dashed blue line) and the applied time cuts ($\pm 3\sigma$) are indicated by the red lines.

- **Green**: L3 sideband, Tagger time is not prompt.

It is obvious, that if only one of the detectors is prompt, background contributions due to random hits from the other detector systems will add to the time spectrum. In the following, two cases are distinguished:

- The three photons are detected in the Crystal Ball and TAPS (called now CB-TAPS events).

- All the three photons are detected in the Crystal Ball (called now CBonly events).

Only for the first scenario the contributions of all the three sidebands L1, L2 and L3 have to be subtracted. As it is shown as an exemple for the Crystal Ball in figure 5.12 two areas in the background region are chosen, normalized and than subtracted. With this method the background under the prompt peak is removed.
In figure 5.13(a) the contributions from the three sidebands are shown together with the original $\pi^0\gamma$ invariant mass spectrum. The contribution from the L1 sideband is strongly peaking in the region of the η meson mass. Here two photons from the η decay are detected in the CB and a third photon is detected in chance coincidence in TAPS, but not being prompt or only by chance. For details see [Lem09]. In the case that all three photons hit only the Crystal Ball detector, only the CB sidebands (see figure 5.12) are used to subtract the background contribution. The corresponding
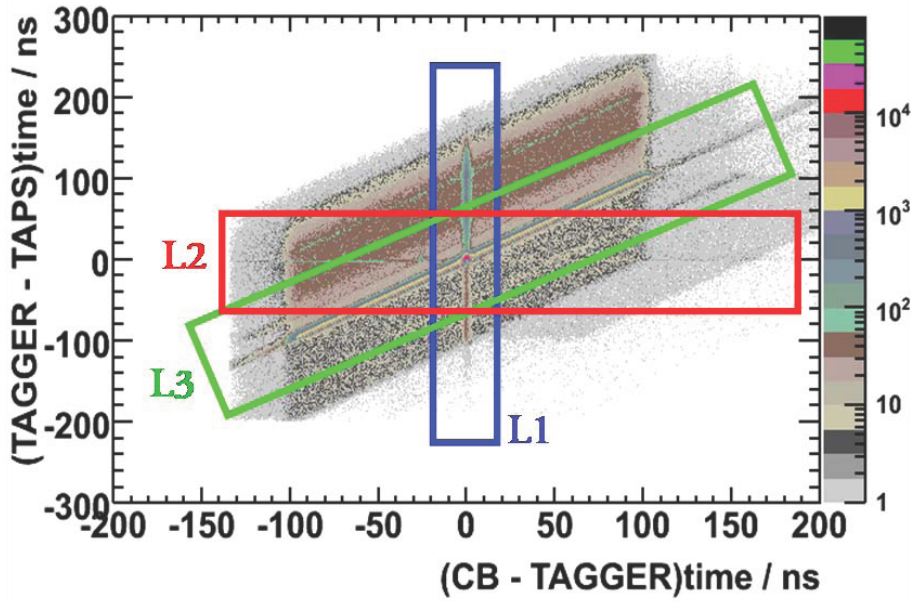
Figure 5.11: The time difference $t_{CB} - t_{tagger}$ is plotted versus the time difference $t_{TAPS} - t_{tagger}$. Prompt events are at the point where all the three bands cross.
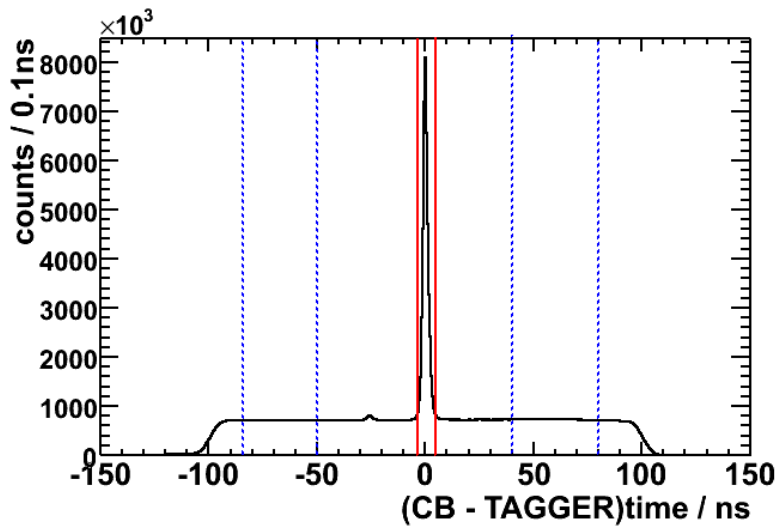
Figure 5.12: The timing of neutral hits in the Crystal Ball. In red the area of the prompt peak is marked, the dashed blue lines mark the areas of the background selected for the time sideband subtraction technique.

(a)   (b)
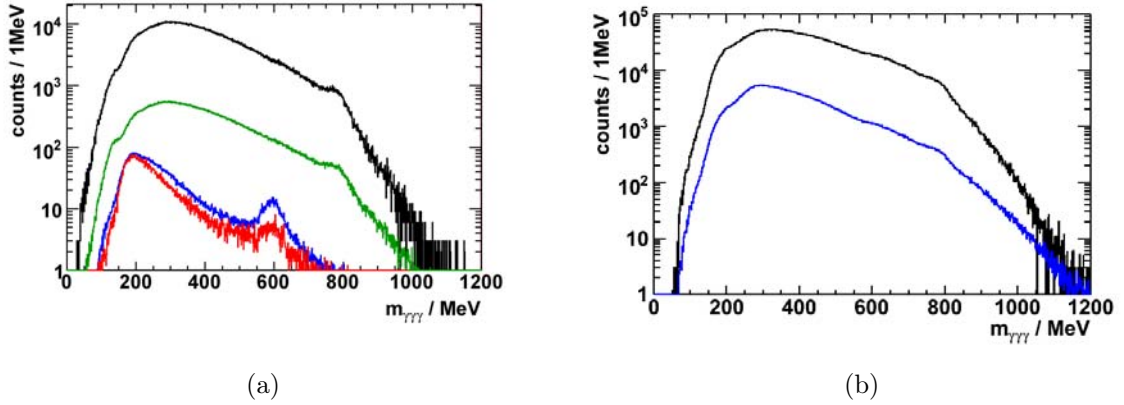
Figure 5.13: (a) The three photons are detected in the CB and TAPS. Raw $\pi^0\gamma$ invariant mass spectrum (black) with the contributions from the three sidebands L1 (blue), L2 (red) and L3 (green). (b) The three photons are detected only in the CB. Raw $\pi^0\gamma$ invariant mass spectrum (black) with the sideband contribution (blue).

spectra are shown in figure 5.13(b).The sum of the CBTAPS and CBonly invariant mass spectra after the time sideband subtraction is shown in figure 5.15.

With the applied time sideband subtraction technique wrongly assigned Tagger photons are removed. Looking at figure 5.14(a) the average tagger multiplicity for each event is five due to random hits in the Tagger. With the sideband subtraction the tagger multiplicity for prompt events is roughly one (see figure 5.14(b)); this ensures the right energy assignment to the incoming photons.

(a)   (b)
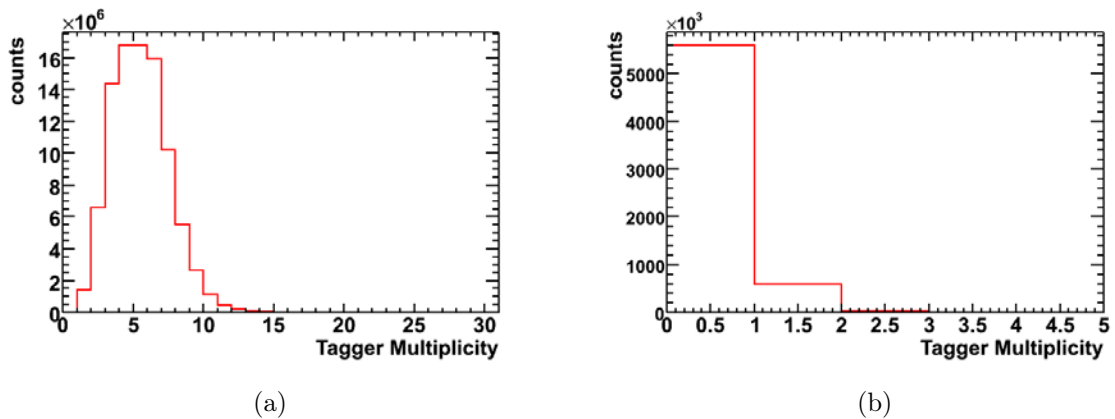
Figure 5.14: (a) Tagger multiplicity distribution without time cuts. (b) Tagger multiplicity distribution for prompt events.

5.4. Pion Sideband Subtraction Technique
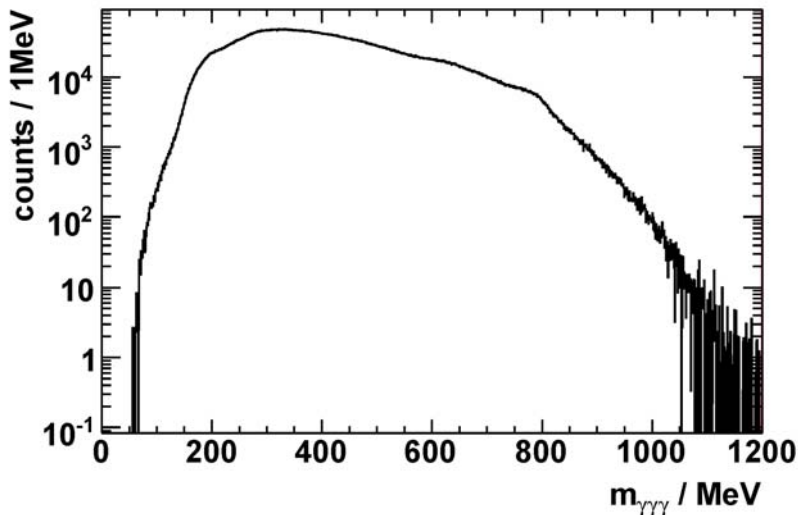
Figure 5.15: $\pi^0\gamma$ invariant mass spectrum for the carbon target after subtracting the random coincidences. The proton was not required.

Figure 5.15 shows the $\pi^0\gamma$ invariant mass spectrum after subtracting the random coincidences. Looking at the shape of the background, an enhancement around the η meson mass is visible. It can not be excluded, that this bump extends into the ω region and therefore would distort the observed ω meson lineshape. Thus, this background enhancement has to be removed.

The origin of this background contribution stems from the decay channel $\gamma p \to \pi^0\eta$, which has four photons in the final state and therefore should not contribute to the analysis branch we are looking at. Although the CB/TAPS detector system covers roughly the full solid angle of 4π, it can happen that one photon gets lost. Furthermore, two photon clusters may overlap so that only three out of four photon clusters are registered.

The background contribution was studied in Monte Carlo simulations of the $\gamma p \to \pi^0\eta p$ reaction ([Nan10a]). Figure 5.16(a) shows those events where only three photons from the four final state photons are detected. Combining two photons from an η decay and one photon from a π^0 decay, an almost vertical band can be seen at masses around 600 Mev on the x-axis. This leads to the bump seen in the $\pi^0\gamma$ invariant mass spectrum.
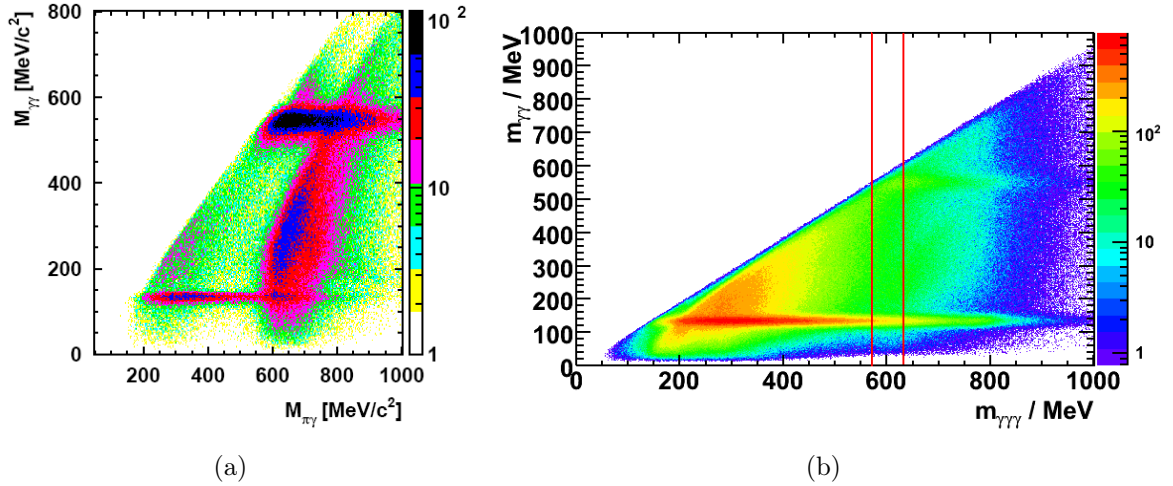
Figure 5.16: The invariant mass for all three $\gamma\gamma$ combinations is plotted versus the $\pi^0\gamma$ invariant mass. (a) Monte Carlo simulation for the reaction: $\gamma p \to \pi^0 \eta p$, where only three photons and a proton are detected. (b) Data, looking for the reaction $\gamma C \to X\pi^0\gamma p$.

To remove this background contribution at around 600 MeV the pion sideband subtraction technique has been applied. Therefore the two dimensional plot shown in figure 5.16 is projected on the $m_{\gamma\gamma}$ axis in the mass range $570 \leq m_{\pi^0\gamma} \leq 630$ MeV. In the projection the π^0 is well visible, sitting on top of a nonlinear background. Three areas are identified, one peak region and two sideband regions, as indicated in figure 5.17. The background is fitted and the yield in the two sidebands as well as the yield under the pion peak is determined. Afterwards the background counts in the sidebands are normalized to the background counts under the pion peak. The contribution from the two sidebands can be seen in figure 5.18(a). Here the full projection on the x-axis of figure 5.16(b) is shown together with the x-projections for the range $75 \leq m_{\gamma\gamma} \leq 110$ MeV (left sideband, blue) and $160 \leq m_{\gamma\gamma} \leq 195$ MeV (right sideband, green) Finally, the two normalized curves from the left and right sidebands are subtracted from the $\pi^0\gamma$ invariant mass spectrum over the full range. Figure 5.18(b) shows the comparison before and after the applied sideband subtraction technique.

5.5. Monte Carlo Simulation

Monte Carlo simulations can be used to determine the detector response and to analyse possible background contributions. The standard program to simulate the interactions
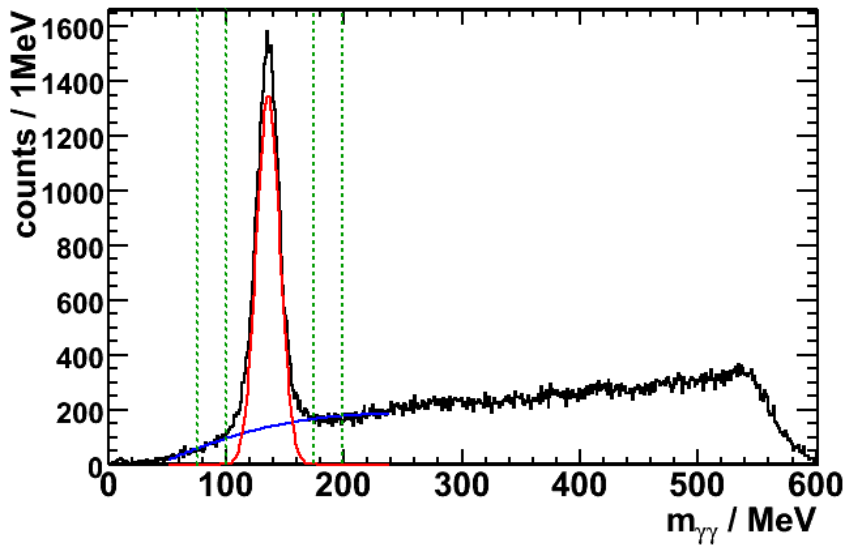
Figure 5.17: $\gamma\gamma$ invariant mass spectrum for the carbon target (y-projection of figure 5.16(b)). In blue the fit to the background and in red the π^0 peak content is shown, the dashed green lines indicate the two sideband regions.

(a)   (b)
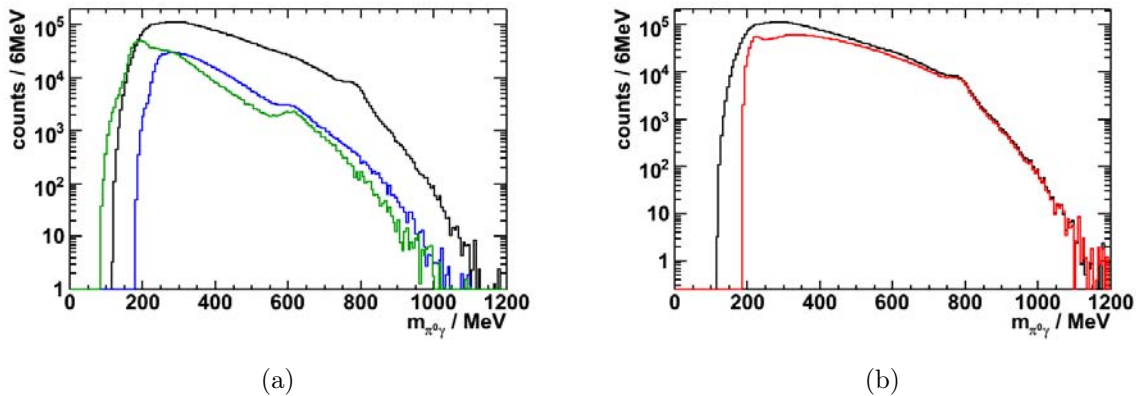
Figure 5.18: (a) $\pi^0\gamma$ invariant mass spectrum for the carbon target in black (full x-projection of figure 5.16(b)). The left and right sidebands are shown in blue and green, respectively. (b) $\pi^0\gamma$ invariant mass spectrum for the carbon target before the pion sideband subtraction (black) and after the pion sideband subtraction (red).

of mid and high energetic particles is the GEANT[1] package [Ago03].
First of all, the events of interest have to be generated. Therefore an event generator is

---

[1]**GE**ometry **AN**d **T**racking

needed. In this generator the incident photon energy is given by a $1/E_\gamma$ distribution in the energy range 800 to 1400 MeV. To allow also for reactions below the ω production threshold $E_{\gamma,thresh} = 1108$ MeV Fermi motion was implemented for the solid targets. This smeares the momentum of the nucleon by the distribution function shown in figure 5.19.
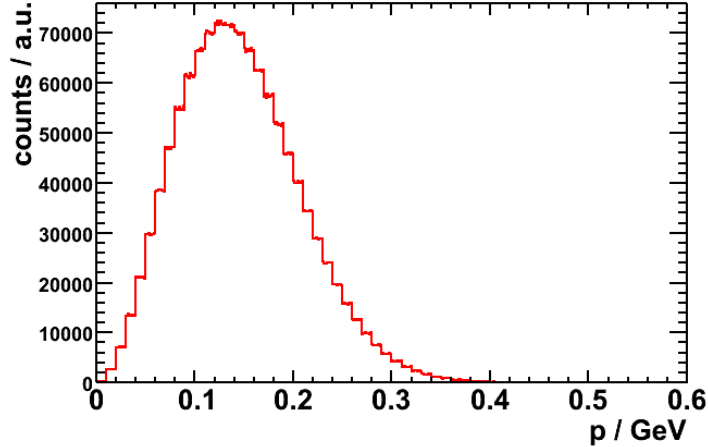
Figure 5.19: Fermi momentum distribution function used for the carbon target.

For the production and decay of particles the event generator uses the GDECA classes of GEANT. This three body kinematic routine calculates the four momenta of the reaction products.

For this thesis, the following reactions have been simulated:

$$\gamma p \rightarrow \omega p \rightarrow \pi^0 \gamma p \tag{5.8}$$

$$\gamma p \rightarrow \pi^0 \pi^0 p \tag{5.9}$$

For the reaction in equation 5.8 simulations were performed for a liquid hydrogen and a carbon target. The length for the liquid hydrogen target was chosen to be 5 cm (as the one used in the experiment), 15 mm and 1 mm, to study the impact of an extended target. The result is shown in figure 5.20.

The simulations for the carbon target were performed with 15 mm length, the same as used in the experiment. Here, the Fermi momentum was included.

Thus, the background is dominated by contributions from $\pi^0 \pi^0$ decays, this channel was also investigated in simulations using the carbon target.

The values provided from the event generator after executing the GDECA classes are angles and the four momenta of the particles in the center of mass system. They have
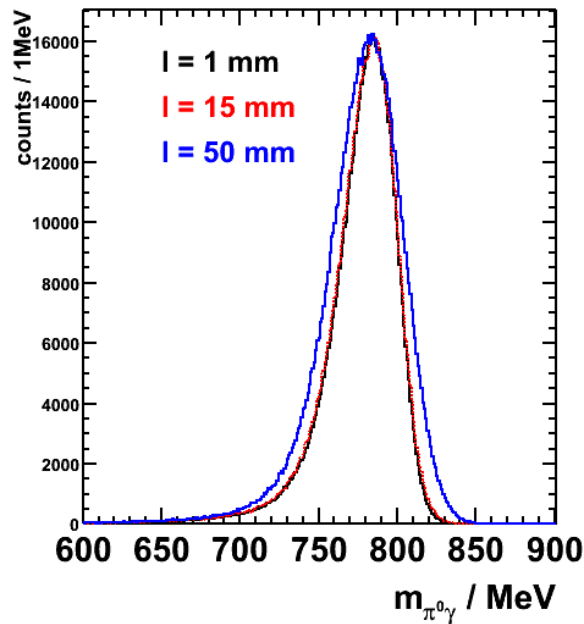
Figure 5.20: The impact on the target thickness to the invariant mass. The reconstructed widths are 22.0 MeV (blue line), 17.1 MeV (red line) and 16.7 MeV (black line) for the three thicknesses 50 mm, 15 mm and 1 mm, respectively.

to be transformed into the laboratory systems before they can be feed into GEANT. GEANT now calculates all interactions of the generated particles with the detector material. Therefore the whole detector geometry has to be implemented into GEANT as shown in figure 5.21. The different detector components CB, MWPC, PID, TAPS and TOF bars can be included in the detector setup file, depending on the used experimental setup. In our case only CB, PID and TAPS are implemented in the simulation.

5.6. Determination of ω Lineshape

The extraction of the ω meson lineshape is very sensitive to the determination of the background. Therefore two different methods have been used in this thesis.
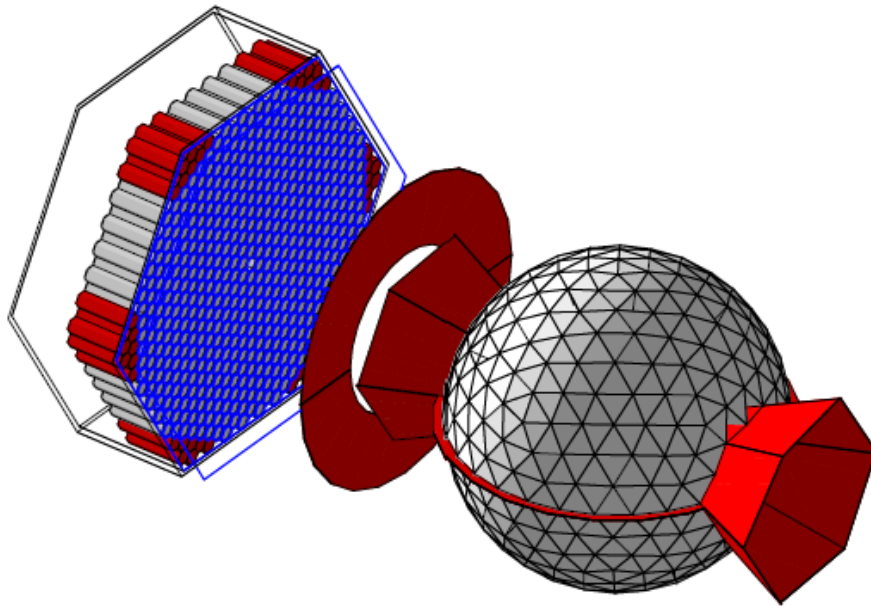
Figure 5.21: Detector geometry of the Crystal Ball and TAPS setup in Mainz implemented in GEANT4.

5.6.1. Background Determination by a Fit

The background contribution is determined by a fit and afterwards subtracted from the whole $\pi^0\gamma$ invariant mass spectrum. The background is parametrized as:

$$B(x) = exp\left(p_0 + p_1 \cdot x + p_2 \cdot x^2 + p_3 \cdot x^3\right) \tag{5.10}$$

Figure 5.22(a) shows the $\pi^0\gamma$ invariant mass spectrum for the exclusive analysis of the carbon data. The fit to the data is shown in blue, the dashed blue line corresponds to the background fit. To classify the quality of the fit the ratio $\frac{signal}{fit}$ is made, shown in figure 5.22(b). Varying the range of the fit, the deviations from one on the right and left side of the peak in the ratio plot are kept as small as possible. The average deviation from 1 in the mass range 350 MeV to 700 MeV is in the order of 1%.

5.6.2. Background Determination from the Data

An alternative method to determine the background contribution was investigated by M. Nanova [Nan10a]. The main background contributions come from the reactions
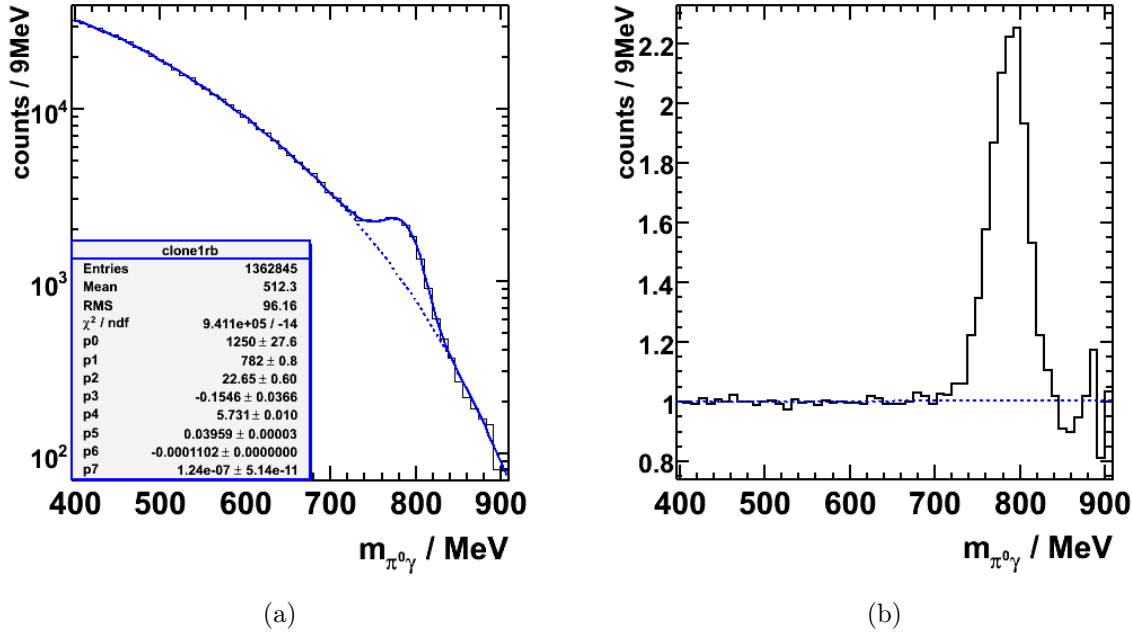
Figure 5.22: (a) $\pi^0\gamma$ invariant mass spectrum for the carbon data in the exclusive analysis. In blue (dashed line) the fit to the background is shown. (b) Ratio of the $\pi^0\gamma$ spectrum to the background fit.

$\gamma A \to (A-1)p\pi^0\pi^0$ and $\gamma A \to (A-1)p\pi^0\eta$ where four photons are in the final state. It can happen that only three of the photons are registered due to detector inefficiencies or photon cluster overlap.

To reproduce the background directly from the data four photon events are selected and one of them is randomly omitted. The same cuts (prompt timing, $T_{\pi^0} > 150$ MeV, pion sideband subtraction) as for the three photon analysis are applied. The signal from the three photon analysis is compared to the background from the four photon analysis in figure 5.23(a). Signal and background are different in slope and magnitude due to different kinematics. Therefore the probability to detect m photons in an event with M photons can be calculated:

$$P_m^M = \left(\begin{array}{c} M \\ m \end{array} \right) \cdot (1 - \Omega)^{M-m} \cdot \Omega^m \tag{5.11}$$

with the detection efficiency Ω for one photon. In table 5.3 the calculated probabilities for different detection efficiencies are listed.

The energy dependence of the probability to register only three out of the four photons is studied in simulations of the main background contribution $\gamma p \to \pi^0\pi^0 p$, shown in figure 5.23(b). The red curve corresponds to the detection of three photons, while the

(a)   (b)
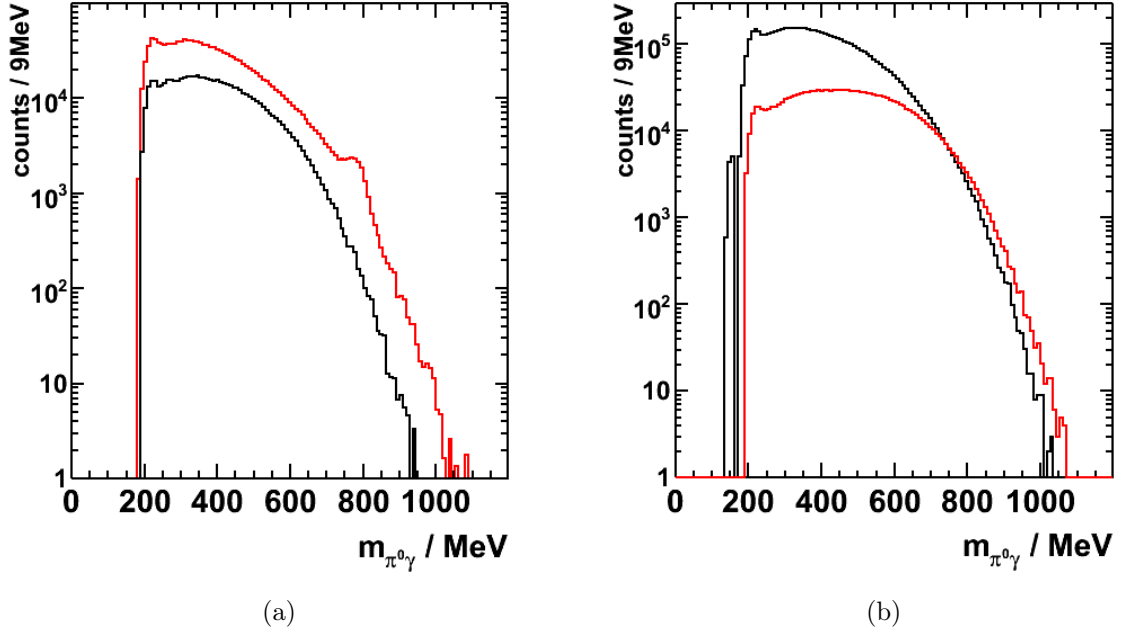
Figure 5.23: (a) **Data:** Signal spectrum (red) from events with three photons and one proton and background spectrum from events with four photons and one proton with randomly omitting one photon for the carbon target. (b) **Simulation:** Events with three photons and one proton detected (red) and events with four photons and one proton detected (black) from the reaction $\gamma p \rightarrow p\pi^0\pi^0$.

Ω	M = 3	M = 4	
	m = 3	m = 3	m = 4
0.5	0.13	0.25	0.06
0.6	0.22	0.35	0.13
0.75	0.42	0.42	0.32
0.8	0.51	0.41	0.41
0.85	0.61	0.36	0.52
0.9	0.73	0.29	0.66

Table 5.3: Photon detection probability.

black curve correponds to four detected photons where one of them is omitted randomly in the analysis. Looking at the ratio of both curves, one sees that the probability to detect only three out of four photons depends on the energy (see figure 5.24(a)).

In a light nucleus like carbon, strong in-medium effects are not expected. Therefore

one can use the ratio $\frac{\text{signal}}{\text{background}}$ in figure 5.24(b) to correct the background slope in the niobium spectrum. The correction function (in blue) is obtained by fitting the ratio, excluding the peak region between 740 MeV and 820 MeV. It is not possible to fit the energy range from 400 MeV to 950 MeV with one function. Therefore the ranges 400 MeV to 700 MeV and 600 MeV to 950 MeV are fitted seperately and than combined to one function to correct the niobium background.

Comparing the ratio obtained from simulations to the ratio of the signal to the background events for the carbon data a difference in slope is visible. Therefore the two π^0 channel seems to be the dominante contribution to the background, but not the only contribution.

(a)   (b)
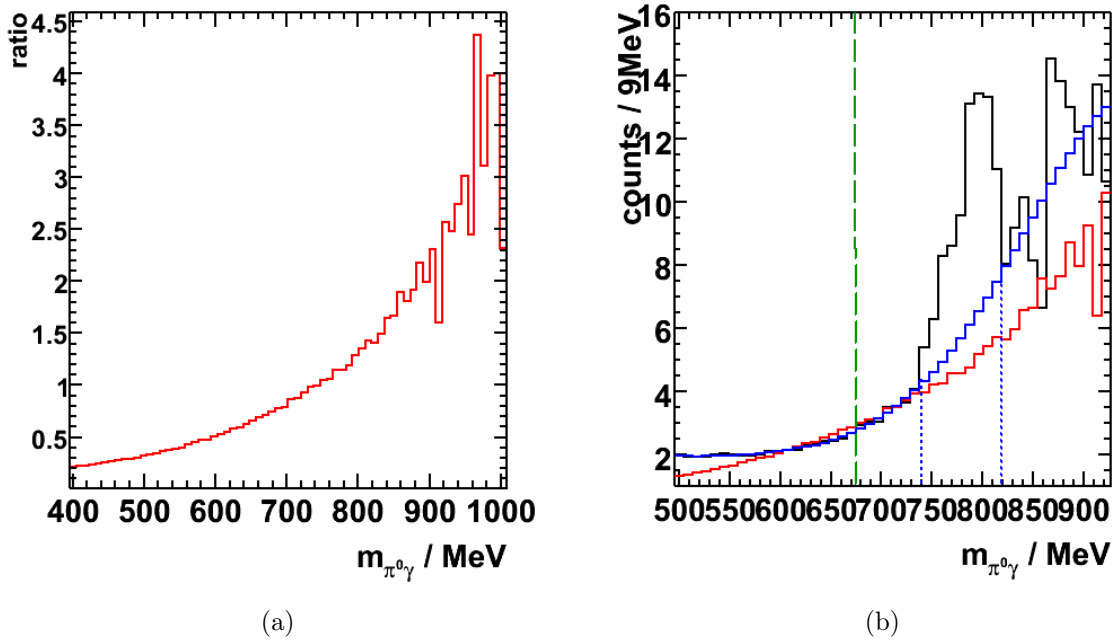
Figure 5.24: (a) **Simulation:** Ratio of the $3\gamma + 1p$ events to the $4\gamma + 1p$ events. (b) **Data:** Ratio of the $3\gamma + 1p$ events to the $4\gamma + 1p$ events for the carbon target. The ratio is fitted excluding the range 740 MeV to 820 MeV (dashed blue lines). The dashed green line indicates the border changing from the one fit to the other fit in the correction function shown in blue.

In figure 5.25(a) the signal from the three photon exclusive analysis is compared to the background from the four photon exclusive analysis for the niobium data. The obtained correction function from the carbon ratio is now multiplied with the Nb background to change its slope. To determine the height of the background, the number of counts in the signal and background spectrum are requested to be the same

in the mass range 600 MeV to 900 MeV, excluding the peak region. Figure 5.25(b) shows the signal together with the corrected and normalized background. To extract

(a)

(b)
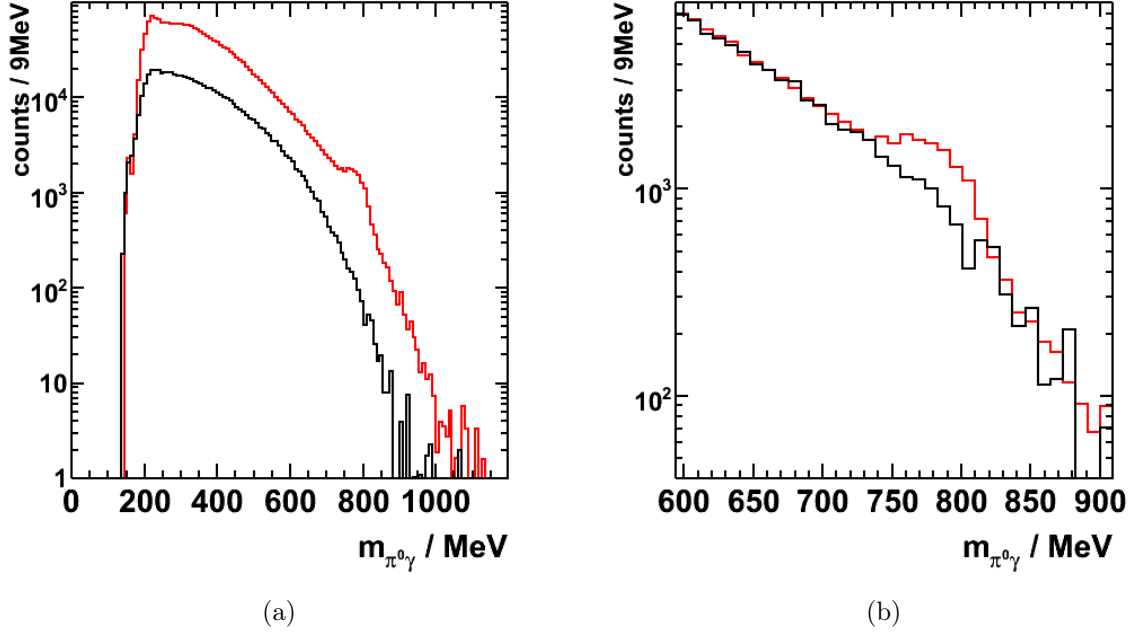
Figure 5.25: *Exclusive analysis:* (a) In red the $\pi^0\gamma$ invariant mass spectrum from events with three photons and one proton is shown. In black the background spectrum from events with four photons and one proton is shown. Both spectra are for the niobium target. (b) The corrected and normalized background in black together with the signal spectrum in red.

the lineshape of the ω signal, a first attempt was to subtract the background spectrum directly from the data. Unfortunately, the statistics at the higher masses is too poor; fluctuations are too large in the ratio as well as in the background subtracted signal spectrum. To avoid these large fluctuations, the background was fitted as it is illustrated in figure 5.26 (upper left panel). At the higher masses the situation improves, but at lower masses the direct subtraction of the background works much better. Again, a combination of data and fit was applied, shown in figure 5.26 (upper right panel).

To check the quality, the ratio of the signal spectrum to the combined background decription is determined, see figure 5.26 (lower left panel). Here the average deviation from 1 in the mass range from 350 MeV to 700 MeV is 3.5%.

Finally, the combined background description is subtracted from the signal spectrum (figure 5.26 (lower right panel)).
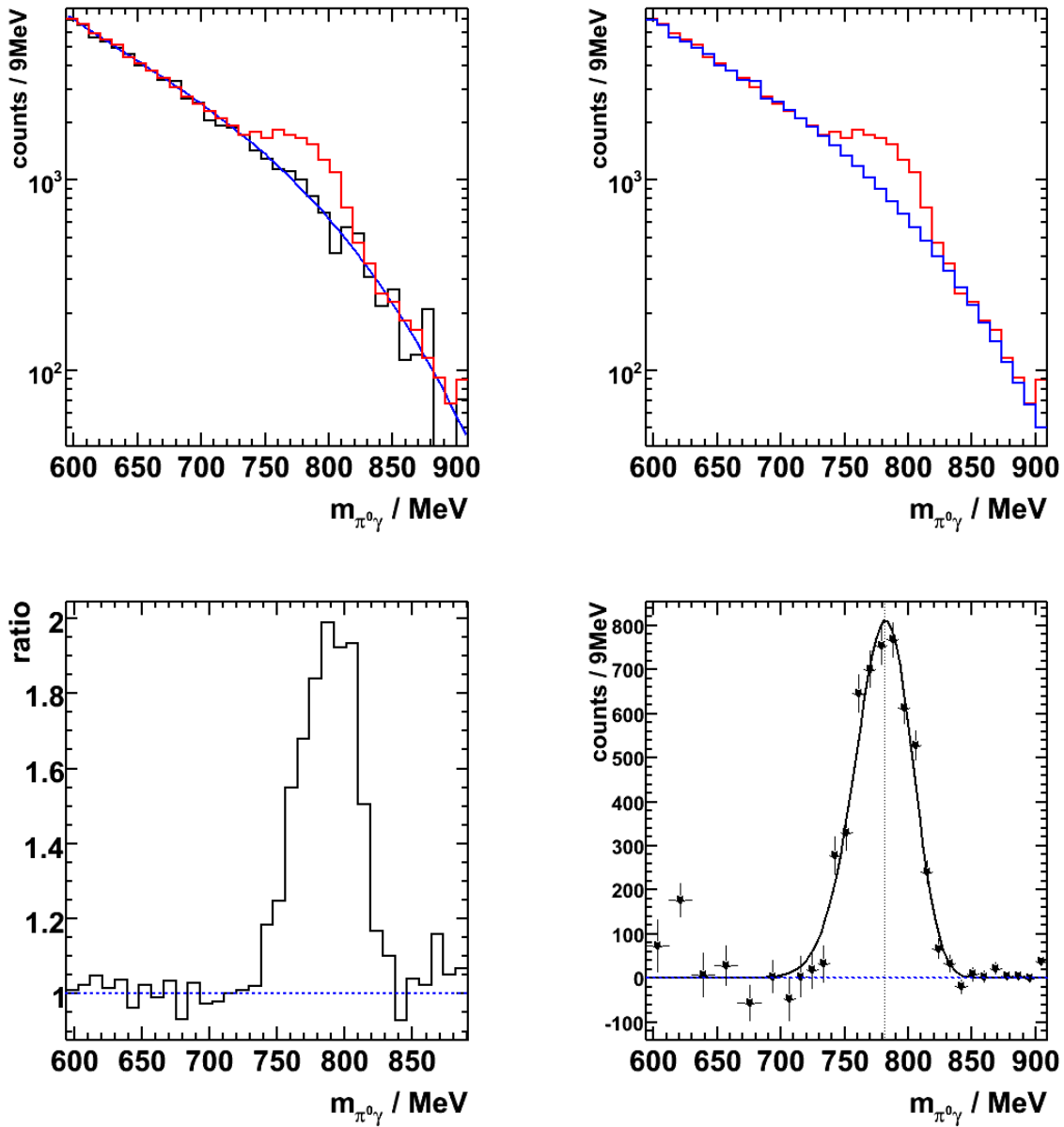
Figure 5.26: ***Exclusive analysis:*** *Upper left:* The signal (red) and background spectrum (black). In blue the fit to the background is shown. *Upper right:* The background spectrum parametrized by the data at lower masses and by the fit at higher masses (blue). In red the $\pi^0\gamma$ signal spectrum for niobium. *Lower left:* Ratio of the $\pi^0\gamma$ spectrum to the background spectrum from figure 5.26(b). *Lower right:* $\pi^0\gamma$ invariant mass spectrum after background subtraction.

5.7. Momentum Analysis

For the momentum analysis the ω yield is determined in different momentum bins, each of them 50 MeV wide. Here only the semi-exclusive analysis is performed to have sufficient statistics in the different momentum bins. Exactly the same cuts as for the lineshape analysis are applied.

The ω yield in each momentum bin is determined using the fit method described in chapter 5.6.1. The fit range is fixed to 350 to 940 MeV. After fitting all the momentum bins, a larger deviation in the fit parameters σ and d (the tailing parameter) is seen. Figure 5.27 shows these parameters as a function of the momentum for the carbon data, figure 5.28 for the niobium data. A fit through the points is applied and the corresponding values are now used in the Novosibirsk fit routine as fixed parameters for each bin. The obtained counts from the fit have to be corrected with the detector
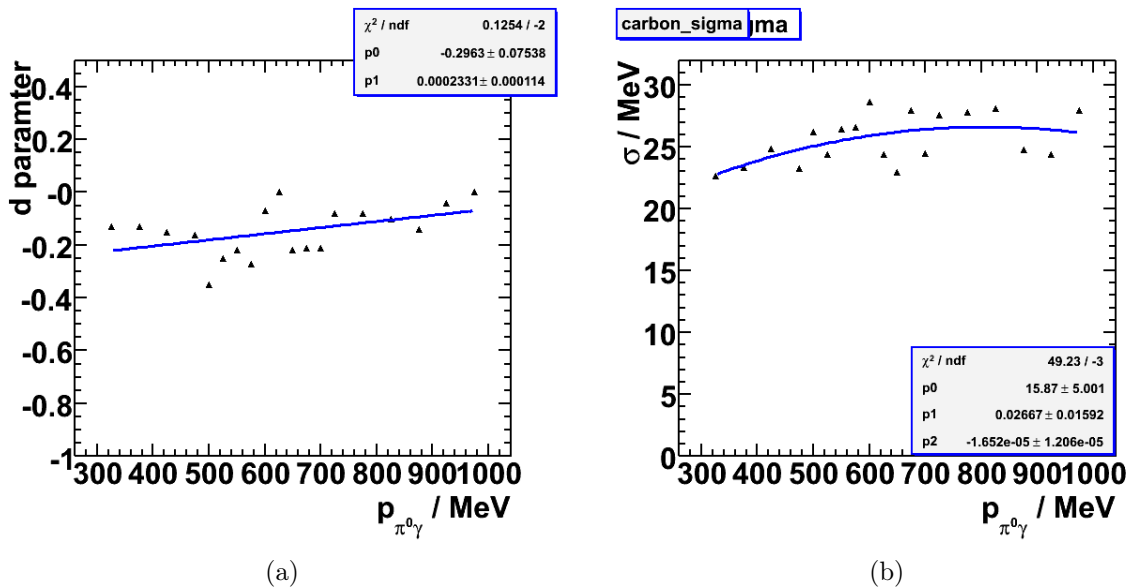
Figure 5.27: Carbon data: (a) Tailing parameter d of the fit for the different momentum bins. (b) The width σ of the fit for the different momentum bins.

acceptance. Therefore the reaction $\gamma p \rightarrow \omega p \rightarrow \pi^0 \gamma$ was simulated. The corresponding start distribution is shown in figure 5.29(a). To determine the acceptance of the detector system, one has to divide the distribution of reconstructed events by the start distribution. Since, the momentum analysis is performed semi-exclusive, the proton is not required. The reconstructed events are shown in figure 5.29(a), taken only the invariant mass range $m_\omega \pm 3\sigma$ into account. The resulting detector acceptance can be seen in figure 5.29(b).

Finally, the data points have to be divided by the detector acceptance before they can
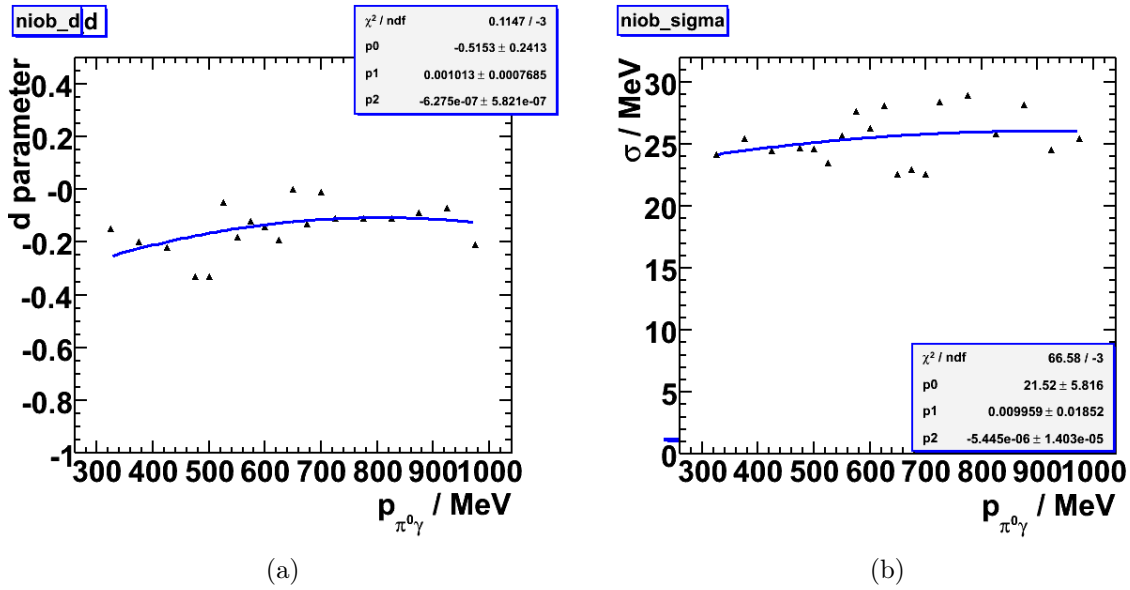
Figure 5.28: Niobium data: (a) Tailing parameter d of the fit for the different momentum bins. (b) The width σ of the fit for the different momentum bins.

be compared to the theoretical predictions. The errors are deduced by the equation

$$e = \sqrt{S + 2 \cdot B} \tag{5.12}$$

where S belongs to the counts in the peak and B are the counts in the background, both determined in $\pm 3\sigma$ of the peak value.

(a)   (b)
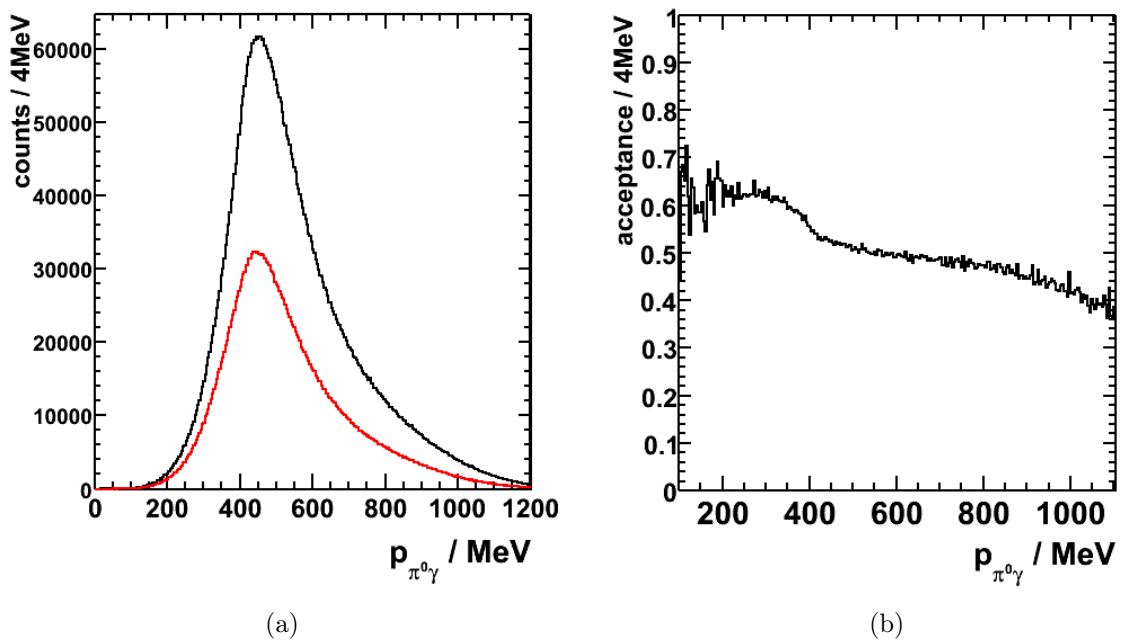
Figure 5.29: (a) **Simulation:** Start distribution (black) and distribution of reconstructed events from the reaction $\gamma p \rightarrow \omega p \rightarrow \pi^0 \gamma$. The proton was not required. (b) **Simulation:** Detector acceptance.

Chapter 6.

Results

In this chapter the results obtained in this thesis are presented. The lineshapes of the $\pi^0\gamma$ invariant mass spectra are compared for the two target materials carbon and niobium. In addition the lineshapes are compared to a reference signal, obtained from a liquid hydrogen measurement which defines vacuum properties. This data was taken in 2006/2007 and calibrated from H. Berghäuser within his PhD work.
In addition the results obtained in the exclusive and semi-exclusive analysis are compared to theoretical predictions.

As a second possiblity to achieve informations of the properties of the ω meson in a nuclear medium, the momentum distribution of the ω meson was investigated. The results for the carbon and niobium target are also compared to GiBUU transport code calculations.

Finally the thesis is closed with conclusions and an outlook.

6.1. Exclusive Lineshape Analysis

For the exclusive analysis all particles in the final state of the reaction

$$\gamma A \rightarrow (A-1)\omega p \rightarrow (A-1)\pi^0 \gamma p \rightarrow (A-1)\gamma\gamma\gamma p \qquad (6.1)$$

are detected. Figure 6.1(a) shows the invariant mass spectrum for the three beamtimes: liquid hydrogen, carbon and niobium. Already here it is visible, that the lineshape of the liquid hydron spectrum differs from the other two. Going to higher masses the spectrum falls off more steeply which makes it more difficult to fit the background contribution.
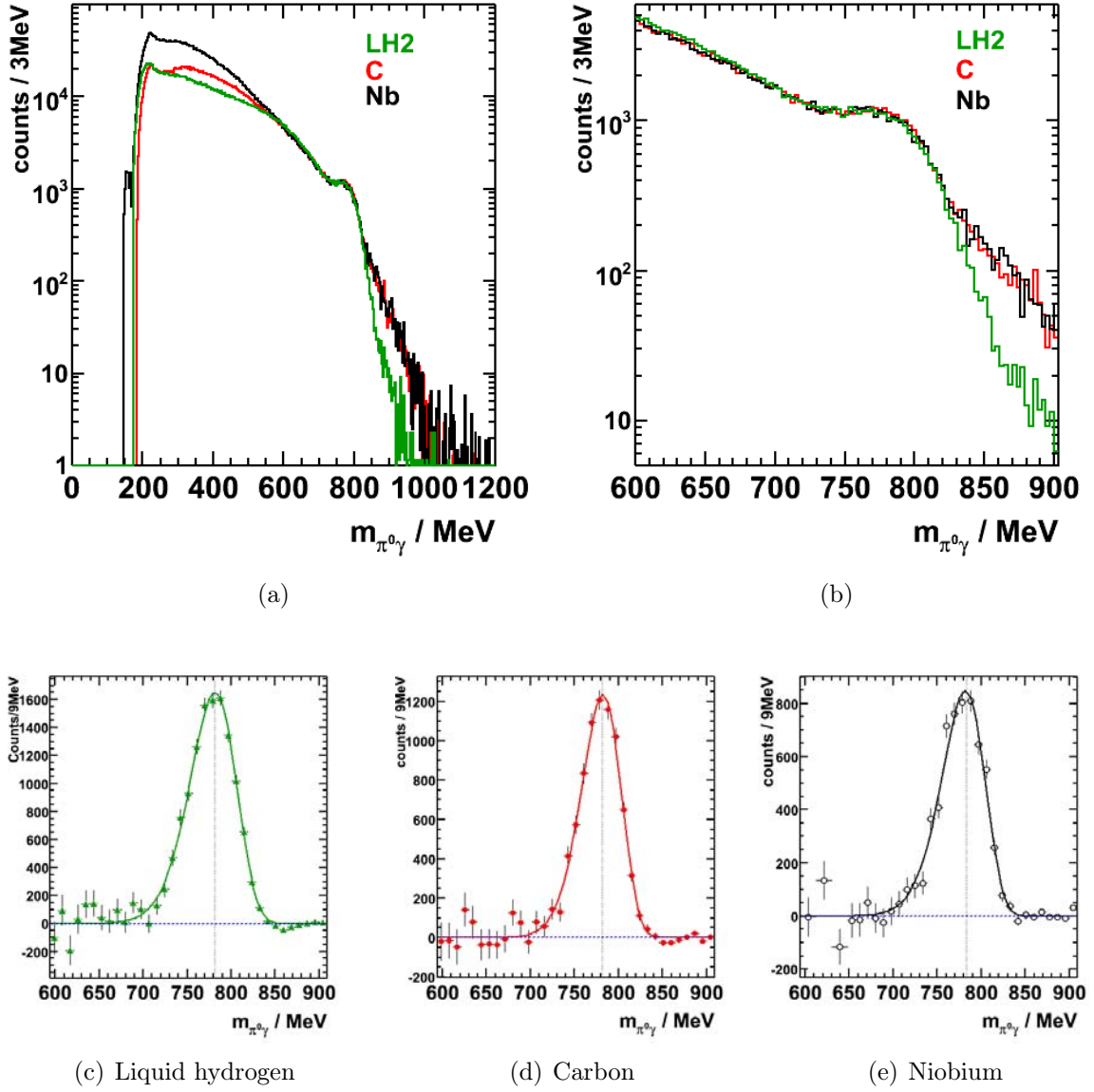
Figure 6.1: *Exclusive analysis, background determined by the fit method.*
(a) The whole $\pi^0\gamma$ invariant mass spectrum for the three different beamtimes: liquid hydrogen (green), carbon (red) and niobium (black). **(b)** The same spectrum, but now zoomed in the range 600 MeV to 900 MeV. **(c) - (e)** $\pi^0\gamma$ invariant mass spectrum obtained after background subtraction for the three different targets.

Having a closer look into the peak region (Figure 6.1(b)), one sees that the ω peak in the liquid hydrogen data is broader compared to the peaks in the carbon and niobium data which can be attributed to the extended size of the LH_2 target.

Figure 6.1(c) - (e) shows the obtained lineshape for the three different target materials after the background is subtracted. For these plots the background contribution was determined by a fit with the Novosibirsk function. The obtained fit parameters are listed in table 6.1. A comparison of the parameters shows that they are comparable within the erros.

As a next step, the invariant mass spectra are now compared with each other.

	Peak Position [MeV]	σ [MeV]	Tailing Parameter d
liquid hydrogen (5 cm)	781.5	26.6 ± 0.6	-0.17 ± 0.02
carbon	782.0	22.7 ± 0.6	-0.15 ± 0.04
niobium	781.7	24.7 ± 0.8	-0.18 ± 0.04

Table 6.1: ***Exclusive analysis***. Fit parameters of the Novosibirsk function for the different target materials. The d parameter is a measure how pronounced the tailing to lower masses is.

6.1.1. Comparison of different Targets

For a comparison of the different targets, the background contribution was determined by a fit and afterwards subtracted.

Starting with a comparison of the carbon data to the reference signal liquid hydrogen as it is shown in figure 6.2 (upper right panel). Naively, one would expect the liquid hydrogen signal to be narrower than the signal from the carbon target. But it has to be taken into account, that the liquid hydrogen target is an extended target with 5 cm length. The thickness of the nuclear targets was chosen, to correspond to approximately 10% of their radiation length. Therefore the lengths for the carbon and niobium target were 1.5 cm and 0.1 cm, respectively. According to simulations presented in chapter 5.5 the length of the target influences the width of the signal. Going from 5 cm to 1.5 cm and 0.1 cm the resolution decreases from $\sigma = 22.0$ MeV to $\sigma = 17.1$ MeV and $\sigma = 16.7$ MeV, respectively. The resolution changes by roughly 20%. For a final comparison of both data sets this effect has to be taken into account. Figure 6.2 (upper left panel) shows the liquid hydrogen data with a 20% reduced width together with the carbon data.

In figure 6.2 (lower left panel) the comparison of niobium and liquid hydrogen is shown. Again the effect of the extended target on the width of the signal has to be taken into account. The liquid hydrogen lineshape corresponding to a target thickness of 0.1 cm is shown in the lower right panel of figure 6.2.
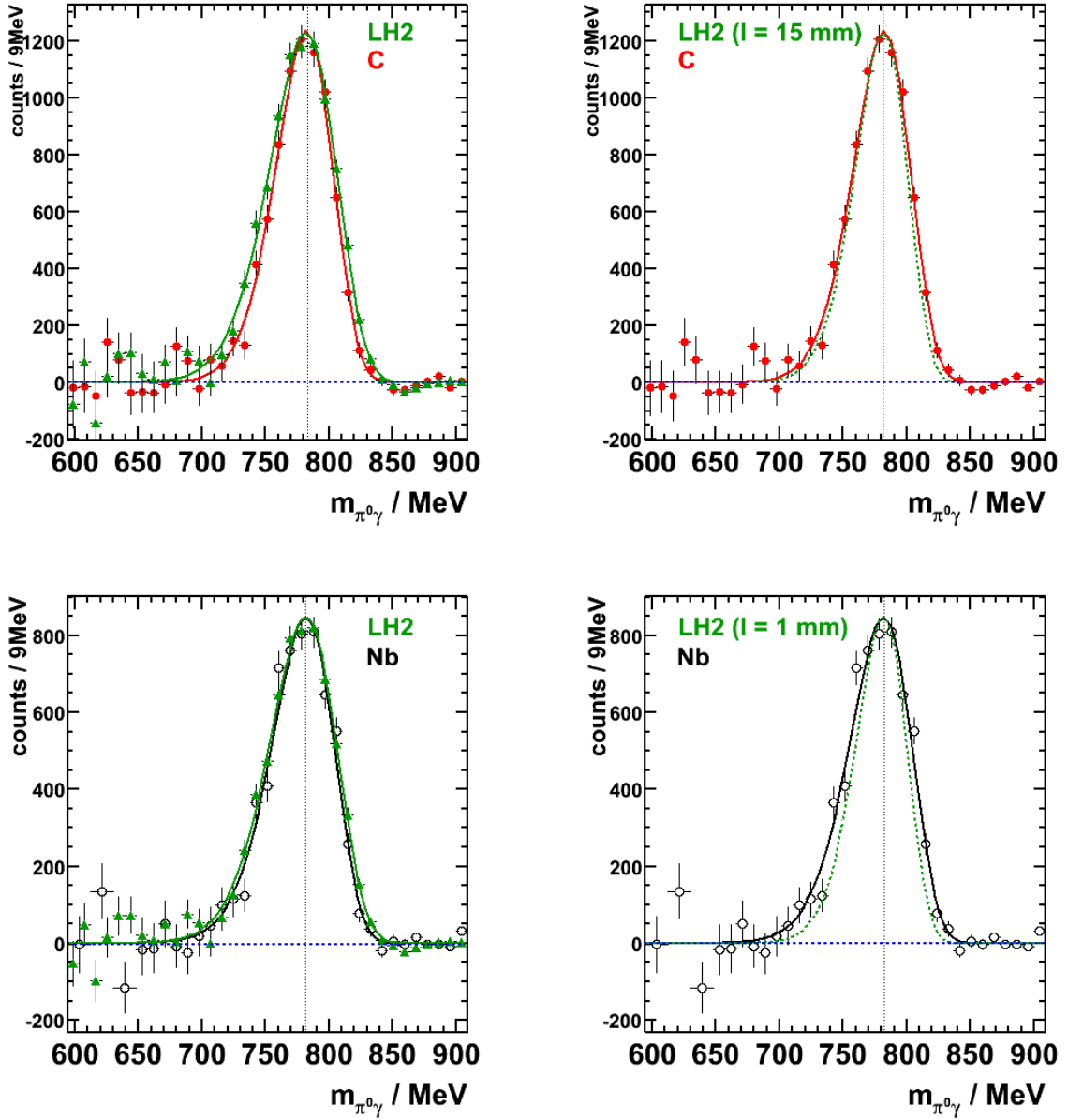
Figure 6.2: *Exclusive analysis, background determined by the fit method.*
Upper left: The carbon data in red is compared to liquid hydrogen data in green.
Upper right: The carbon data compared to a liquid hydrogen signal with a reduced
width corresponding to a target thickness of 1.5 cm. *Lower left:* The niobium data
in black is compared to liquid hydrogen data in green. *Lower right:* The niobium
data compared to a liquid hydrogen signal with a reduced width, corresponding to
a target thickness of 0.1 cm.

Finally, all lineshapes can be plotted toghether, as it is shown in figure 6.3(a). All three curves are so close together that within the errors no deviation can be seen when comparing the signal of the nuclear targets to the reference signal.

(a)　　　　　　　　　　　　　(b)
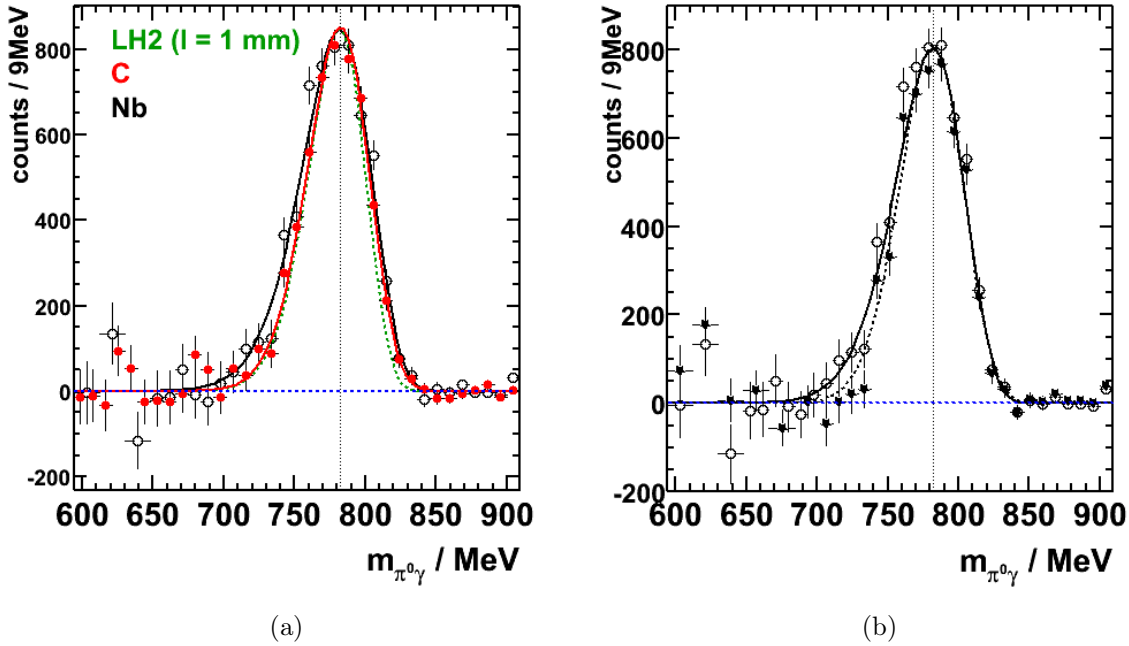
Figure 6.3: *Exclusive analysis.* **(a)** $\pi^0\gamma$ invariant mass spectrum for niobium (black) in comparison to the carbon data (red) and to the lineshape for a 1 mm thick liquid hydrogen target (green). The background was determined by the fit method. **(b)** Comparison of the niobium data with the two different background determination methods: fit method (open circles) and from the data (black stars).

In case of the niobium target, the background was in addition determind directly from the data. Since in the carbon data no strong in-medium effects are expected, its ratio of the $\pi^0\gamma$ spectrum to the background spectrum obtained from four photons is used to correct the background of the niobium data.

In figure 6.3(b) the comparison of the two niobium analyses is shown. Already here it is visible how sensitive the lineshape of the signal to the background determination is. Within the errors both curves agree, but in the important low mass regime deviations are visible.

6.2. Semi-Exclusive Lineshape Analysis

In the semi-exclusive analysis the statistics is much higher compared to the exclusive analysis. Here the hope is, that the data is that precise to exclude at least some of the theoretically predicted scenarios.

Figure 6.4(a), (b) show the comparison of the three beamtimes. Also for the semi-exclusive analysis, the background contribution was first determined by a fit with the Novosibirsk function. In figure 6.4(c) - (e) the $\pi^0\gamma$ invariant mass spectrum for the different target materials after the background subtraction are shown. The obtained fit parameters are listed in table 6.2.

	Peak Position [MeV]	σ [MeV]	Tailing Parameter d
liquid hydrogen (5 cm)	784.5	27.7 ± 0.5	-0.01 ± 0.02
carbon	782.1	23.3 ± 0.4	-0.15 ± 0.02
niobium	782.0	22.8 ± 0.4	-0.14 ± 0.02

Table 6.2: *Semi-exclusive analysis*. Fit parameters of the Novosibirsk function for the different target materials. The d parameter is a measure how pronounced the tailing to lower masses is.

6.2.1. Comparison of different Targets

Now the lineshapes for the different target materials were compared. At first, the carbon data is shown together with liquid hydrogen data in figure 6.5 (upper left panel). Due to the extended size of the liquid hydrogen target the signal is much broader. In figure 6.5 (upper right panel) the same target length for the carbon and liquid hydrogen data was assumed.

The niobium data is compared to liquid hydrogen with 5 cm target thickness (figure 6.5 (lower left panel)) and 0.1 cm target thickness (figure 6.5 (lower right panel)). Finally, all invariant mass spectra for the three different targets were plotted together, as it is shown in figure 6.6(a). Here the fit to the lineshapes of the carbon and niobium are even so close, that they hardly can be distinguished. Figure 6.6(b) shows the two results for the niobium data: the open rectangles correspond to the fit method while the black stars correspond to the background determination from the data. Again the systematic uncertainties are visible.

(a)

(b)

(c)

(d)

(e)
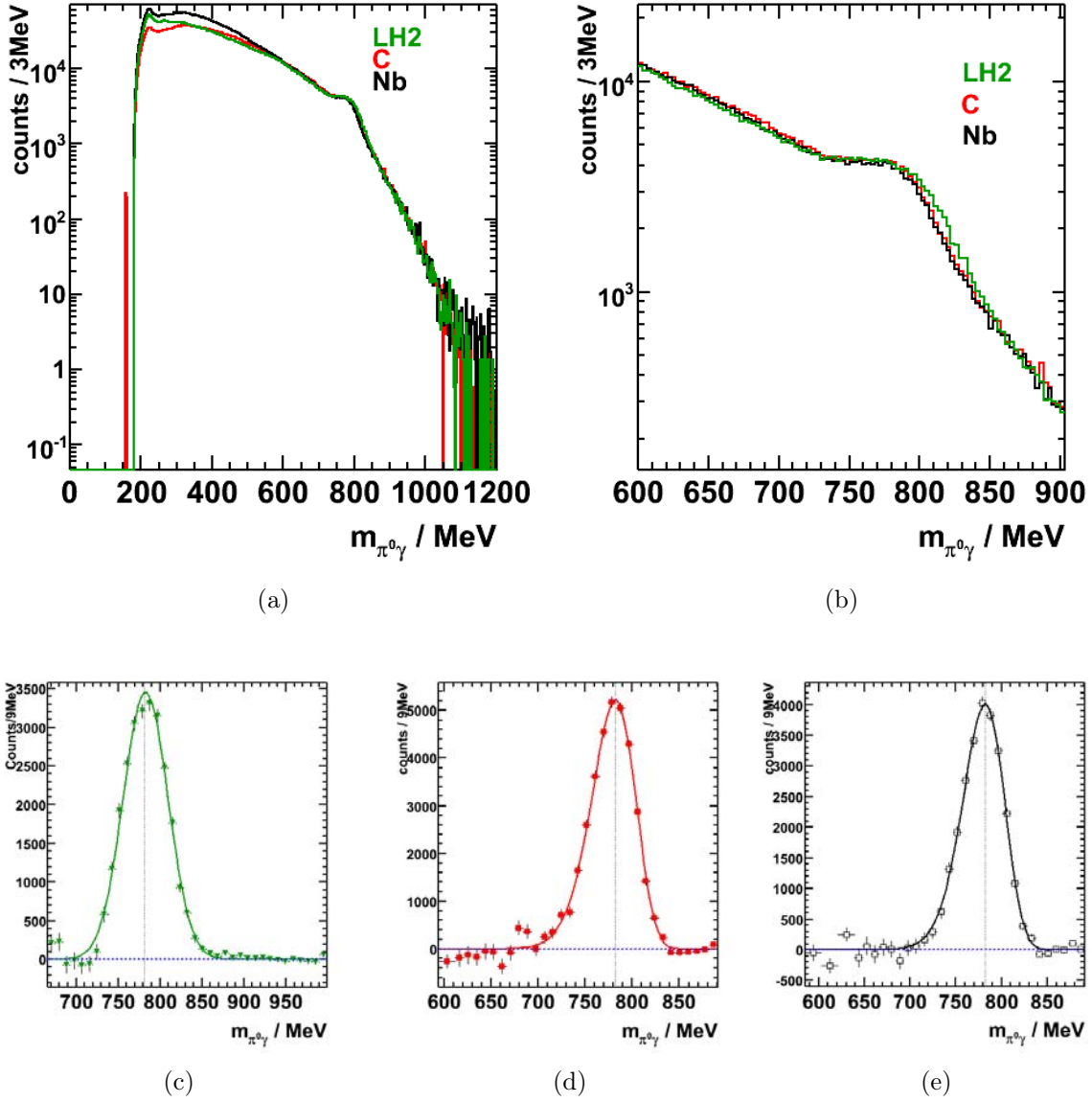
Figure 6.4: *Semi-exclusive analysis, background determined by the fit method.* **(a)** The whole $\pi^0\gamma$ invariant mass spectrum for the three different beamtimes: liquid hydrogen (green), carbon (red) and niobium (black). **(b)** The same spectrum, but now plotted in the range 600 MeV to 900 MeV. **(c) - (e)** $\pi^0\gamma$ invariant mass spectrum obtained after background subtraction for the three different targets.

121
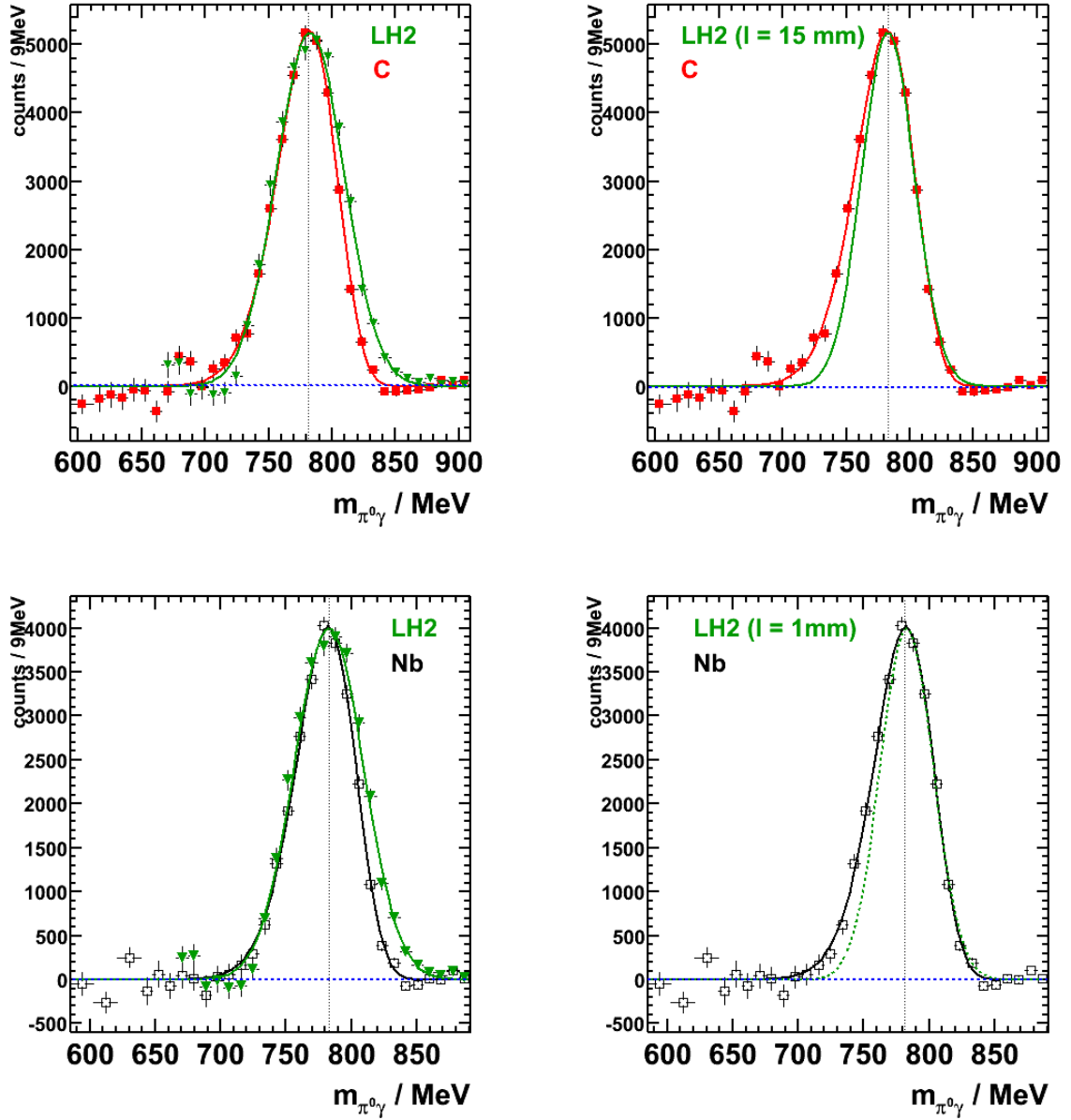
Figure 6.5: *Semi-exclusive analysis, background determined by the fit method.* *Upper left:* The carbon data in red is compared to liquid hydrogen data in green. *Upper right:* The carbon data compared to an ω signal from liquid hydrogen with a reduced width, corresponding to a target thickness of 1.5 cm. *Lower left:* The niobium data in black is compared to liquid hydrogen data in green. *Lower right:* The niobium data compared to a liquid hydrogen signal with a reduced width, corresponding to a target thickness of 0.1 cm.
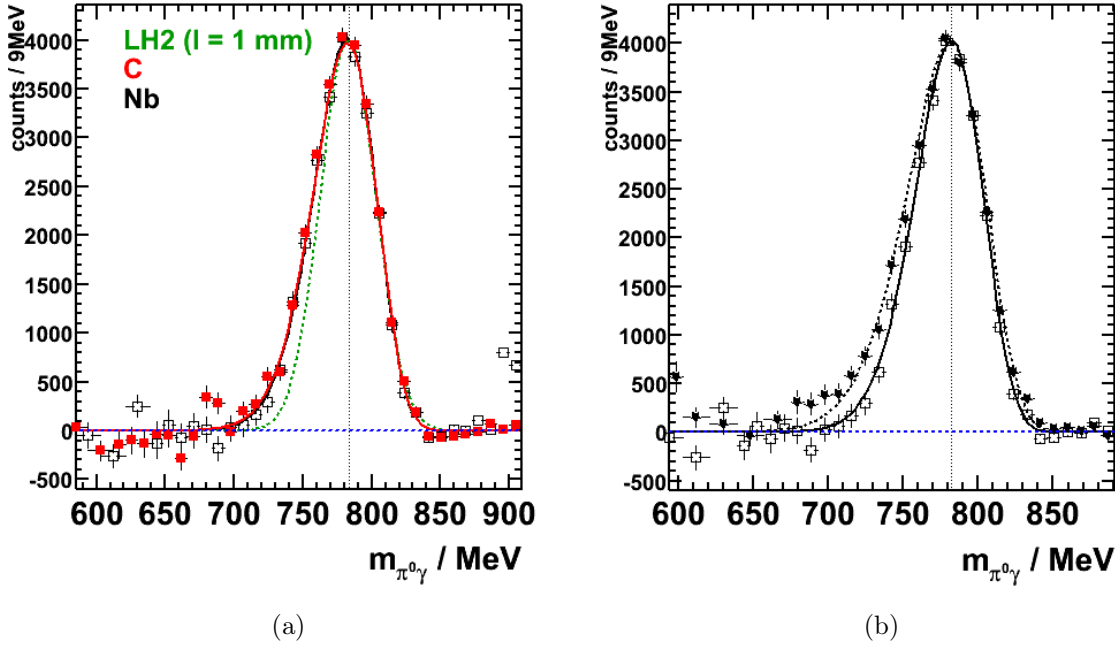
Figure 6.6: *Semi-exclusive analysis.* **(a)** $\pi^0\gamma$ invariant mass spectrum for niobium (black) in comparison to the carbon data (red) and to the lineshape for a 1mm thick liquid hydrogen target (green). **(b)** Comparison of both niobum analyses: $\pi^0\gamma$ invariant mass spectrum, background determined by a fit in the open rectangles, background determined from the data in the black stars.

6.3. Comparison to GiBUU Calculations

The motivation to perform the experiments for this thesis where BUU transport code calculations, predicting a measurable change of the ω meson lineshape in a nuclear medium, see figure 6.7(a). If the lineshape is affected by in-medium effects, one should see a difference comparing the $\pi^0\gamma$ invariant mass distribution for different target materials. This comparison of the lineshape for different target materials (light (carbon) and heavy (niobium) nuclei) presented in the last sections shows no significant difference.

Therefore the data is now compared to the theoretical predictions. Here, the transport code was further improved, which leads to a change in the predicted lineshapes. Whereas the old predictions showed a pronounced tail towards lower masses (figure 6.7(a)) the new theoretical calculations show no significant enhancement at the lower masses. As it is shown in figure 6.7(b) the differences between the three scenarios (no modification, collisional broadening and collisional broadening plus an attractive mass shift) are small. Only the scenario where a mass shift alone without broadening

is taken into account has a stronger tailing at lower masses.

(a)   (b)
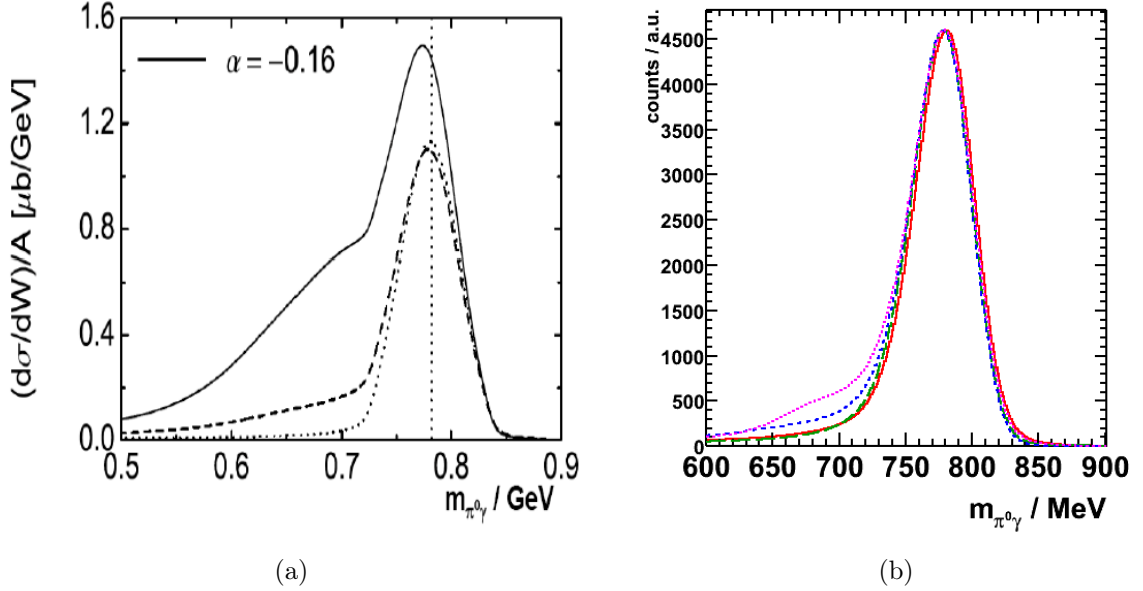
Figure 6.7: **(a)** Motivation for the studies of the ω meson lineshape for production in the near threshold regime. The theoretical predictions for collisional broadening (solid line) and collisional broadening plus mass shift (dashed line) are compared to the vacuum spectral function (dotted line). **(b)** More recent GiBUU transport code calculations for the ω lineshape in vacuum (solid red line), collisional broadening (dashed green line), collisional broadening and mass shift (dashed blue line) and shift only (magenta dotted line).

The comparison of the measured ω meson lineshape for the exclusive analyses to the latest theoretical predictions are shown in figure 6.8 (upper left panel). The open circles correspond to the data where the background was determined by a fit, for the black stars the background was determined from the data. This plot shows the systematic uncertainties for the lineshape determination, because of the strong sensitivity to the background determination.

The lineshape obtained by the fitting method describes the predicted curves within the error bars while the niobium data where the background was determined from the data undershoots the theoretical predictions at lower masses. The average of both curves is shown in figure 6.8 (upper right panel). From this comparison it seems that the mass shift scenario can be excluded. Comparing the mass shift scenario with the average experimental data in the invariant mass region from 600 MeV to 750 MeV yields to a $\chi^2/\mathrm{DoF} = 37.79/12$ with a χ^2 - probability of two per mill, while the comparison to the scenario with collisional broadening yields to a $\chi^2/\mathrm{DoF} = 19.55/12$ with a χ^2 - probability of 8%.
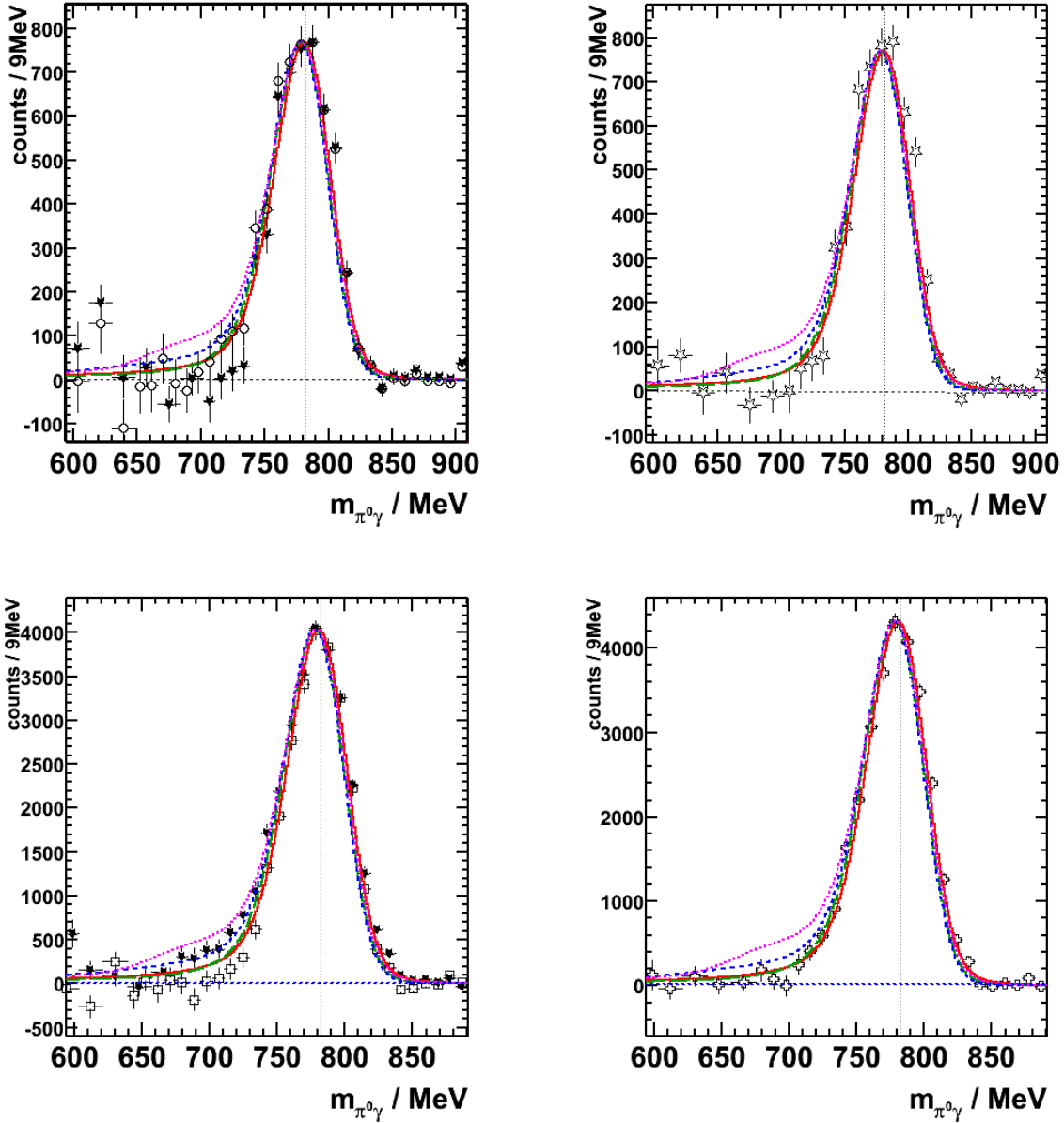
Figure 6.8: The niobium data is compared to the theoretical predictions: vacuum (solid red line), collisional broadening (dashed green line), collisional broadening plus mass shift (dashed blue line) and mass shift only (dotted magenta line). ***Exclusive analysis:*** *Upper left:* The open circles correpond to the data where the subtracted background was determined by a fit. For the black stars the subtracted background was determined directly from the data. *Upper right:* Avergage invariant mass spectrum of the two data analyses. ***Semi-exclusive analysis:*** *Lower left:* The open rectangles correpond to the data where the subtracted background was determined by a fit. For the black stars the subtracted background was determined directly from the data. *Upper right:* Avergage invariant mass spectrum of the two data analyses.

125

Also the two niobium data sets from the semi-exclusive analysis are compared to the theoretical calculations as illustrated in figure 6.8 (lower left panel). Whereas the stars (background determined from the data) seems to favour the scenario collisional broadening plus mass shift, the open rectangles (background determined from a fit) are below all the scenarios. The average of both signals seems to be in a good agreement with the GiBUU calculations as it is shown in figure 6.8 (lower right panel).

A comparison of the average experimental data to the mass shift scenario without collisional broadening in the mass range 600 MeV to 750 MeV yields to a $\chi^2/\mathrm{DoF} = 56.07/12$ with a χ^2 - probability of less then one per mill, while the comparison to the scenario with collisional broadening yields $\chi^2/\mathrm{DoF} = 8.16/12$ with a χ^2 - probability of 77%.

6.4. Momentum Distribution

For this analysis the ω yield is determined in different 50 MeV wide momentum bins. To have sufficient statistics over the full momentum range, the analysis is performed semi-exclusively. The ω signal is fitted with the Novosibirsk function to determine the ω yield. After the counts are corrected for the detector acceptance they are compared to recent GiBUU transport calculations, shown in figure 6.9. Looking at the theoretical predictions, they agree quite well with each other at higher momenta. Changes due to in-medium effects are expected at low momenta, where the chance for an ω meson is higher to decay in the medium. Therefore the data is normalized to the theoretical predictions at $p_{\pi^0\gamma} = 750$ MeV.

Both data sets do agree with the theoretical predictions within the errors at high momenta. At low momenta the theoretical predictions seem to overestimate the experimental data.

Nevertheless, this plot suggests that the scenarios with a mass shift can be excluded from the experimental data. The differences between the scenarios assuming no medium modifications and collisional broadening are more pronounced compared to the predictions for the lineshape analysis, but even with the high statistics of this experiment it is not possible to distinguish between these two scenarios.
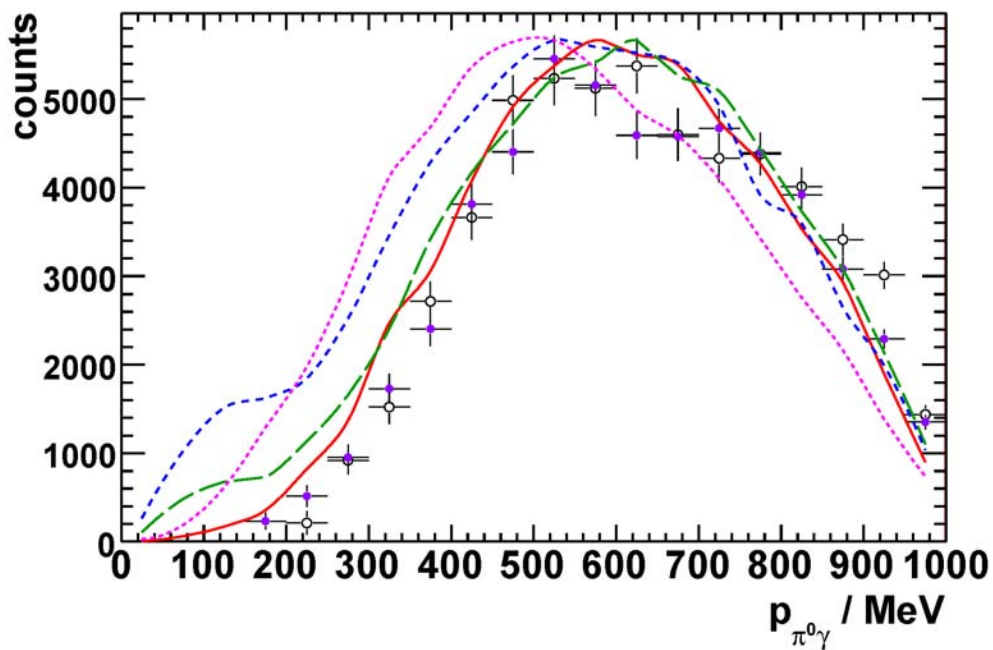
Figure 6.9: *Semi-exclusive analysis:* Momentum distribution for the two targets carbon (purple points) and niobium (open black circles), compared to the theoretical predictions: no modification (solid red line), collisional broadening (dashed green line), collisional broadening plus mass shift (dashed blue line) and mass shift only (dotted magenta line).

Chapter 7.

Conclusion and Outlook

The experiments of this thesis were planned as second generation experiments with the goal to collect data with increased statistics close to the ω photoproduction threshold $E_{\gamma,thresh} = 1108$ MeV, motivated by BUU transport code calculations. The question should be answered whether information on in-medium modifications can be extracted from the ω meson lineshape or not. Therefore the decay channel $\omega \to \pi^0\gamma$ was investigated in this thesis. The main advantage of this hadronic decay channel is the suppression of the ρ contribution to the signal by two orders of magnitude.

To extract the ω lineshape, two different types of analysis were performed. In the one analysis the background is determined by a fit. The ratio of the signal to the fit shows the quality of the fit, with an average deviation in the mass range 400 to 700 MeV in the order of 1%. In the other analysis type the background is determined from the data, using the carbon data ratio of the $\pi^0\gamma$ spectrum to the background spectrum from four photons to correct the niobium background contribution. Since the lineshape of the ω signal is very sensitive to the background determination, the results of both methods can be compared and taken as a crosscheck of the lineshape extraction.

A comparison of the invariant mass distributions for the three different target materials (liquid hydrogen, carbon, niobium) showed good agreement for C and Nb and a slight broadening compared to the ω signal from the hydrogen target after correcting for the 5 cm target length. In the semi-exclusive analysis where the statistics is much higher, the same effect can be seen: the $\pi^0\gamma$ invariant mass distributions from the carbon and niobium target are in good agreement, but slightly broader compared to the ω signal from the hydrogen target corresponding to a thickness of 1 mm.

In addition the lineshape of the niobium signal is compared to GiBUU calculations. Here the probabiltity that the experimental data in the exclusive analysis is decribed by the mass shift without collisional broadening scenario is two per mill and therefore can be excluded. The probability for the collisional broadening scenario to describe the data is roughly 8%. The corresponding χ^2-Test for the semi-exclusive analysis give probabilities of less than one per mill and 77%, respectively.

The theoretical predictions for the momentum distribution of the ω mesons show a more pronounced difference between the four scenarios. Using here the high statistics in the semi-exclusive analysis, the experimental data reproduces the GiBUU calculations at the high momenta, while they are overestimated at low momenta.
From this comparison the two scenarios assuming collisional broadening plus mass shift and mass shift only can be excluded, which confirms the result obtained from the lineshape analysis.

Concerning the lineshape analysis, further studies are planned in the near future to extract the ω lineshape for a more restricted incident photon energy range from 900 to 1100 MeV. In addition, a cut on the ω momentum $p_\omega < 300$ MeV can be applied to increase the amount of in-medium decays.
The most promising method, however, to extract information on in-medium modifications is still the excitation function of the ω meson, where the ongoing analysis will soon give new results.

Appendix A.

Lineshape Analysis Fits
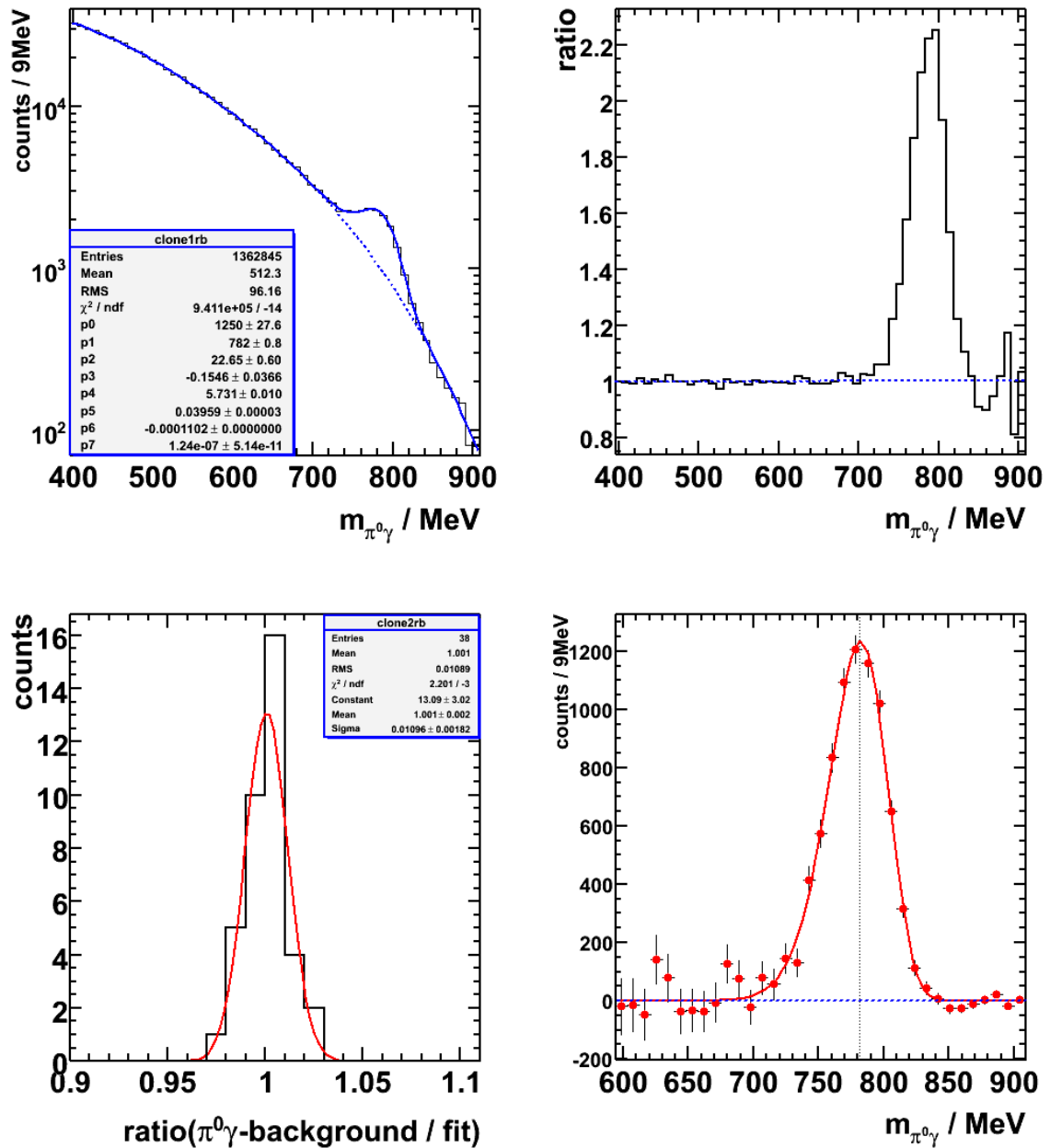
Figure A.1: ***Exclusive analysis for the carbon target, background determined by the fit method.*** *Upper left:* $\pi^0\gamma$ invariant mass spectrum. *Upper right:* Ratio of the $\pi^0\gamma$ spectrum to the background fit. *Lower left:* Average deviation from 1 in the mass range 350 to 700 MeV is 1%. *Lower right:* $\pi^0\gamma$ invariant mass spectrum after background subtraction.
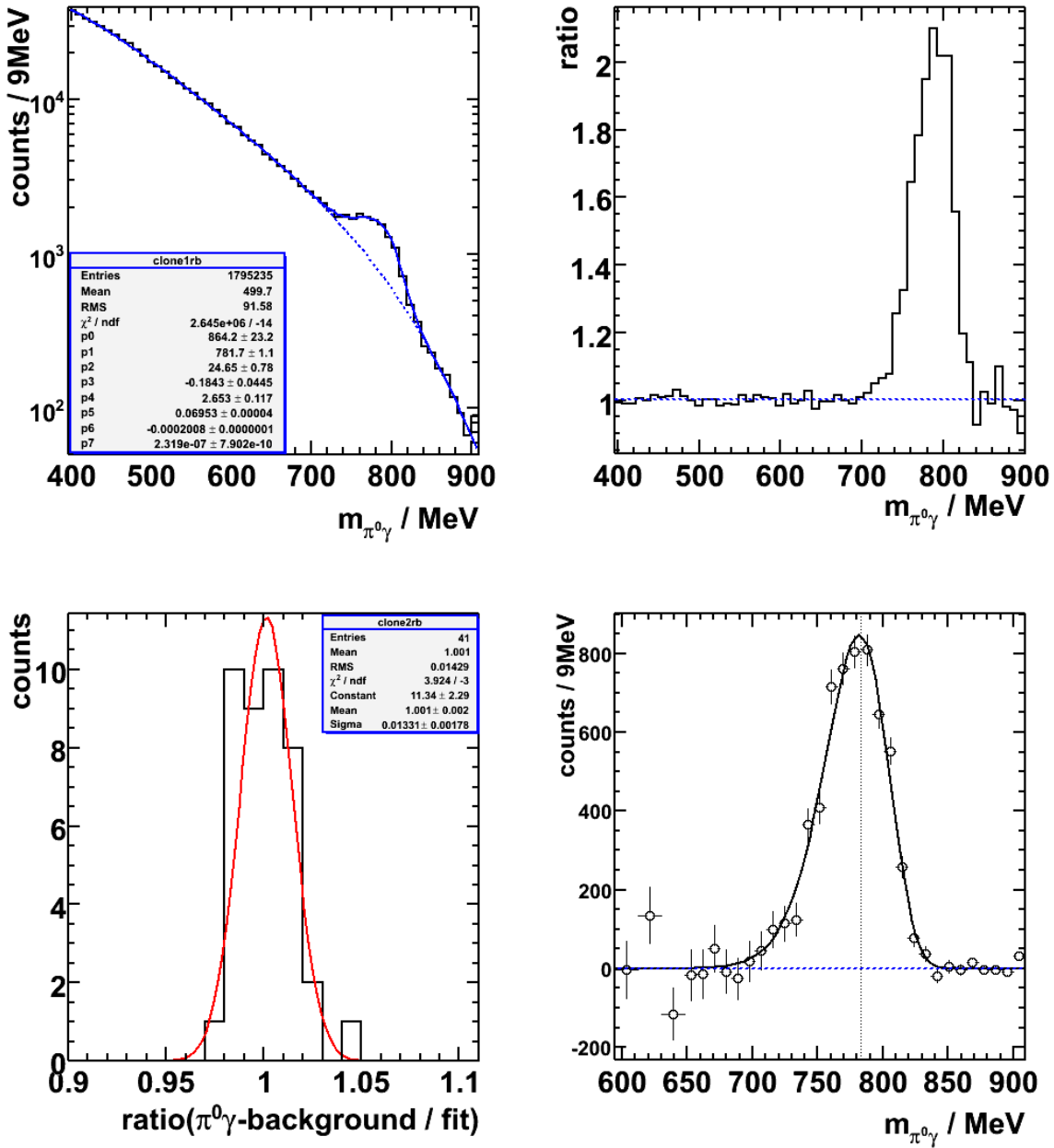
Figure A.2: *Exclusive analysis for the niobium target, background determined by the fit method.* *Upper left:* $\pi^0\gamma$ invariant mass spectrum. *Upper right:* Ratio of the $\pi^0\gamma$ spectrum to the background fit. *Lower left:* Average deviation from 1 in the mass range 350 to 700 MeV is 1.3%. *Lower right:* $\pi^0\gamma$ invariant mass spectrum after background subtraction.
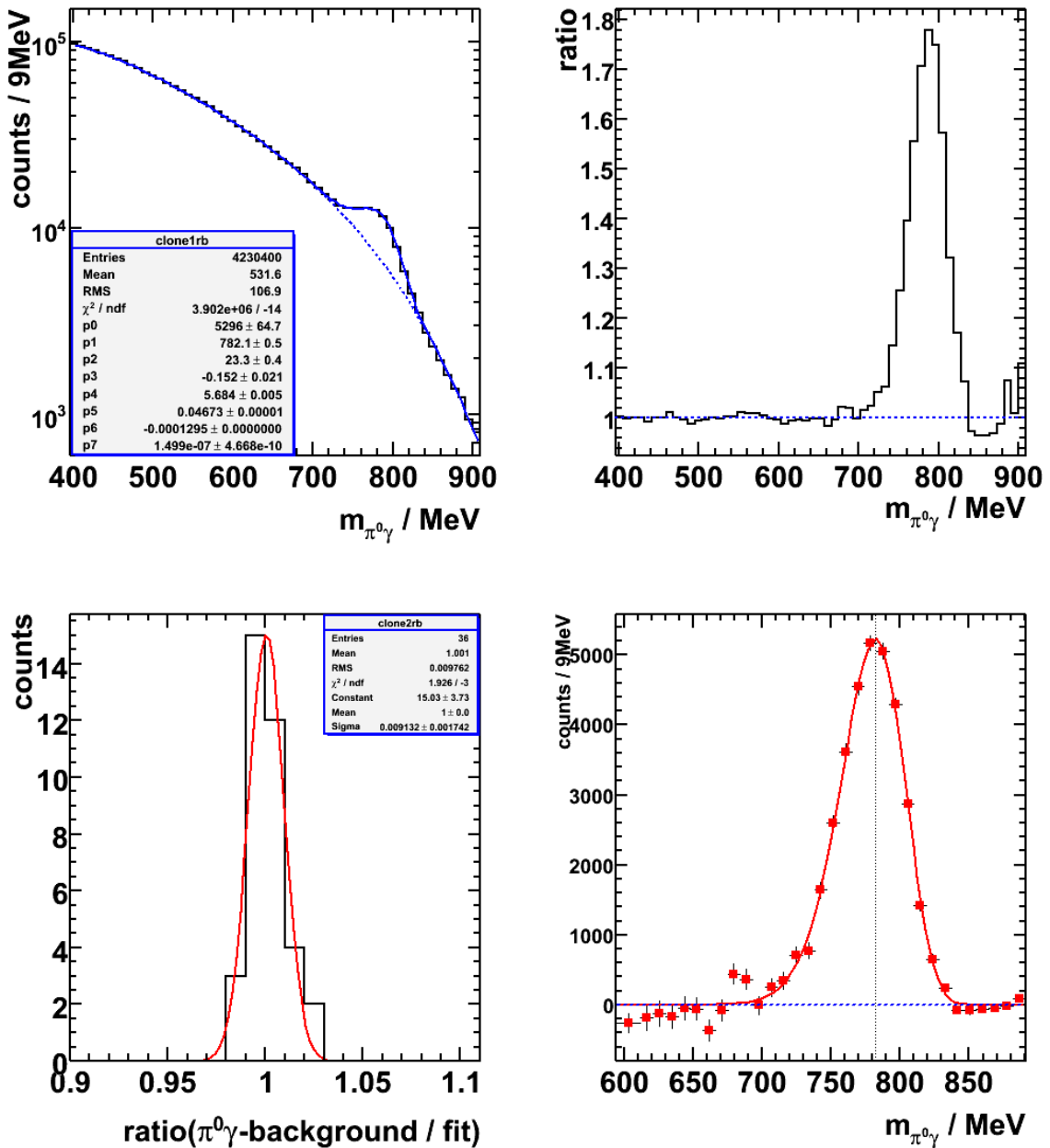
Figure A.3: *Semi-exclusive analysis for the carbon target, background determined by the fit method. Upper left:* $\pi^0\gamma$ invariant mass spectrum. *Upper right:* Ratio of the $\pi^0\gamma$ spectrum to the background fit. *Lower left:* Average deviation from 1 in the mass range 350 to 700 MeV is less than 1%. *Lower right:* $\pi^0\gamma$ invariant mass spectrum after background subtraction.
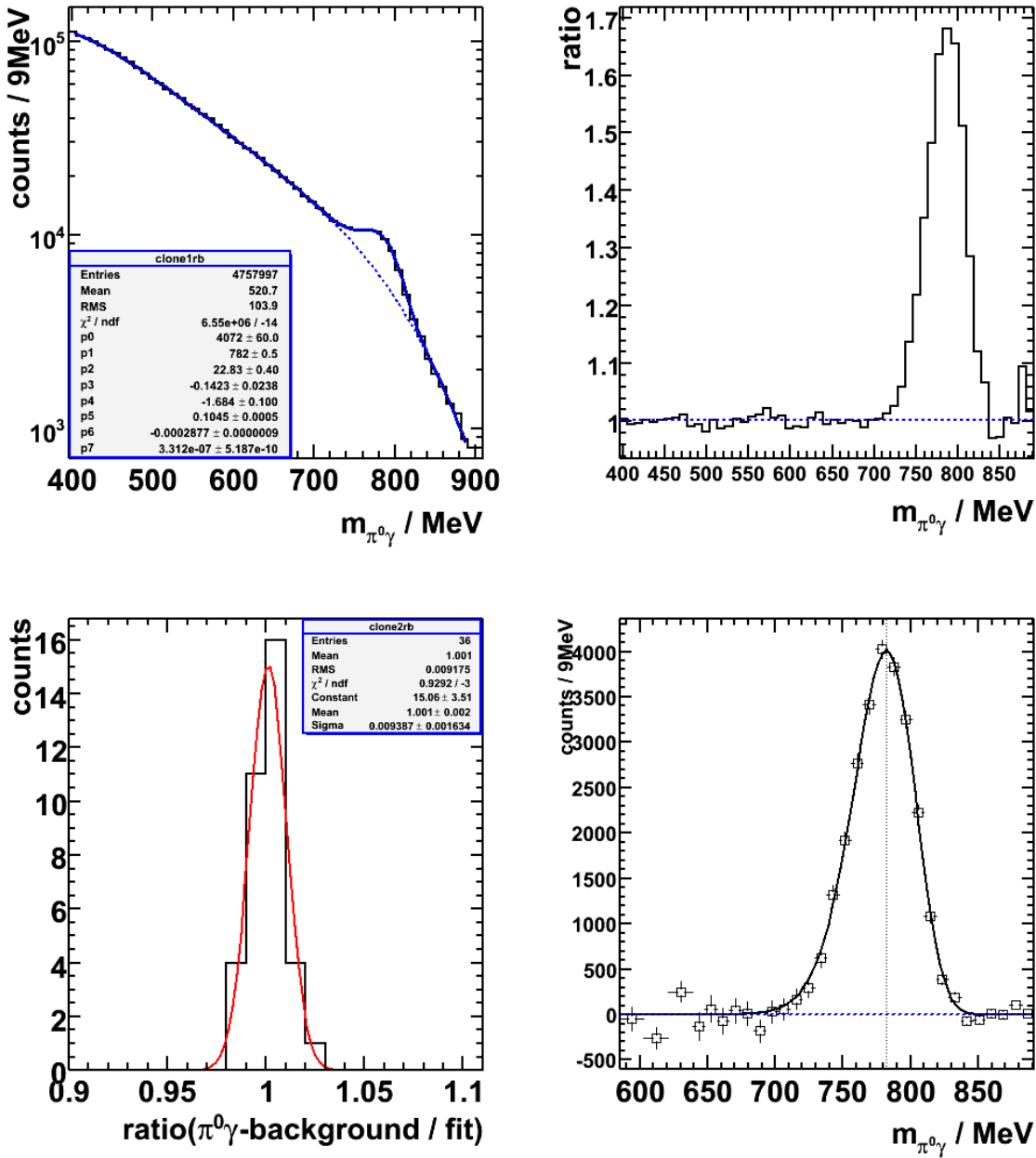
Figure A.4: *Semi-exclusive analysis for the niobium target, background determined by the fit method.* *Upper left:* $\pi^0\gamma$ invariant mass spectrum. *Upper right:* Ratio of the $\pi^0\gamma$ spectrum to the background fit. *Lower left:* Average deviation from 1 in the mass range 350 to 700 MeV is less than 1%. *Lower right:* $\pi^0\gamma$ invariant mass spectrum after background subtraction.
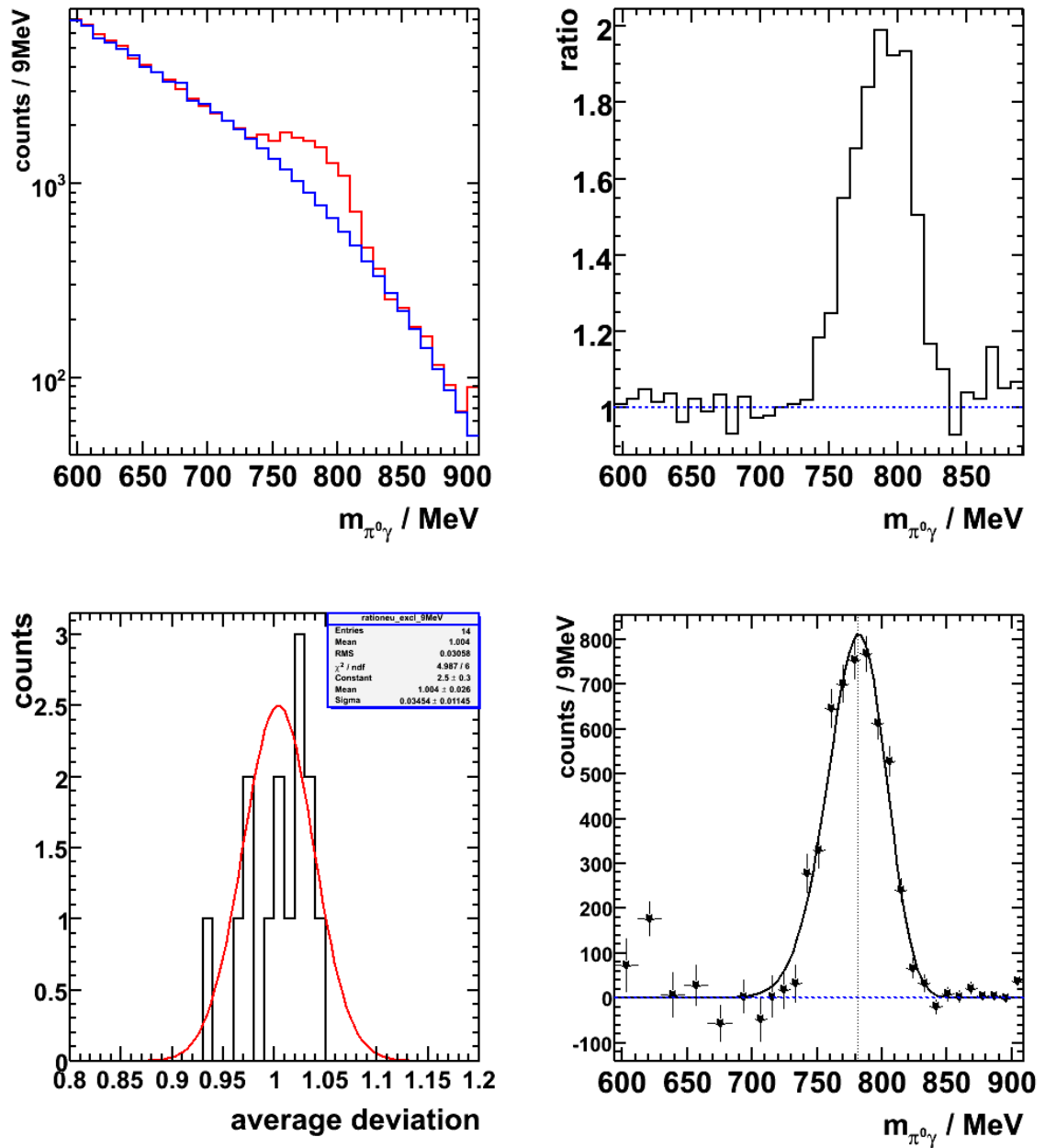
Figure A.5: *Exclusive analysis for the niobium target, background determined from the data.* *Upper left:* $\pi^0\gamma$ invariant mass spectrum. *Upper right:* Ratio of the $\pi^0\gamma$ spectrum to the background determined from the data. *Lower left:* Average deviation from 1 in the mass range 600 to 700 MeV is 3.5%. *Lower right:* $\pi^0\gamma$ invariant mass spectrum after background subtraction.
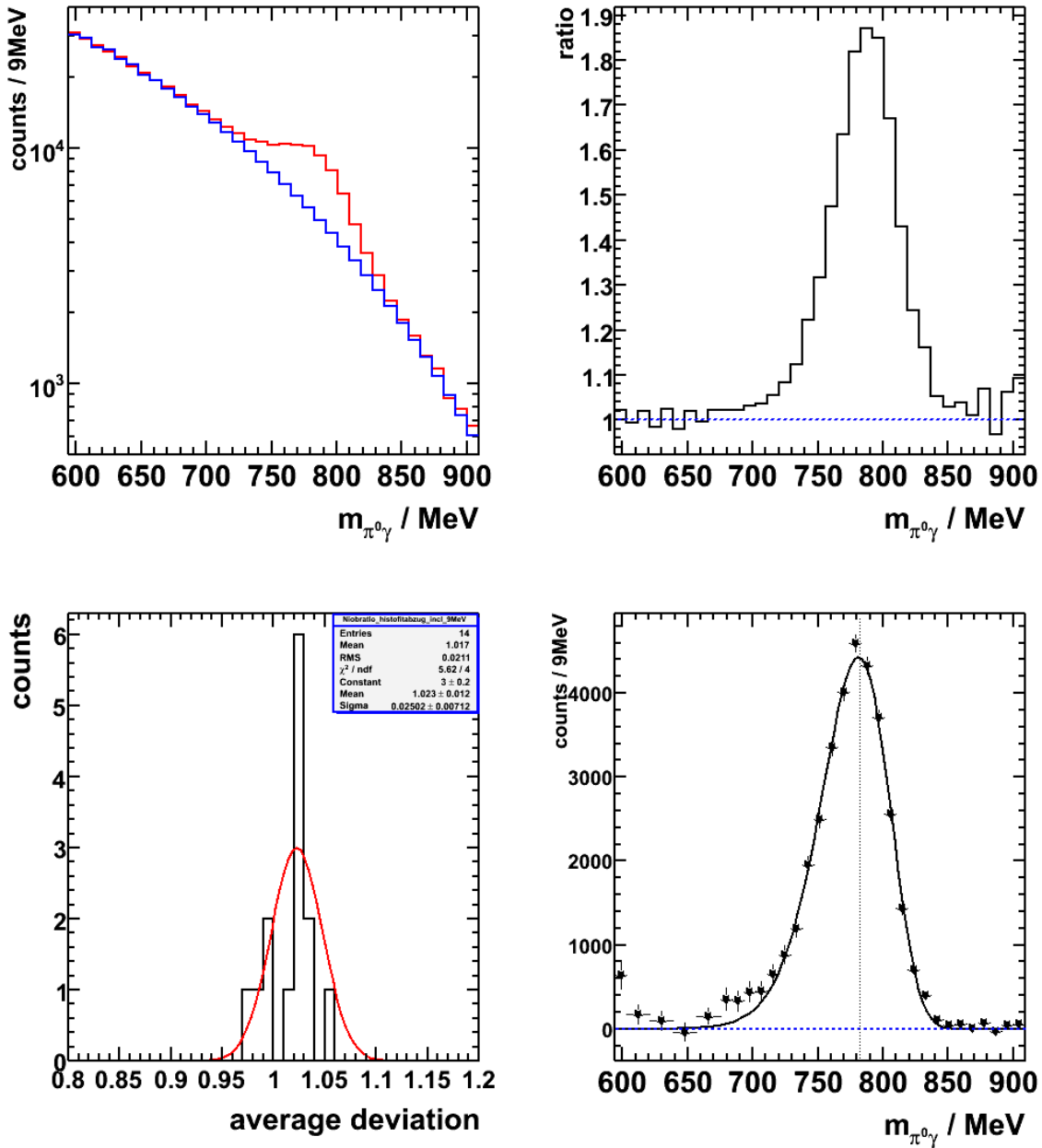
Figure A.6: *Semi-exclusive analysis for the niobium target, background determined from the data.* *Upper left:* $\pi^0\gamma$ invariant mass spectrum. *Upper right:* Ratio of the $\pi^0\gamma$ spectrum to the background determined from the data. *Lower left:* Average deviation from 1 in the mass range 600 to 700 MeV is 2.5%. *Lower right:* $\pi^0\gamma$ invariant mass spectrum after background subtraction.
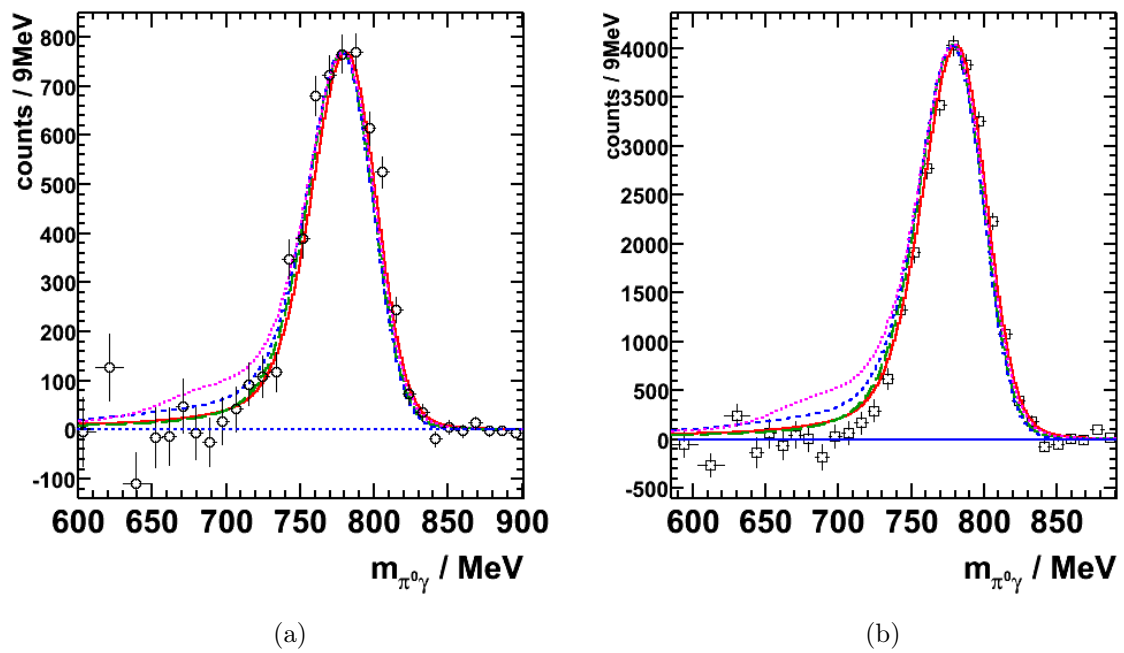
Figure A.7: $\pi^0\gamma$ invariant mass spectrum in comparison to the theoretical calculations. **(a)** Exclusive analysis, background determined by a fit. **(b)** Semi-exclusive analysis, background determined by a fit.

Appendix B.

Momentum Analysis Fits
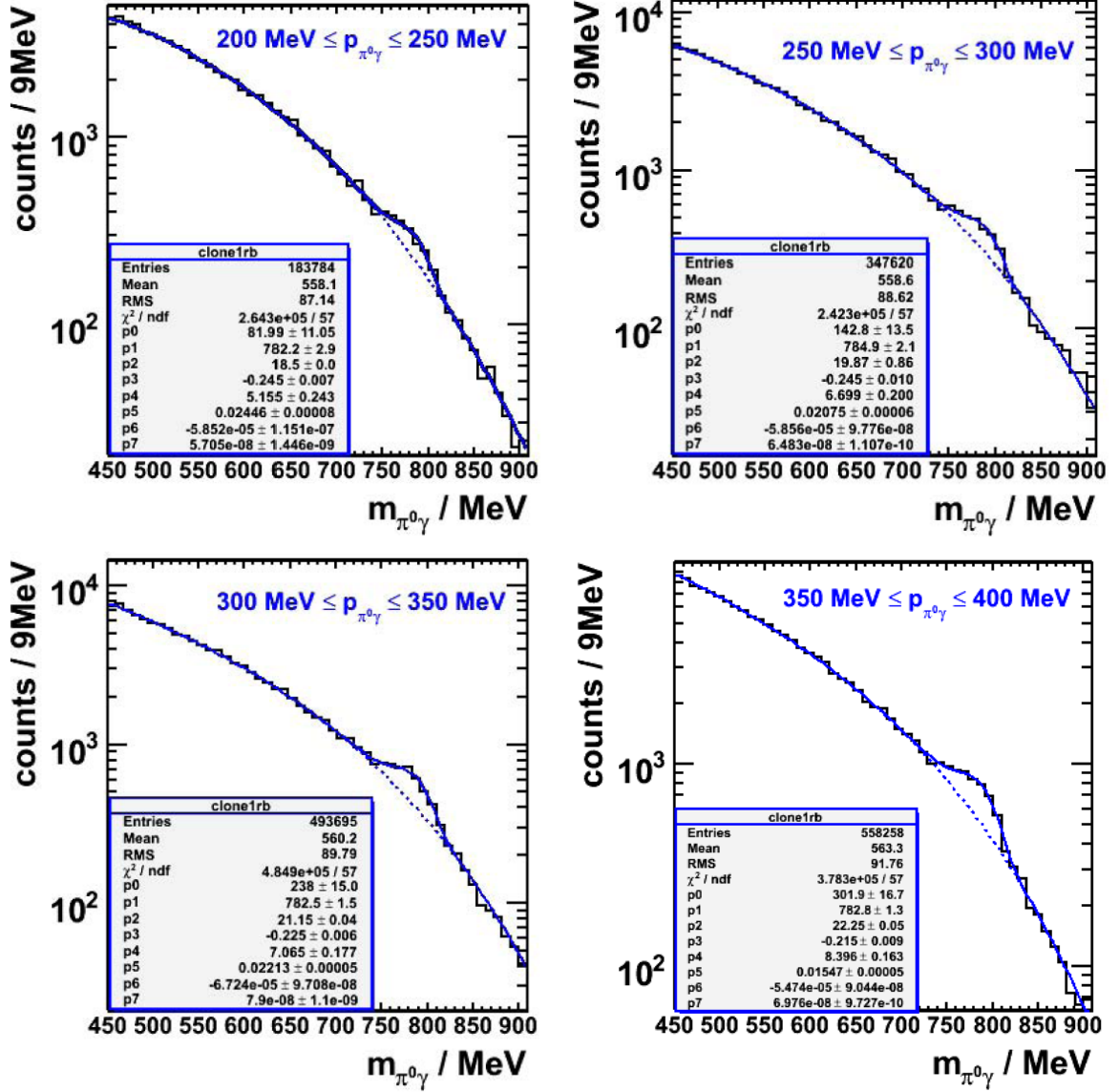
Figure B.1: *Semi-exclusive analysis for the carbon target.* $\pi^0\gamma$ invariant mass spectrum with the fit to the signal in blue and to the background in dashed blue.
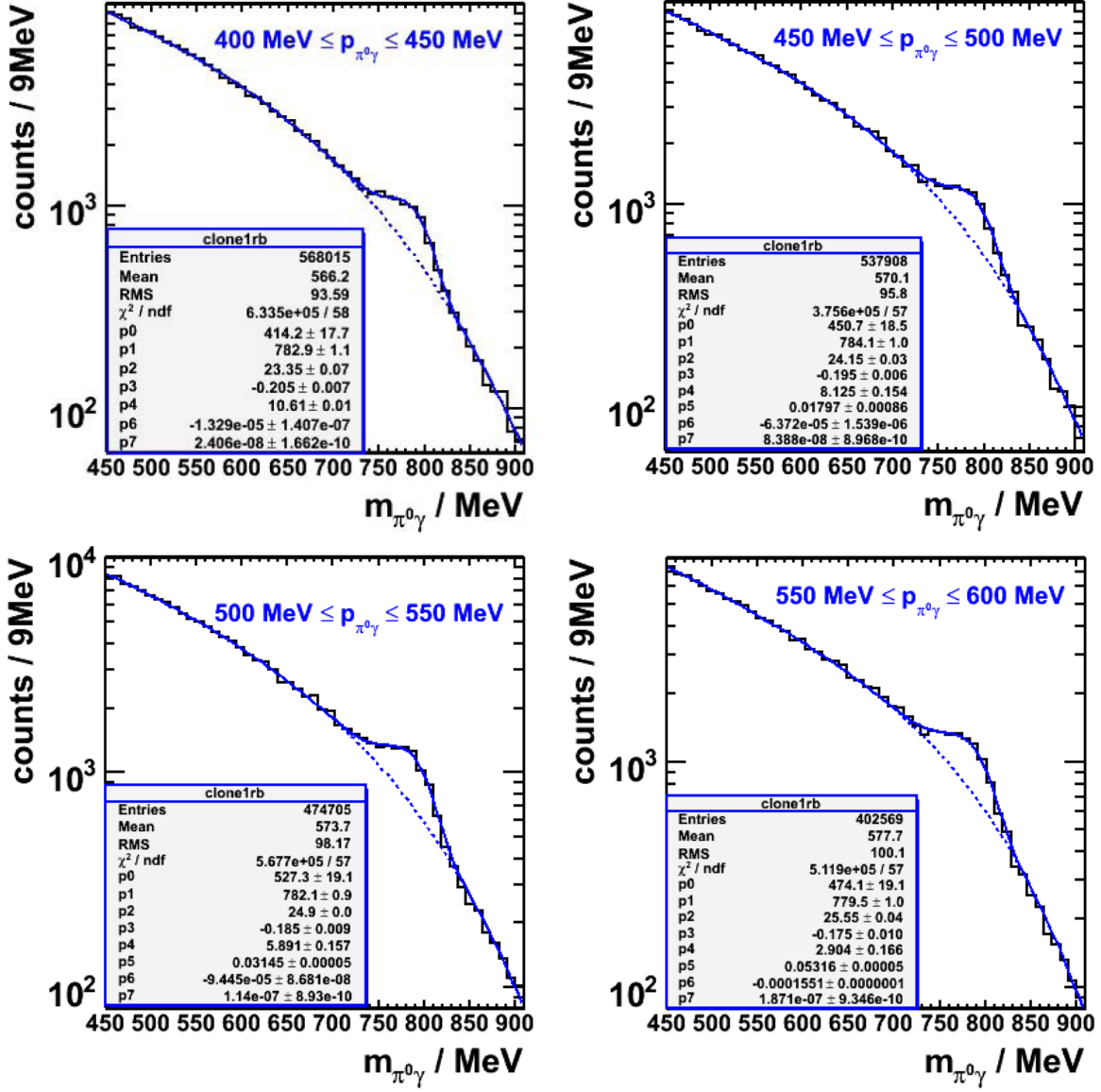
Figure B.2: *Semi-exclusive analysis for the carbon target.* $\pi^0\gamma$ invariant mass spectrum with the fit to the signal in blue and to the background in dashed blue.
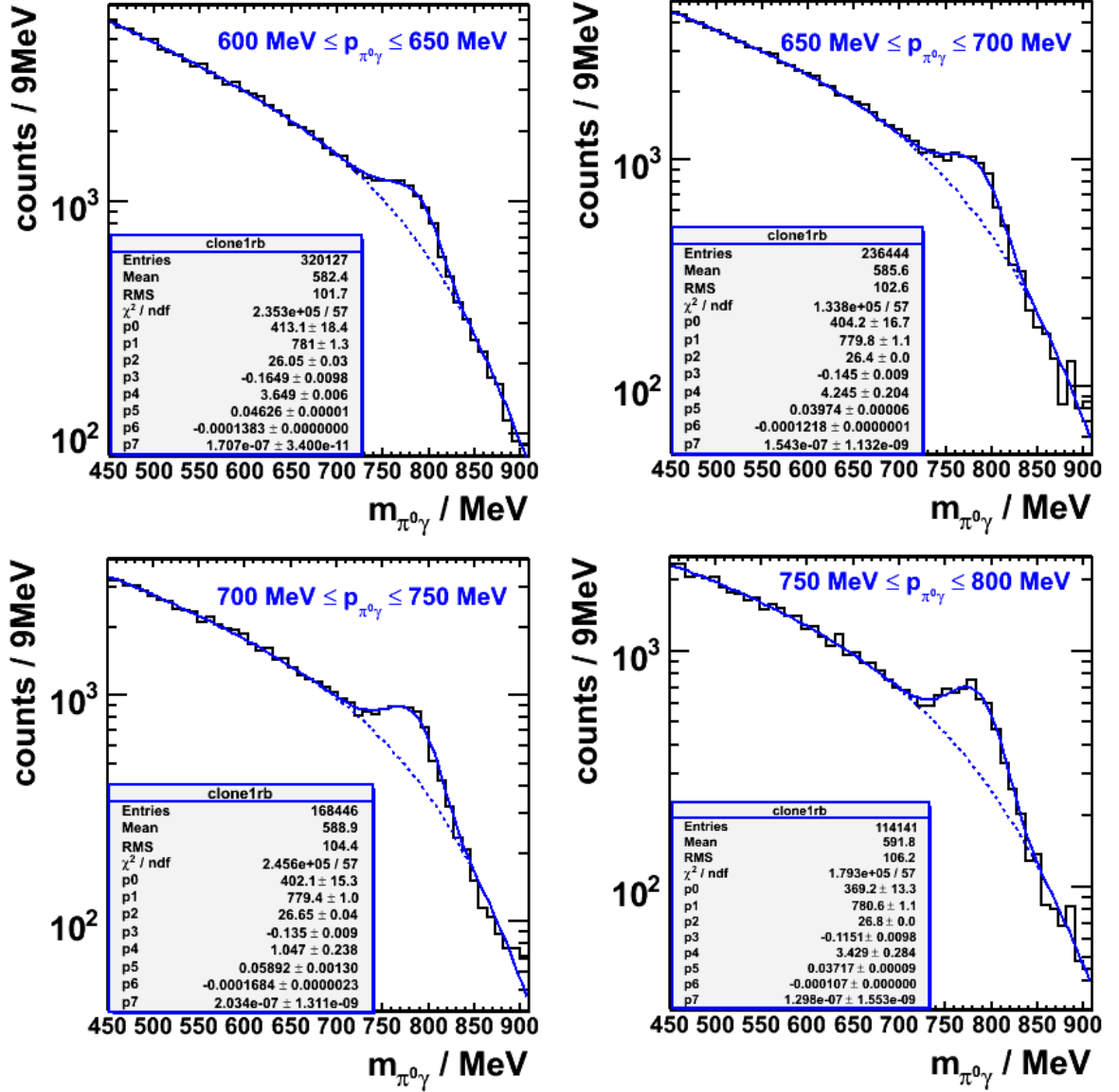
Figure B.3: *Semi-exclusive analysis for the carbon target.* $\pi^0\gamma$ invariant mass spectrum with the fit to the signal in blue and to the background in dashed blue.
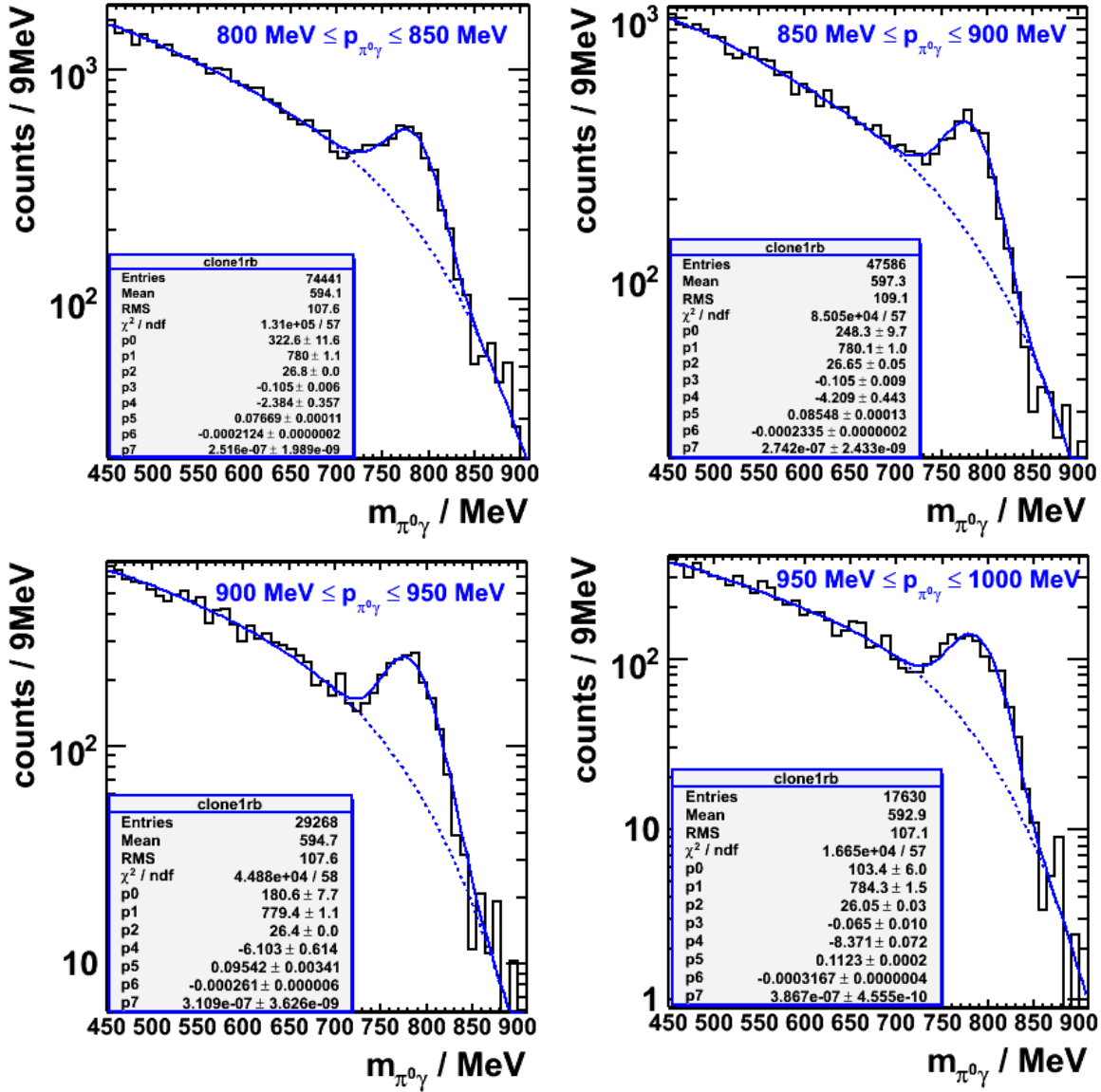
Figure B.4: *Semi-exclusive analysis for the carbon target.* $\pi^0\gamma$ invariant mass spectrum with the fit to the signal in blue and to the background in dashed blue.
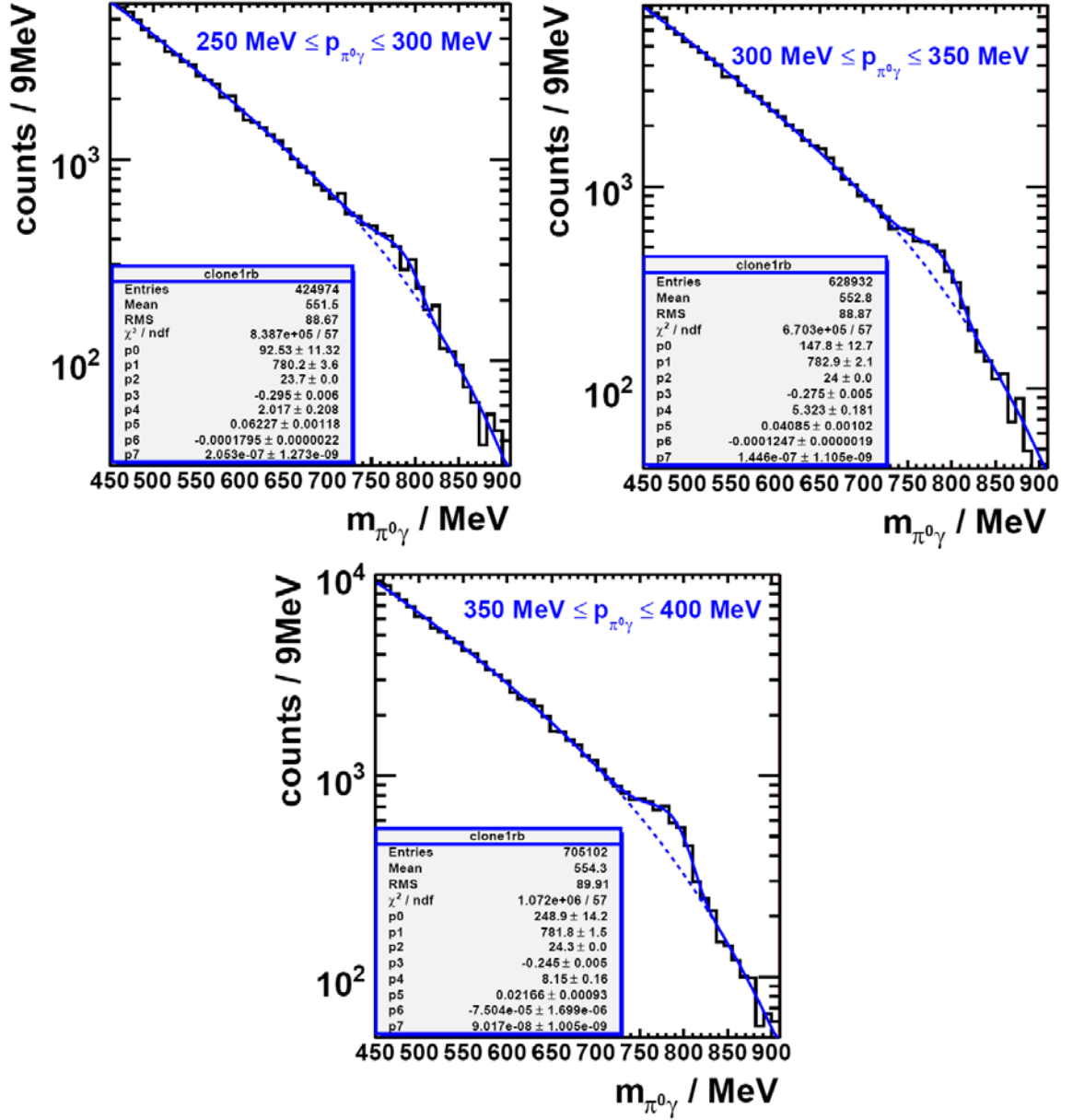
Figure B.5: *Semi-exclusive analysis for the niobium target.* $\pi^0\gamma$ invariant mass spectrum with the fit to the signal in blue and to the background in dashed blue.
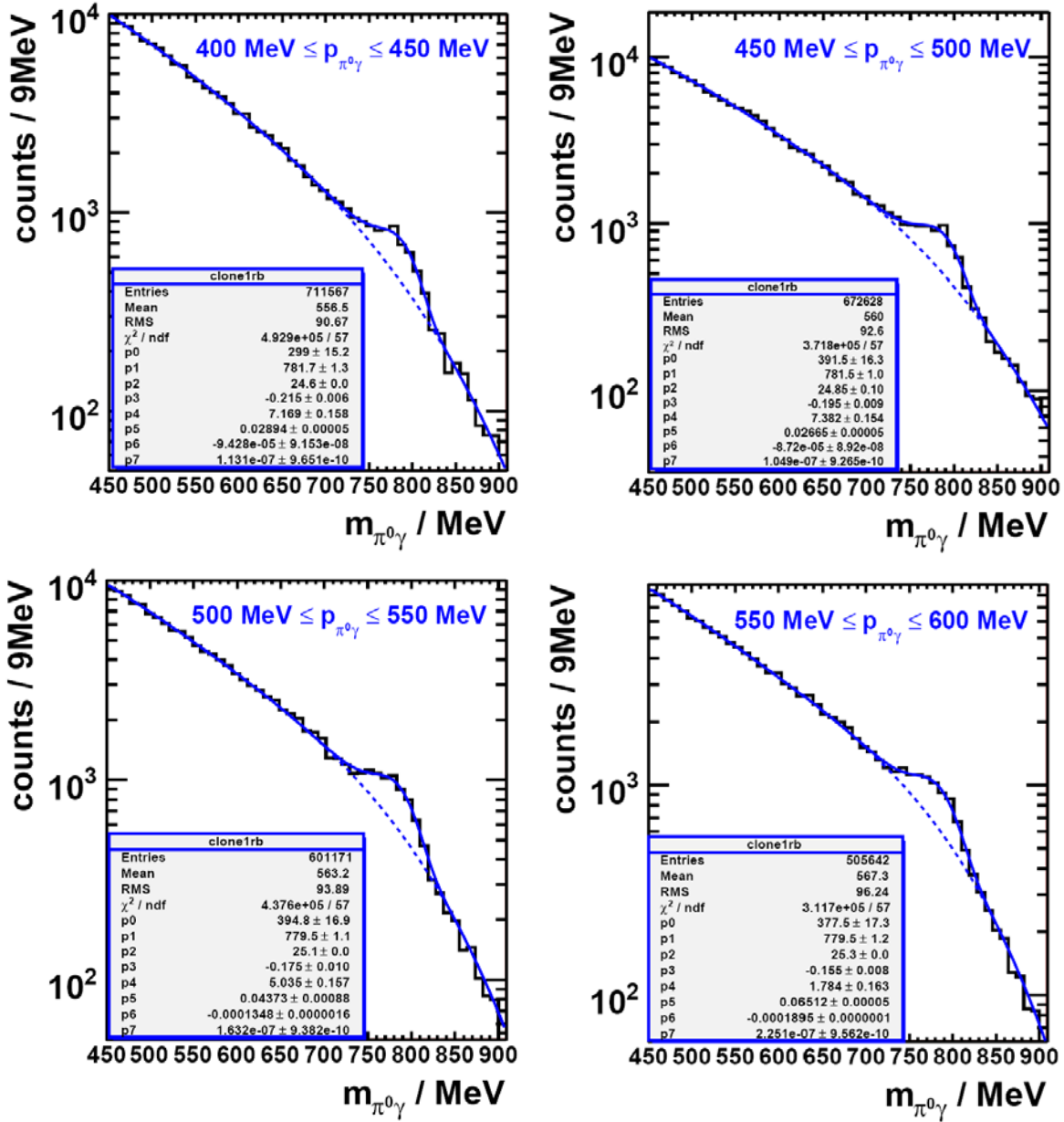
Figure B.6: *Semi-exclusive analysis for the niobium target.* $\pi^0\gamma$ invariant mass spectrum with the fit to the signal in blue and to the background in dashed blue.
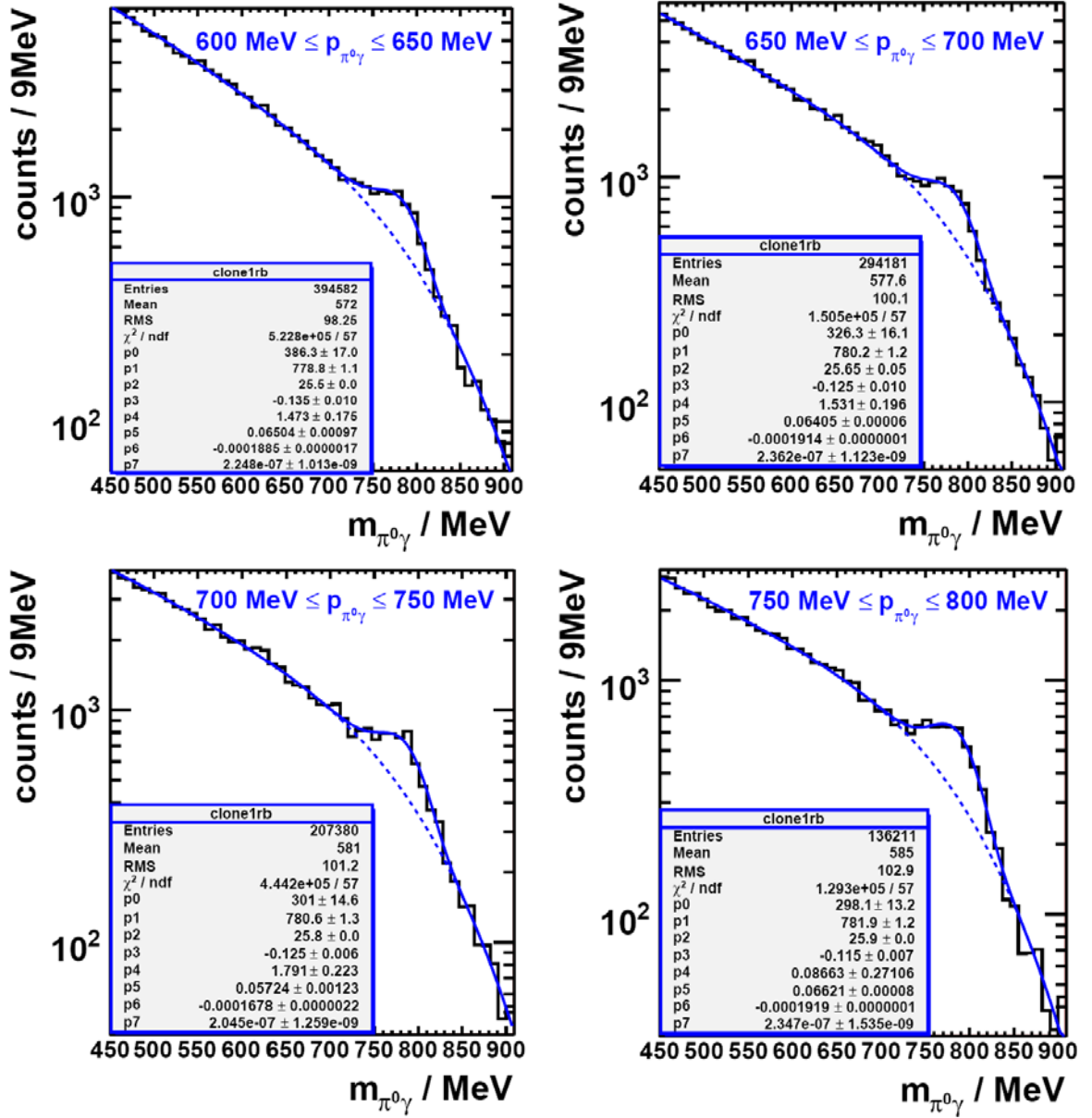
Figure B.7: *Semi-exclusive analysis for the niobium target.* $\pi^0\gamma$ invariant mass spectrum with the fit to the signal in blue and to the background in dashed blue.
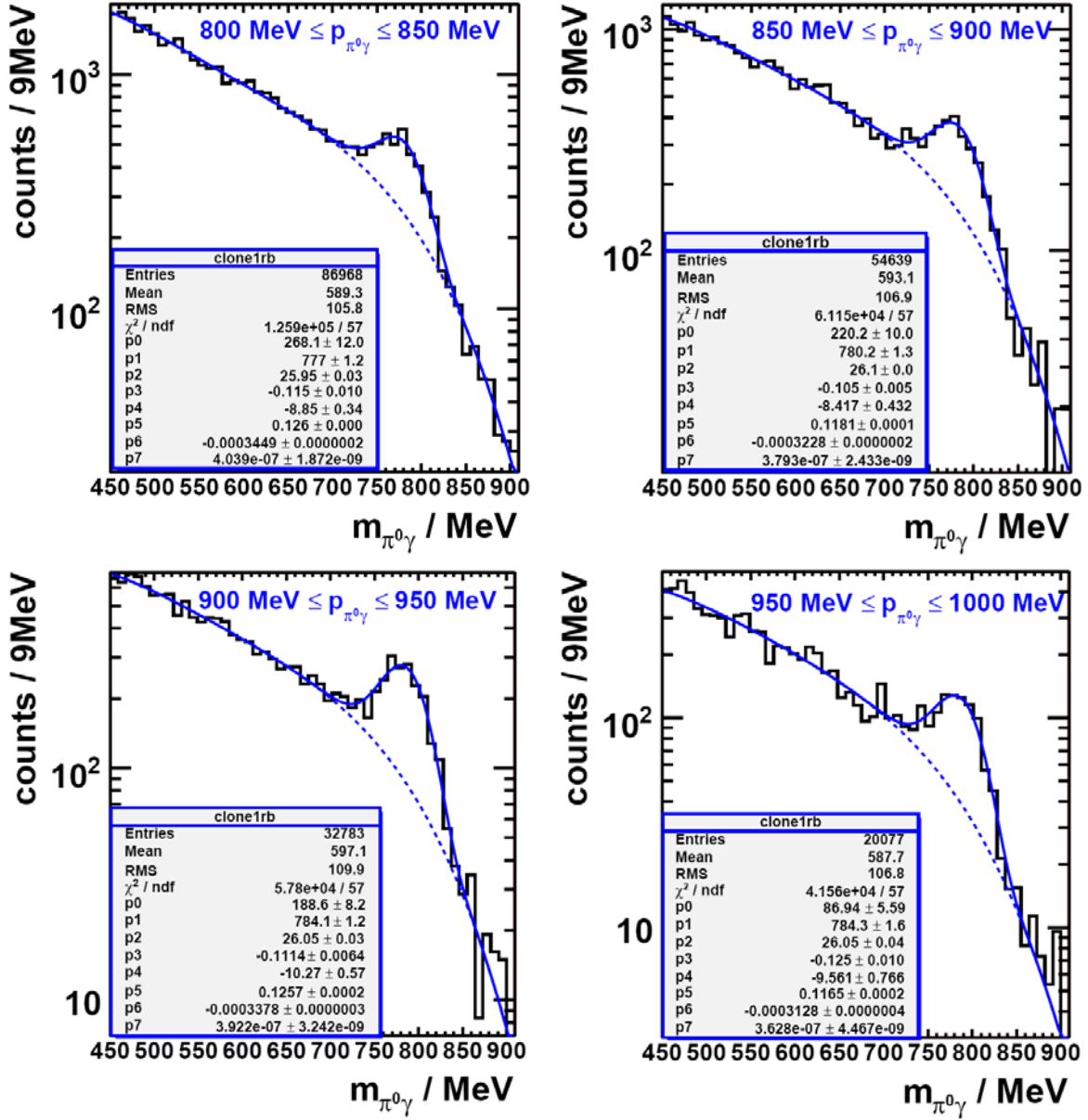
Figure B.8: *Semi-exclusive analysis for the niobium target.* $\pi^0\gamma$ invariant mass spectrum with the fit to the signal in blue and to the background in dashed blue.

List of Figures

154

List of Tables

Appendix C.

Bibliography

[Abe95]   Abe, F. et al. Observation of Top Quark Production in $\bar{p}p$ Collisions with the Collider Detector at Fermilab. *Phys. Rev. Lett.*, 74(14):2626–2631, Apr 1995.

[Ada08]   Adamová, D. et al. Modification of the ρ meson detected by low-mass electron-positron pairs in central Pb-Au collisions at 158A GeV/c. *Phys. Lett. B*, 666:425–429, 2008. arXiv:nucl-ex/0611022v3.

[Ago03]   Agostinelli, S. et al. G4–a simulation toolkit. *Nuclear Instruments and Methods in Physics Research Section A: Accelerators, Spectrometers, Detectors and Associated Equipment*, 506(3):250 – 303, 2003.

[Arn06]   Arnaldi, R. et al. First Measurement of the ρ Spectral Function in High-Energy Nuclear Collisions. *Phys. Rev. Lett.*, 96, 2006. arXiv:nucl-ex/0605007v1.

[Bar64]   Barnes, V. E. et al. Observation of a Hyperon with Strangeness Minus Three. *Phys. Rev. Lett.*, 12(8):204–206, Feb 1964.

[Ber88]   Bernard, V. and Meissner, U. G. Properties of vector and axial-vector mesons from a generalized Nambu-Jona-Lasinio model. *Nuclear Physics A*, 489:647–670, 1988.

[Bro91]   Brown, G. E. and Rho, Mannque . Scaling effective Lagrangians in a dense medium. *Phys. Rev. Lett.*, 66(21):2720–2723, May 1991.

[Col05]   PANDA Collaboration. Technical progress report, 2005. http://www-panda.gsi.de.

[Col09a] B1 Collaboration. http://www.kph.uni-mainz.de/b1/, 2009.

[Col09b] PANDA Collaboration. Physics Performance Report for PANDA: Strong Interaction Studies with Antiprotons, 2009. arXiv:0903.3905v1 [hep-ex].

[Dow06]   Downie, E. J. Radiative π^0 photoproduction in the region of the $\Delta(1232)$ resonance. PhD thesis, University of Glasgow, Mainz, Germany, 2006.

[Dre00]   Drexler, P. Aufbau eines Zeitzweiges für die neue TAPS-Elektronik. Diploma thesis, Justus-Liebig-University, Gießen, Germany, 2000.

[Dre02]   Drexler, P. et al. The New Read-Out Electronics for the BaF_2-Calorimeter TAPS. *IEEE Transactions on Nuclear Science*, 2002.

[Dre04]   Drexler, P. Entwicklung und Aufbau der neuen TAPS-Elektronik. PhD thesis, Justus-Liebig-University, Gießen, Germany, 2004.

[Fri10]   Friedrich, S. private communication, 2010.

[Gab94]   Gabler, A. R. Response of TAPS to monochromatic photonswith energies between 45 and 790 MeV. *Nucl. Instr. and Methods* , 346:168–176, 1994.

[Gal08]   Gallmeister, K. et al. Hadrons in Nuclei from High (200 GeV) to Low (1 GeV) energies. *Phys. Lett. B*, 666:425–429, 2008. arXiv:nucl-th/07122200v1.

[Geß08]   T. Geßler. Particle identification of reaction products from photonuclear reactions using the taps detector system. Bachelor thesis, Justus-Liebig-University, Gießen, Germany, 2008.

[Hat92]   Hatsuda, T. and Lee, S. H. QCD sum rules for vector mesons in the nuclear medium. *Phys. Rev. C*, 46(1):R34–R38, Jul 1992.

[Hei10]   Heine, R. et al. Recent Status of the MAMI-C Accelerator and First Experiences with the Energy Upgrade towards 1.6 GeV. *Proc. of the iPAC 2010, Kyoto, Japan*, 2010.

[Jan99]   Janssen, S. et al. The new charged-particle veto detector for the photon spectrometer taps. *Nuclear Physics A*, 650(3):299 – 312, 1999.

[Kas07]   Kaskulov, M., Hernandez, E. and Oset, E. Inclusive ω photoproduction from nuclei and ω in the nuclear medium. *Eur. Phys. J. A*, 31:245–254, 2007. arXiv:nucl-th/0610067v1.

[Kli99]   Klingl, F. and Waas, T. and Weise, W. Nuclear bound states of ω mesons. *Nuclear Physics A*, 650(3):299 – 312, 1999. .

[Koc95]   Koch, V. Introduction to Chiral Symmetry, 1995. arXiv:nucl-th/9512029.

[Kot08]   Kotulla, M. et al. Modification of the ω-meson lifetime in nuclear matter. *Physical Review Letters*, 100(19):192302, 2008. arXiv:0802.0989v1 [nucl-ex].

[Lem09]   B. Lemmer. Measurement of the excitation function of ω-photoproduction on carbon and niobium. Diploma thesis, Justus-Liebig-University, Gießen, Germany, 2009.

[Lut02]   Lutz,M. F. M. and Wolf, Gy. and Friman, B. Scattering of vector mesons off nucleons. *Nuclear Physics A*, 706(3-4):431 – 496, 2002.

[Mar98]   Martin, A. Detection of charged pions and protons in the segmented electromagnetic calorimeter TAPS. *Nucl. Instr. and Methods* , 417:137–149, 1998.

[McG08]   McGeorge, J. C. et al. Upgrade of the Glasgow photon tagging spectrometer for Mainz MAMI–C. *The European Physical Journal A*, 37(1):129–137, 2008.

[Mes01]   Messchendorp, J. G. etal. Studying the ω mass in-medium in $\gamma + A \to \pi^0\gamma + X$ reactions. *The European Physics Journal A - Hadrons and Nuclei*, 11(1):95–103, 2001.

[Mue06a]   Muehlich, P. and Mosel, U. Attenuation of ϕ mesons in γA reactions. *Nucl. Phys. A*, 765:188–196, 2006. arXiv:nucl-th/0510078v1.

[Mue06b]   Muehlich, P. and Mosel, U. ω attenuation in nuclei. *Nucl. Phys. A*, 73:156–172, 2006. arXiv:nucl-th/0602054v1.

[Mue06c]   Muehlich, P. and Shklyar, V.and Leupold, S. and Mosel, U. and Post, M. The spectral function of the ω meson in nuclear matter from a coupled-channel resonance model. *Nuclear Physics A*, 780(3-4):187 – 205, 2006.

[Nan10a]   Nanova, M. et al. In-medium ω mass from the $\gamma + Nb \to \pi^0\gamma + X$ reaction. *Phys. Rev. C*, 82(3):035209, Sep 2010. arXiv:nucl-ex/1005.5694v2.

[Nan10b]   Nanova, M. et al. Photoproduction of ω mesons on nuclei near the production threshold. *European Physical Journal A*, 2010. to be published.

[Nar06]   Naruki, M. et al. Experimental Signature of Medium Modifications for ρ and ω Mesons in the 12 GeV p + A Reactions. *Phys. Rev. Lett.*, 96, 2006. arXiv:nucl-ex/0504016v4.

[Nas07]   Nasseripour, R. et al. Search for Medium Modifications of the ρ Meson. *Phys. Rev. Lett.*, 99, 2007. arXiv:nucl-ex/07072324v3.

[Nef95]   Nefkens, B.M.K. The crystal ball. *Crystal Ball Report 95-1*, 1995.

[Nov91]   Novotny, R. The BaF_2 Photon Spectrometer TAPS. *IEEE Transactions on Nuclear Science*, 38(2):379–385, 1991.

[PDG08]   Particle Data Group PDG. Particle physics booklet, 2008.

[Roe91]   Roebig-Landau, M. Eichung des TAPS-Detektorsystems mit Hoehenstrahlung. Diploma thesis, Justus-Liebig-University, Gießen, Germany, 1991.

[Trn05]   Trnka, D. et al. Observation of In-Medium Modifications of the ω Meson. *Phys. Rev. Lett.*, 94(19):192303, May 2005.

[Wei10]   Weil, J. private communication, 2010.

Danksagung

Mein Dank gilt zuerst Prof. Dr. Volker Metag dafür, dass ich an diesem spannenden Thema arbeiten durfte. Auch wenn, oder gerade weil es nicht immer einfach war, habe ich in den letzten Jahren viel gelernt.

Danken möchte ich auch meinem „Baby" TAPS in Mainz. Die meiste Zeit hat es problemlos funktioniert und nur ganz wenig Scherereien verursacht. In diesem Zusammenhang ebenfalls ein großes Dankeschön an die tollen Menschen der A2 Kollaboration, ohne die diese Arbeit nicht möglich gewesen wäre. Im speziellen an Erik, Evie und Olli, die wirklich zu jeder Tages - und Nachtzeit bei der Lösung von Problemen geholfen haben. Und das Wichtigste: die Zusammenarbeit hat wirklich Spass gemacht! Zudem ein besonderer Dank an den Basler TAPSianer Dominik für seine Hilfe.

Für die Unterstützung und den Spass möchte ich meinen (Ex-)Zimmerkollegen Henning und Boris danken. Zusammen haben wir doch alle schwierigen Situationen der letzten Jahre gemeistert, wenn auch manchmal mit einer großen Portion Galgenhumor. Aber wir waren erfolgreich!

Karoly, you are my hero! Without you, this work would not be finished now. Thanks so much!

Ein globales danke geht an alle Mitarbeiter und inzwischen Ehemalige der Arbeitsgruppe Metag für eine tolle Arbeitsatmosphäre. Da wären Anita, Henning, Jürgen, Mariana, Ralf, René, Stefan L., Uli, Volker, Werner, die Bonner TAPSianer Frida, Karoly und Stefan F. sowie die PANDA-Bärchen Daniel, Markus, Peter, Rainer, Till, Tobi und Valera. Es war immer schön bei einem Kaffee über die physikalischen und nichtphysikalischen Dinge des Lebens zu diskutieren.

Einen wesentlichen Beitrag zu dieser Arbeit haben auch die fleißigen Korrekturleser geleistet. Allen voran der mutige Erstleser Olli. Ich sage vielen Dank und kann nur hoffen, dass es nicht zu grausam war... Für das ausmerzen der übrigen Schreibfehler geht mein Dank an Daniel, Markus und Tobi.

Danke an Benjamin, Nico, Till, die mich während meiner gesamten Studienzeit begleitet und in den letzten Wochen ertragen haben, bzw. meine Abwesenheit an

jeglicher sozialer Aktivität. Und tatsächlich: „Alles wird gut!"

Andy gilt mein spezieller Dank für das gemeinsame Durchstehen meiner Dissertationszeit. Ich kann mir keinen besseren „Stuhl" vorstellen!
Das finale Dankeschön geht an meine Eltern, die mich während meiner gesamten Promotion und vor allem in den letzten Wochen unterstützt haben.

Erklärung

Hiermit versichere ich, dass ich diese Arbeit selbständig verfasst und keine weiteren Quellen und Hilfsmittel außer den genannten verwendet habe. Diese Arbeit wurde bisher keiner anderen Prüfungsbehörde vorgelegt und auch noch nicht veröffentlicht.

Michaela Thiel
Gießen, 10.November 2010